The Role of a Direct Knock-out Mechanism in the Inclusive (p, α) Reaction

Johannes Jacobus van Zyl

Thesis presented in partial fulfillment of the
requirements for the degree of Master of Science at
Stellenbosch University

Supervisor: Prof G.C. Hillhouse
Co-supervisors: Prof A.A. Cowley and Dr B.I.S. van der Ventel

March 2008

Declaration:

I, the undersigned, hereby declare that the work contained in this thesis is my own original work and that I have not previously in its entirety or in part submitted it at any university for a degree.

Signature: ……

Date: …….

ABSTRACT

The role of a direct knock-out mechanism in the inclusive (p, α) reaction

Experimental double differential cross sections and analyzing powers for the inclusive $^{93}Nb(\vec{p}, \alpha)$ and $^{93}Nb(\vec{p}, {}^{3}He)$ reactions have been measured at an incident energy of 160 MeV. The results of this experiment, for emission angles ranging from 15° to 60° as well as previously measured data for $^{93}Nb(\vec{p}, \alpha)$ at 100 MeV and $^{59}Co(\vec{p}, \alpha)$ at 100 and 160 MeV, have been compared with theoretical calculations based on a direct quasi-free α-cluster knockout mechanism.

A computer code has been employed which calculates triple differential cross section and analysing power values using the distorted wave impulse approximation (DWIA). Inclusive double differential cross sections and analysing powers were calculated by integrating over the solid angle of the unobserved proton.

It was found that the DWIA is limited in its ability to reproduce the experimental data. Some slight agreements have been observed in the region of large emission energies and small angles. This is consistent with the findings of previous studies based on a direct multi-step analysis which indicated that the first step knock-out reaction dominates in this region.

UITTREKSEL

Die rol van 'n direkte uitslaanmeganisme in die inklusiewe (p, α) reaksie

Die dubbelle differensiële kansvlakke en analiseervermoë vir die inklusiewe $^{93}Nb(\vec{p}, \alpha)$ en $^{93}Nb(\vec{p}, {}^{3}He)$ reaksies is ondersoek by 'n invalsenergie van 160 MeV. Die eksperimentele resultate vir verstrooiingshoeke van 15° tot 60° is, saam met bestaande data vir die $^{93}Nb(\vec{p}, \alpha)$ reaksie by 100 MeV en $^{59}Co(\vec{p}, \alpha)$ reaksie by 100 en 160 MeV, vergelyk met teoretiese berekeninge wat gegrond is op 'n direkte, kwasi-vrye α-deeltjie uitslaanmeganisme.

Berekeninge is gedoen met 'n rekenaar program wat trippel differensiële kansvlakke en analiseervermoë waardes genereer deur middel van die vervormde-golf-impuls-benadering (DWIA). Inklusiewe berekeninge is gedoen deur die trippel differensiële kansvlakke en analiseervermoë te integreer oor die ruimtehoek van die nie-waargenome proton.

Daar is gevind dat die DWIA redelik beperk is vir die beskrywing van die eksperimentele data. Geringe ooreenstemming is wel waargeneem in die gebied waar die verstrooiingshoek klein, en die energie van die waargenome deeltjies hoog is. Hierdie resultate is versoenbaar met vorige direkte multistap berekeninge wat ook aangetoon het dat die eerste stap uitslaanreaksie die grootste bydrae in hierdie gebied lewer.

ACKNOWLEDGMENTS

My sincere gratitude and appreciation to all my friends, colleagues and family who have contributed towards the successful completion of this thesis, especially

- my co-supervisor **Professor Anthony Cowley**, whom I consider to be both a personal friend and colleague, for all our meaningful discussions. Your insight and experience in the field of experimental nuclear physics has been of great benefit to me.

- my supervisor **Professor Greg Hillhouse**, I have learned a great deal from you not only in terms of this work, but also in my general understanding of physics and our role as teachers. I don't think I have thanked you enough.

- **Dr. Retief Neetling** for your expert advice and willingness to always help me with running codes, working on the VAX/VMS system, doing the experimental setups and nuclear physics questions in general.

- my friends and colleagues at the University of Stellenbosch and iThemba LABS. A special word of thanks to **Dr. Anton Stander**, **Dr. Jacques Bezuidenhout**, **Nortin Titus**, and **Dr. Brandon van der Ventel**.

- the **Physics Department** for this opportunity and for allowing me the time away from the office to work on this study.

- my **father**, for your advice on many of the grammar and editing style issues in this thesis. This one's for you!

- my dearest wife **Frieda**, for your encouragement, love and patient understanding during those days and nights that I could not give you my full attention.

"O Lord my God, when I in awesome wonder, consider all the worlds Thy Hands have made. I see the stars, I hear the rolling thunder, Thy power throughout the universe displayed. Then sings my soul, my Saviour God, to Thee! How great Thou art, how great Thou art!"

- Carl Gustaf Boberg (1859-1940)

TABLE OF CONTENTS

CHAPTER 1 INTRODUCTION

A brief overview of the nuclear reaction mechanisms describing the interaction of medium energy protons with target nuclei is presented in this chapter. Section 1.1 gives a summary of the broad distinctions made between different reaction mechanisms. The second section is concerned with the study of the (p, α) reaction and its importance for our understanding of nuclear reactions. In the last section of this chapter, section 1.3, the aims and scope of this thesis are highlighted.

1.1 Background to nuclear reactions

When the energy of a projectile incident on a target nucleus is high enough to overcome the Coulomb potential, it will experience the strong nuclear force caused by the nucleons inside the nucleus. This interaction is successfully described by the optical model in which the interaction potential is complex. Such a complex potential accounts for a range of non-elastic processes, like inelastic scattering and nucleon transfer reactions. Nuclear reactions are generally divided into two extremes based on the energy involved in the reaction. On the low emission energy side a compound nucleus can form, while on the high emission energy side, direct reactions dominate the final state of the residual nucleus [Bur95].

1.1.1 Direct and compound reactions

Direct and compound reactions are also distinguished by the duration of the interaction. Direct reactions are considered relatively prompt (~ 10^{-22} s), i.e. having a reaction time which compares to the time it takes a projectile of a few MeV to traverse the diameter of the target nucleus. During direct reactions the final state is usually formed through a single-step interaction, not with the target as a whole, but with just a part of it, like a single nucleon in the surface. The cross section, which is related to the probability for a specific reaction, consists therefore primarily of the contribution of the overlap between the wave functions of the initial and final states. The resulting yield of reaction products is predominantly in the forward direction relative to the projectile.

If the projectile interacts with the target at its surface, i.e. a peripheral interaction, it is usually a simple direct collision. On the other hand, with sufficient energy the projectile can

penetrate into the interior of the target nucleus, colliding with several of the nucleons inside. We can therefore expect direct reactions to be more surfaced localised whereas compound nuclear reactions will be localised in the interior [Gle83].

During compound nuclear reactions the projectile is usually captured by the target and will share its energy with the nucleons inside. Such compound nuclei can live long enough for statistical equilibrium to be established (~10^{-16} s). Thereafter it is probable that a few nucleons or nucleon clusters may have enough energy to escape from the compound nucleus, much like the evaporation of energetic molecules from a liquid drop, until the excitation energy is below the particle emission threshold. The nucleus can then decay further to its ground state by the emission of gamma rays. One would therefore not expect any a-priori direction in the yield of emitted particles, but rather an isotropic angular distribution (see **Figure 1-1**).

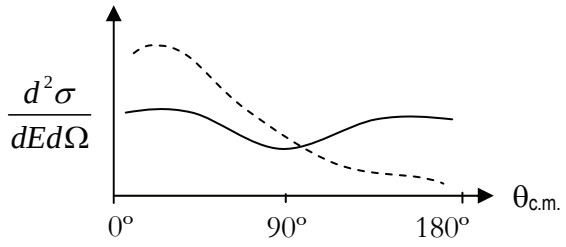

Figure 1-1: *Typical angular distributions of direct (dashed line) and compound (solid line) reaction cross sections.*

1.1.2 The Pre-equilibrium reaction

In the energy range between direct reactions, where discrete states in the residual nucleus are excited and little energy is transferred to the target, and large excitations where compound nuclei are formed, a continuum of ejectile energies is found where pre-equilibrium or statistical multi-step reaction models are applicable. This is illustrated in **Figure 1-2**.

In this region some reactions are characterised by a continuum (overlapping) of final states with isotropic cross-section distributions, consistent with compound nuclear processes, but with energy distributions containing more energetic particles than predicted. This suggests that the nuclear excitation takes place in a series of steps, and that emission can take place at an earlier stage before statistical equilibrium has been established. Pre-equilibrium reaction

models have been widely used to describe reactions in the energy range between 10 and 200 MeV. The basic pre-equilibrium model assumes that the reaction takes place through a sequence of steps characterised by the number of excited particle-hole pairs. Initially the incident particle is considered to be in a one-particle (1p) state in the continuum above the Fermi level. In the first step, the projectile can interact with one of the nucleons in the nucleus, creating a two-particle-one-hole (2p1h) excited state. In a second step another nucleon can be excited to create a three-particle-two-hole (3p2h) state, and so on. After any step one ore more particles can be ejected [Hod03].

Pre-equilibrium reaction theories are broadly divided into the two types, multi-step compound reactions (MSC) where all the particles remain bound, and multi-step direct reactions (MSD) where at least one particle, often the incident one, stays in the continuum. A number of pre-equilibrium theories to calculate both these processes have been developed. Of these, the theory of Feshbach, Kerman and Koonin (FKK) has been applied widely.

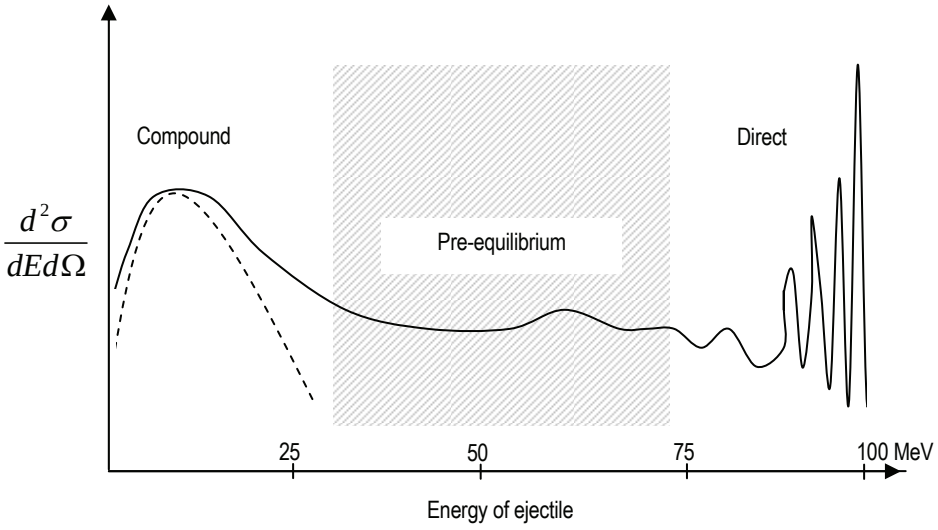

Figure 1-2: *Diagram roughly depicting a typical energy spectrum of ~100 MeV incident energy protons interacting with a target nucleus.*

In the case of the pre-equilibrium emission of light composite ejectiles, such as for example α-particles, two opposite reaction mechanisms have been suggested, the idea of pre-formed α-clusters, since it is such a strongly bound object (the binding energy per nucleon is ~7 MeV), and on the other hand, a coalescence model which assumes the cluster is formed during the course of the reaction [Hod03].

1.2 The importance of (p,α) reaction studies

The emission of nucleons due to the interaction of 80 – 200 MeV incident protons with a variety of nuclei has been successfully described by means of the statistical multi-step direct reaction formulation of FKK [Cow91], [Ste97], [Ric94]. Although many pre-equilibrium reaction studies have been conducted in the past, the processes involved in the emission of complex particles like helions and α-particles are, however, not understood to the same degree. The need for a better understanding of the relative contributions of different reaction mechanisms not only for nuclear structure research but in many nuclear applications, such as medical therapy with proton beams, transmutation of radioactive waste and the design of effective and safe materials for reactors, therefore still exists.

1.2.1 α-Clusters in nuclei

The existence of possible pre-formed α-clusters in nuclei have been studied extensively in the past. One of the most direct ways of investigating the existence of α-clustering in nuclei is by means of a direct knock-out reaction. The high stability of the α-particle would suggest that a cluster description involving a knock-out or pick-up reaction would be reasonable. The simplest method is probably that of the inclusive (p, α) reaction.

Many (p, $p\alpha$) coincidence reaction studies on a range of target nuclei from ^{6}Li to ^{66}Zn at incident energies between 100 MeV and 296 MeV have been conducted [Car84], [Nad81b], [Nad89], [Nev07], [Roo77], [Wan85], and [Yos98]. These studies employed the distorted wave impulse approximation (DWIA) which gave very good agreement with measured energy sharing differential cross sections. As mentioned by Neveling *et al.* [Nev07] the existence of pre-formed α-clusters could be confirmed if coincidence measurements of the cluster momentum distributions give results which agree with that expected by the theory for the interaction of nucleons with a bound cluster.

In the case of coincidence (p, $p\alpha$) reaction studies, as mentioned by Hodgson [Hod02], one can expect the cross sections and analysing powers to show similarities with that of free p-α interactions if indeed the reaction proceeds by the direct knock-out of a pre-formed α-

particle by the incident proton. This was confirmed by ^{9}Be (p, $p\alpha$) investigations done by Wang *et al.* [Wan85] (see section 5.1.1).

1.2.2 Multi-step reaction studies for (p,^{3}He) and (p, α)

Many studies involving the FKK theory have been done on pre-equilibrium reactions in which composite particles are emitted. Cowley *et al.* [Cow96], [Cow97] successfully described the (p, ^{3}He) and (p, α) reactions at incident energies between 100 and 200 MeV using the FKK multi-step theory where the final step for the former reaction was assumed to be a deuteron pick-up and in the case of the latter reaction, a knock-out process. The direct interaction cross sections were calculated with the distorted wave Born approximation (DWBA). It was found that reactions giving α-particles with the highest outgoing energies are dominated by a one-step process, and as the emission energy decreases, the contributions of the higher steps begin to dominate. As the incidence energy increases, the second- and higher order steps become more important.

In more recent work done by Cowley *et al.* [Cow02] the analysis of the inclusive (p,α) reaction was extended to include analysing power calculations on ^{59}Co at 100 MeV incident energy based on a simple α-cluster knock-out model. The study showed that the calculated analysing power distributions were consistent with a single-step knock-out mechanism at high emission energies. It has been argued that the (p, α) reaction, as opposed to the (p, ^{3}He) reaction, would not likely involve multi-nucleon pick-up, but rather that the emitted α-particle originates from a collision of either the incident proton or secondary scattered proton with a pre-formed α-cluster.

These studies show qualitative similarities in the cross section and analysing power distributions for the (p, α) and (p, ^{3}He) reactions which would suggest that the multi-step reaction formalism can be used to better understand the nature of the reaction mechanism that results in the emission of α-particles. Guided by these results it is reasonable to assume that an analysis of the (p, α) reaction in terms of a simple direct α-cluster knock-out model employing the DWIA will yield results that are indicative of the first-step contribution to the full reaction as clearly distinguished in the multi-step reaction studies.

1.2.3 Reaction mechanisms for (p, α)

The most likely direct reaction mechanisms for the (*p, α*) reaction are (i) triton (^{3}H) pick-up and (ii) *α*-cluster knock-out. Both have been treated theoretically to good approximation using cluster-transfer formalisms [Bon89], [Gad84]. It is still not clear to what degree the different nucleon transfer mechanisms contribute to nuclear reactions, and so both these mechanisms should be included in a full analysis of the reaction.

Based on the stability of the *α*-particle, with a binding energy per nucleon of ~7 MeV compared to that of a triton cluster which is ~2.6 MeV, it is conceivable that a medium energy proton will knock it out as a stable cluster. The triton pick-up model assumes that the incoming proton interacts with a pre-formed three-nucleon cluster on its way through the nucleus. Intuitively this probability decreases with increasing incident energy as higher energy projectiles will likely break the relatively unstable cluster.

At low excitation energies the (*p, α*) reaction mostly creates discrete states in the residual nucleus which have been studied using both pick-up and knock-out, while at higher excitation energies, the reaction tends to excite unresolved continuum states. Demetriou and Hodgson [Dem96] successfully described the contribution of the direct component in the cross sections of (*p, α*) reactions to the continuum by the FKK theory of pre-equilibrium emission using an *α*-particle knock-out model.

Studies by Gadioli *et al.* [Gad84] of the (*p, α*) reaction at low incident energies of ~20 – 30 MeV to discrete states of the residual nucleus, indicated that a clear distinction between the pick-up and knock-out models cannot be made simply on the bases of the angular distributions or analysing powers at these energies. It also showed again a strong dependence on the total orbital momentum of the *α*-particle.

Calculations made by Bonetti *et al.* [Bon89] on the ^{58}Ni(*p,α*) reaction at 72 MeV to continuum final states showed very different analysing power values for pick-up and knock-out. The experimental data definitely favoured the knock-out mechanism.

1.3 The aims and scope of this study

This study aims to investigate the inclusive (p, α) reaction at incident energies of 100 MeV and 160 MeV and compare the measured double differential cross section and analysing power distributions with distorted wave impulse approximation (DWIA) calculations using a simple direct α-cluster knock-out mechanism. It is assumed that the single-step knock-out process is the dominant process in the region of small α-emission angles and low excitation energies.

The single-step direct cluster knock-out mechanism is probably one of the simplest reaction models and although more sophisticated model calculations have been successfully performed with pre-equilibrium multi-step formalisms, it is still very important to understand to what extent this simple model is able to describe the emission of high energy α-particles.

An experiment was conducted at iThemba LABS for the $^{93}Nb(\vec{p},\alpha)$ reaction at an incident proton energy of 160 MeV. Experimental double differential cross section and analysing power data were obtained and analysed for laboratory angles of 15º, 20º, 25º, 30º, 35º, 40º, 50º and 60º and for α-particle energies ranging from 30 to 154 MeV in 4 MeV steps. Recorded data for the inclusive $^{93}Nb(\vec{p},{}^{3}He)$ reaction have also been analysed and are presented in the appendix.

Theoretical double differential cross section and analysing power values were calculated with the computer code THREEDEE by Chant [Cha3D]. This code employs the DWIA formalism, introduced by the author of the code [Cha77], for a direct α-particle knock-out. The calculations were compared with the available $^{93}Nb(\vec{p},\alpha)$ and $^{59}Co(\vec{p},\alpha)$ data at incident energies of 100 and 160 MeV.

The experimental setup for the $^{93}Nb(\vec{p},\alpha)$ and $^{93}Nb(\vec{p},{}^{3}He)$ reactions is outlined in chapter 2. Chapter 3 deals with the experimental procedures and the final analysis of the measured data. The theoretical framework for modelling the reaction is discussed in chapter 4 as well as the procedures and parameters used for the computer code. In chapter 5 the experimental cross section and analysing power distributions are presented with some

comparisons with the calculations done with THREEDEE. The results of a few test calculations are first presented. The last chapter gives a short summary of the conclusions reached in the study. An appendix is provided at the end of the thesis with some derivations and details that relate to this study. The experimental data for the ^{93}Nb (p, α) and ^{93}Nb (p, ^{3}He) reactions which were analysed during this study are presented here in tabulated form.

CHAPTER 2 THE EXPERIMENT

During 2006 experiments were performed at iThemba LABS (Laboratory for Accelerator Based Sciences) near Faure in the Western Cape, South Africa, with the purpose of investigating the inclusive (p, α) reaction at a beam energy of 160 MeV on a ^{93}Nb target. Data were simultaneously obtained for the inclusive (p, ^{3}He) reaction.

This chapter describes the basic experimental setup and procedures for the acquisition of data for the (p,α) and (p, ^{3}He) reactions. The description follows closely that of Bezuidenhout [Bez06] who did a similar experiment at beam energies of 130 and 160 MeV on ^{59}Co and ^{93}Nb during 2001 and 2003. Similar techniques were also employed in the study by Cowley *et al.* [Cow00]. More details on the accelerator and facilities as shown in **Figure 2-1**, have been given by Pilcher *et al.* [Pil89].

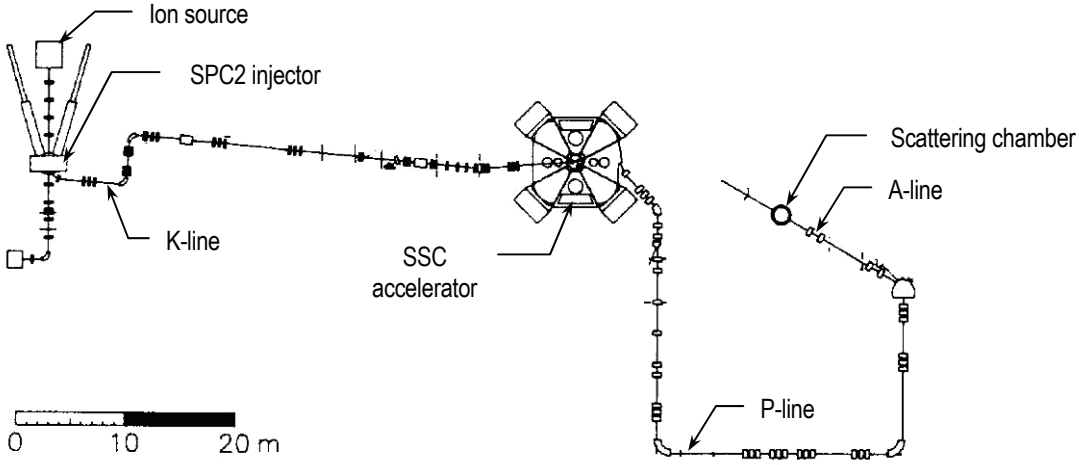

Figure 2-1: *The layout of the cyclotrons and facilities at iThemba LABS showing the beam line used in the experiments.*

2.1 Scattering Chamber

The experiments were performed in a 1.5 m diameter scattering chamber situated in one of the facility's research vaults, which is served by the A-section beam line. The scattering chamber is evacuated to a pressure of below 10^{-5} mbar in three stages by means of a system that consists of a rotary pump, a turbo molecular pump and a liquid helium cryogenic pump, operating at below 24 K.

Inside the chamber, two separately movable telescope arms support the various detectors and preamplifiers (see **Figure 2-2**). The telescope arms can be positioned by remote control at various angles to the left and right of the incident beam direction.

The different target foils (listed in **Table 2-1**) are mounted on a target ladder and placed at the centre of the scattering chamber on a movable frame which can be remotely operated, like the telescope arms, from the data room. During the experiment, different targets are selected by moving the ladder up or down to pre-defined target positions. The angle between the normal of the targets and the beam direction can also be adjusted if needed. For this experiment the target angle was kept at zero.

Protons, polarised in the direction normal to the scattering plane, were provided by a hydrogen ion source. The proton beam is initially accelerated to about 6.7 MeV by a solid-pole injector cyclotron (SPC2) and then to the desired 160 MeV by the main separated-sector cyclotron (SSC). The polarisation was switched at the ion source between the up and down direction at regular 10 second intervals. This technique serves to minimise systematic errors. An average beam polarisation of between 65% and 85% was maintained during the experiments.

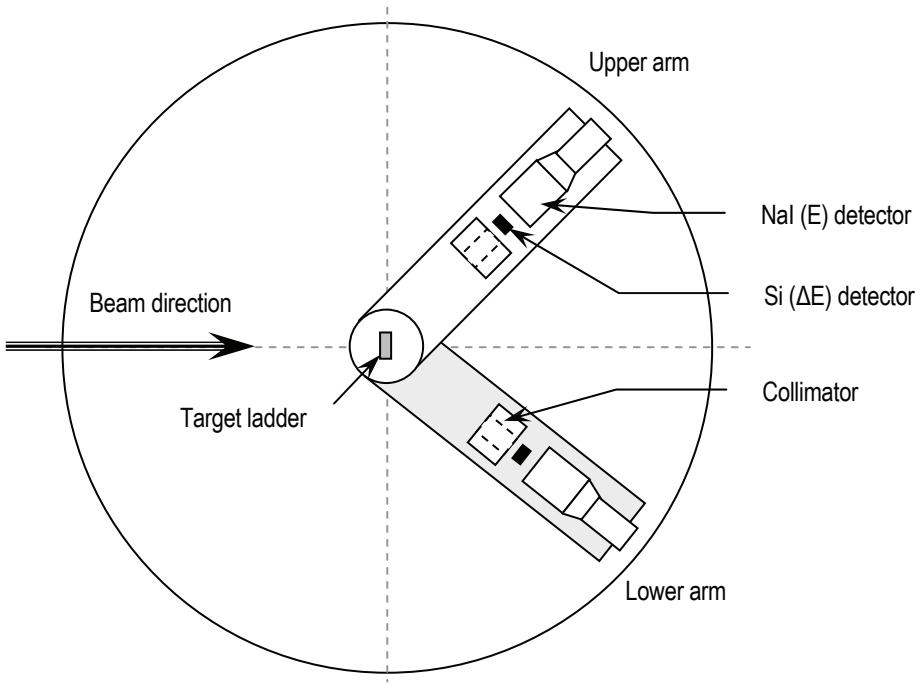

Figure 2-2: *Diagram showing top view of the scattering chamber with the upper and lower telescope arms inside.*

2.2 Targets

The target ladder contained two ^{93}Nb target foils, one ^{59}Co foil, a ^{12}C target for calibration, beam offset and polarisation measurements, a Al_2O_3 scintillating "ruby" used to view the beam spot, and an empty frame for investigating possible beam halos. The Nb and Co targets were self-supporting metal foils with a 100% occurrence of the desired isotopes. The thicknesses of the different targets are listed in **Table 2-1**. These targets are the same as those used by Bezuidenhout [Bez06], who gives the uncertainty in the thicknesses of the targets as less than 7%.

Target	*Thickness [mg/cm^2]*
^{93}Nb (3 μm)	2.57 ± 0.17
^{93}Nb (10 μm)	8.57 ± 0.52
^{59}Co (10 μm)	8.90 ± 0.62
^{12}C	0.100

Table 2-1: *Target thicknesses*

2.3 Detector Telescopes

Each of the two detector telescopes consisted of a 500 μm Si surface-barrier detector used as an energy loss (ΔE) detector, and a standard 76 mm × 127 mm NaI(Tl) scintillation detector which serves as an energy stopping (E) detector. The Si detector was mounted in a Teflon holder just behind a thick brass collimator (See **Figure 2-3**). The NaI(Tl) detectors were positioned behind the Si detectors on a separate stand. The NaI detectors were fitted with a light-emitting diode (LED), embedded inside the NaI crystal. A pulser signal can be sent to the LED at regular intervals, and the resulting detector signal recorded in a separate spectrum. The pulser signal was used to monitor possible gain drifts by the photomultiplier tube behind the crystal.

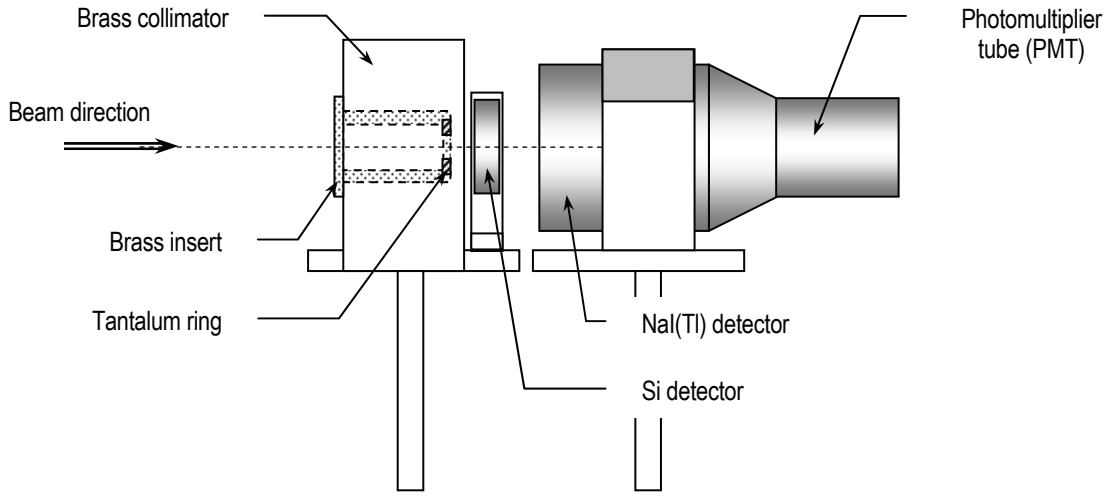

Figure 2-3: *Side view of a telescope setup showing the collimator and Si and NaI(Tl) detectors.*

The collimators consisted of a 43 mm thick and 66 mm wide brass block with a separate brass insert. A 3.15 mm thick tantalum ring, with a 14.1 mm diameter hole in the middle, was inserted into the back of the brass insert, as illustrated in **Figure 2-3**. The collimators thus defined an acceptance solid angle of 1.13 msr (see the appendix for the dimensions and calculation). The brass collimators were covered at one end with a thin (8 μm) Kapton film to prevent any stray fast electrons from entering and damaging the Si detectors.

The sensitive depth of the two Si detectors is given as ~ 528 μm with Au and Al dead layers of 0.021 and 0.15 μm respectively. A 7-μm Havar entrance window covers the NaI crystals. The total energy loss of helions and α-particles as they pass through these layers and detectors were calculated with the computer code KINMAT (which runs on the computer network at iThemba LABS), and used for the energy calibration of the NaI detectors. The calibration procedure is discussed in more detail in chapter 3.

2.4 Electronics

The basic electronic setup for the linear and timing signals from the detectors to the data acquisition system is briefly outlined in this section. A more detailed discussion can be found in the references [Bez06], [För92] and [Ste97].

All the signals to and from the scattering chamber are connected to a patch panel in the scattering chamber vault and relayed to a similar panel in the data room. These consist of high voltage power supplies, energy and timing output signals, and pulser input signals.

2.4.1 Linear signals

Energy signals from each of the four detector preamplifiers are fed into and shaped by a linear amplifier. The uni-polar output from these amplifiers are delayed and sent to a linear gate and stretcher (LGS) module where the signal is only allowed through if the desired logic conditions are met. This is discussed further in the next section. The accepted energy signals are then digitised by an analogue-to-digital converter (ADC). **Figure 2-4** shows the block diagram for the linear and logic signals for one of the telescopes.

2.4.2 Logic signals

Timing signals from the detectors are used to determine valid coincidence events between the ΔE and E signals on each detector telescope on a hardware level. The fast timing signals from the output of each detector preamplifier are further amplified and shaped by a timing filter amplifier (TFA) and then fed into a constant fraction discriminator (CFD). At this point the timing signals from the ΔE and E detectors on one telescope arm are fed into a 4-fold logic unit (4-FLU) where only signals meeting the logic condition ΔE AND E, are allowed through, i.e. for an event to be valid it must trigger both the Si and NaI detectors on the same telescope. For this reason the timing signal from the E detector is stretched ~ 10× wider in time by the CFD than the signal from the ΔE detector, which is delayed for about 100 ns. Any timing jitter in the fast signals is then taken into account by means of the wider timing signal. A busy signal from the event trigger (see section 2.4.3) vetoes the 4-FLU when the system is still busy processing a previous event. For every valid event the relevant signal is counted by a scaler.

2.4.3 Pattern registers and event trigger

Every time a signal is received which satisfies the specific logic condition for a valid event, an event trigger signal is sent to the data acquisition hardware. Each different type of event, e.g. a signal in the left or right detector telescope, the polarisation direction specified by a signal from the polarised ion source, a pulser signal etc., is registered in a pattern register module. This allows identification of the nature of the particular event. Once all the data for an event have reached the pattern register, a strobe signal initiates the readout from the pattern register by the data acquisition program.

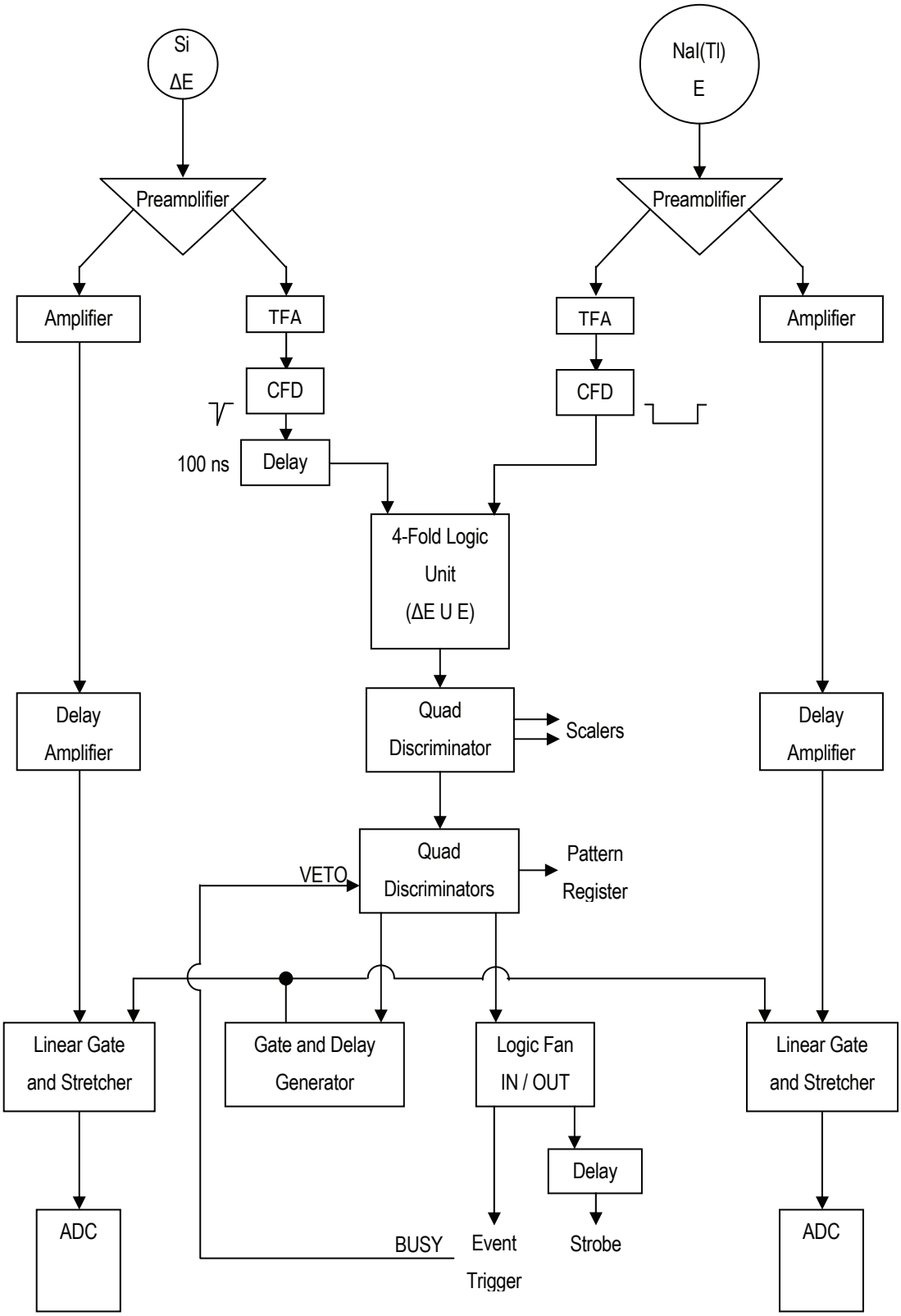

Figure 2-4: *Electronic block diagram for the linear and logic circuitry for one of the detector telescopes.*

2.4.4 Current integrator and dead time

The total accumulated charge, detected on the beam stop, is given by the current integrator (CI) unit, which sends pulses to a designated scaler input, CI-UN (uninhibited). Each pulse in the CI scaler represents a charge of $R \times 10^{-3}$ nC, where R is the range setting (in nA) on the CI unit. In order to measure the dead time of the system, a separate signal from the CI is vetoed by the computer busy signal and sent to a separate scaler input, CI-IN (inhibited). The ratio of CI-IN and CI-UN gives the computer dead time.

2.4.5 Computer interface and hardware

The signals from the different ADC, scaler, pattern register and event trigger modules were interfaced to a VAX workstation via a VME system. The data acquired during the on-line runs were stored event by event on hard disk for later off-line replay.

2.5 Data acquisition software

Data acquisition is managed by a data acquisition program (DAQ), called XSYS which runs on the VAX/VMS computers at iThemba LABS. The DAQ contains instructions (EVL and COM files) by which data from the registers and scalers in the VME interface is read off. A specific EVL file for this type of experiment, which controls the storing and filtering of event data on a software level, has been compiled using an Event Analysis Language (EVAL) code. In the EVAL code various data areas are initialised for storing spectra and setting gates.
Table 2-2 lists the most relevant data areas as defined in the EVAL code. The data of each run are stored in a separate event (EVT) file.

The following outlines the basic flow of logic in the EVAL code. Once the program has initialised all the variables and spectra, it tests for a valid event in the left/right telescope. A signal from the pattern register specifies whether the polarisation of the event is up or down. In order to obtain the magnitude of the polarisation, a one-dimensional gate is set around the elastic peak in the spectrum of data area 30/31. Events within this gate are added to the appropriate data areas (40 – 43) and the relevant scalers are incremented (see **Table 2-2**). Next the program corrects for any gain drifts seen in the raw spectra of the NaI detectors. This is done by calculating the centroid of the pulser signal for 100 pulser events and comparing it to that of the previous 100 events. The relevant NaI detector is then recalibrated according to the new gain.

Area	*Name*	*Description*
30(31)	POL**L**(**R**)dc	Drift-corrected energy spectrum for left/right telescope. Gates are set around the elastic peak for polarisation measurements.
40(41) 42(43)	POL**L**U(D) POL**R**U(D)	Data areas for valid polarisation-up or -down events in the left and right telescopes.
60(62)	TL(R)**A**raw	Raw energy spectrum for the Si detector on the left/right telescope.
61(63)	TL(R)**B**raw	Raw energy spectrum for the NaI detector on the left/right telescope.
71(74)	TL(R)**B**puls	Raw energy spectrum for the NaI detector on the left/right telescope showing pulser signals.
72(75)	TL(R)**B**pdc	Energy spectrum for the NaI detector on the left/right telescope showing pulser signals after automatic drift correction.
80(81)	TL(R)AB	ΔE vs. E spectrum for the left/right telescope. Two-dimensional spectrum for particle identification. Gates are set around particle loci.
91(92) 94(95)	E**L**A_U(D) E**R**A_U(D)	Calibrated energy spectrum for **α-particles** in the left telescope when the beam polarisation is up/down. Similarly for the right telescope.
101(102) 104(105)	E**L**H_U(D) E**R**H_U(D)	Calibrated energy spectrum for **helions** in the left telescope when the beam polarisation is up/down. Similarly for the right telescope.
990	SCALERS	Readout of the scalers as displayed on the STATUS screen.

Table 2-2: *Relevant data areas defined in EVAL code.*

The following steps in the code identify events in the left and right telescopes. For example, if a valid event is identified in the left telescope, i.e. the necessary logic conditions have been met, data areas TLAraw, for the Si detector, and TLBraw, for the NaI detector, are incremented. These spectra are then calibrated with the given calibration parameters, which were determined during the calibration runs, see section 3.1, and stored in new spectra. The different types of particles (α-particles or helions) are distinguished by setting two-dimensional gates around loci in the ΔE versus E spectrum. This procedure is discussed in more detail in section 3.3. The final eight data areas that are extracted for cross section and analysing power calculations, are EL_AU(D), ER_AU(D) for the α-particles in the left and right telescope and for beam polarisation up and down, and EL_HU(D), ER_HU(D) for helions in the left and right telescope and for beam polarisation up and down.

2.6 Experimental procedures

The experiment was performed over several weekends. At the beginning of each weekend the detectors were recalibrated. The Si detectors were calibrated with the use of a radioactive α-source, while the NaI detectors were calibrated using the kinematics of elastic and inelastic scattering of unpolarised protons from a ^{12}C target.

Data runs of about two hours were taken at a time, with a polarisation measurement of a few minutes in between each run. For the polarisation measurements the detector arms were moved to a specific angle and data accumulated until the error in the average polarisation was below 10%.

2.6.1 Beam offset

The angular offsets on the shaft encoder readouts for each telescope arm, relative to the incident beam direction, were also determined before the start of each weekend using the elastic scattering of unpolarised protons from the ^{12}C target. This was done for each arm separately by comparing the number of elastic events in the detector when it is at equal angles to the left and right of the beam.

The true lab angle, θ_{lab} , relative to the incident beam direction, is determined from the relation

$$\theta_{readout} = \theta_{lab} - \theta_{offset}$$

where the offset is positive/negative if the beam is to the left/right of the shaft encoder's zero position, i.e. the beam is "off set" to an angle of θ_{offset} anti-clockwise/clockwise from the beam direction.

2.6.2 Polarisation measurements

The polarisation of the incident beam was measured in (i) the scattering chamber and (ii) the polarimeter in the K section of the beam line, just after the SPC2 accelerator.

i. Scattering chamber

Polarisation measurements were performed in the scattering chamber at regular intervals during the experiment using the elastic scattering of protons from ^{12}C. The two detectors telescopes are positioned at equal angles to the left and right of the incident beam direction and record the number of elastic events in each ($N_L^{\uparrow/\downarrow}$ and $N_R^{\uparrow/\downarrow}$) when the beam is in the spin-up(↑)/spin-down(↓) orientation.

The elastically scattered events were identified by setting a one-dimensional gate around the elastic peak in the drift-corrected spectrum of the NaI detectors, data areas 30 and 31 (see **Table 2-2**). **Figure 2-5** shows the gate in the spectrum for one of the detectors. The measurements were taken with the detectors at equal angles, corresponding to a local maximum in the analysing power, A_y. Values of Meyer *et al.* [Mey83] for the ^{12}C(*p, p*)^{12}C elastic scattering at incident lab energies of 122 and 160 MeV were used. At these two energies, the first maxima in analysing power are found at θ_{lab} = 25° (A_y = 0.71) and θ_{lab} = 19° (A_y = 0.92) respectively.

With the known analysing power value at the set detector angle, the polarization up, $p_\uparrow$ and polarization down, $p_\downarrow$ can be determined from [Hae74]

$$p_{\uparrow/\downarrow} = \frac{1}{A_y} \cdot \frac{N_L^{\uparrow/\downarrow} - N_R^{\uparrow/\downarrow}}{N_L^{\uparrow/\downarrow} + N_R^{\uparrow/\downarrow}}. \qquad (2.6.1)$$

The derivation of equation (2.6.1) is discussed in more detail in section 4.3.

ii. K-line polarimeter

Beam polarisation is measured in the K-line polarimeter, situated just after the injector cyclotron, as part of the setup and tuning of the ion source and beam. The polarimeter consists of a ^{4}He-gas cell target with two 150 μm Si detectors at equal angles of 110° to the beam direction. Polarisation is determined from the known analysing power for the elastic ^{4}He(*p, p*)^{4}He reaction at the beam energy of about 6.7 MeV.

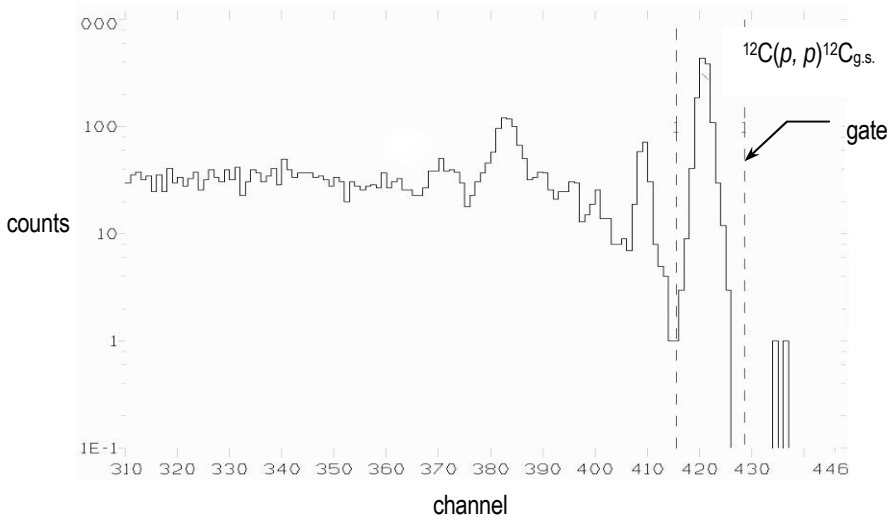

Figure 2-5: *Spectrum of data area 31(POLRdc) showing the one-dimensional gate set around the elastic peak of the reaction ^{12}C(p, p)^{12}C during polarisation measurements in the scattering chamber.*

CHAPTER 3 DATA ANALYSIS

This chapter deals with the analysis of the experimentally measured data during the off-line replay using the EVAL codes similar to that used in the on-line process. A brief description of the calibration procedure for the different detectors is first given. The section thereafter discusses the setting of gates and the techniques used for particle identification. Sections 3.4 and 3.5 describe the calculation of the experimental double differential cross sections and analysing powers. A discussion on the error analysis is also provided. The results of the experimental analysis are given in chapter 5.

3.1 Calibration of the detectors

3.1.1 Si detectors

For the calibration of the Si detectors, a radioactive ^{228}Th source was placed close to the detectors inside the scattering chamber prior to the experiment. The known energies of the α-particles emitted in the Th source and its decay products are given in **Table 3-1**. Since the Si detectors are used as energy loss detectors, the energy range over which calibration is done depends on the amount of energy the protons and α-particles, emerging from the target during the experiment, lose. The minimum energy loss of a 160 MeV proton in a 500 μm Si detector is ~0.5 MeV, while protons of ~10 MeV will be completely stopped in the active layer of the detector. The 500 μm detector is therefore able to fully stop the α-particles from the calibration source.

Energy of α-particle [MeV]						
5.34	5.42	5.68	6.05	6.29	6.78	8.78

Table 3-1: *Energies of the α-particles emitted by a ^{228}Th source.*

From the detector spectrum the α-particle peaks were identified and their centroid channel numbers plotted against the known energies. A linear fit to the data provided the calibration parameters. **Figure 3-1** shows an example of such a calibration curve. The gradient and intercept values are used in the EVAL code when replaying the data.

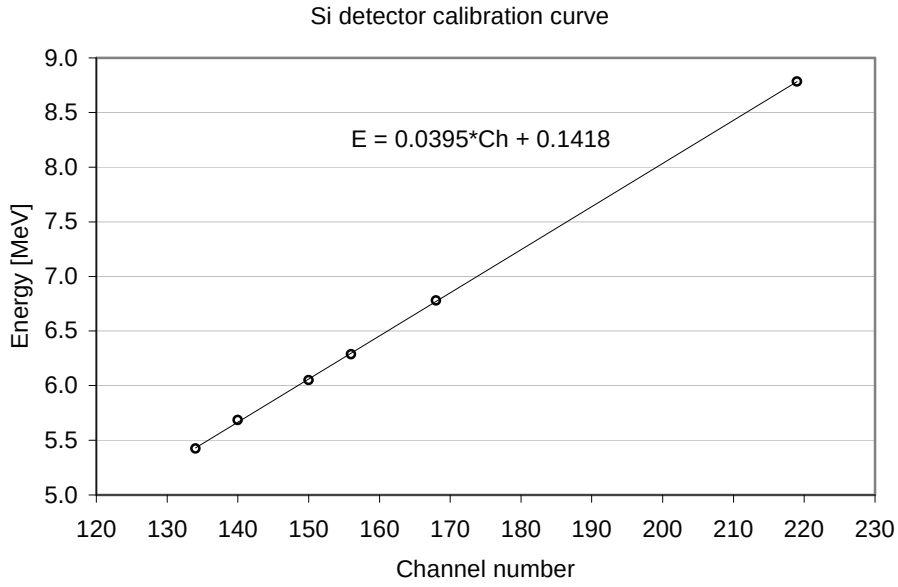

Figure 3-1: *Calibration curve for one of the Si detectors showing a linear fit.*

3.1.2 NaI(Tl) detectors

The NaI(Tl) detectors are calibrated using the elastic and inelastic scattering of protons from the ^{12}C target. The ground and first excited states of ^{12}C are clearly resolved as seen in the raw NaI spectrum in **Figure 3-2**.

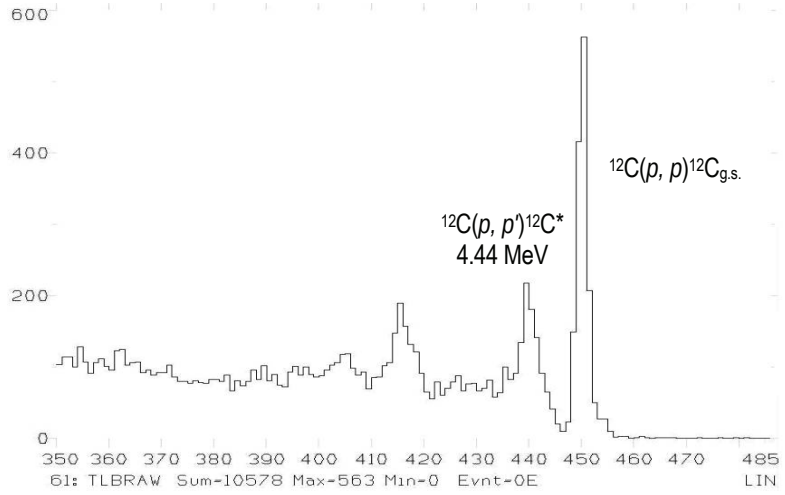

Figure 3-2: *Raw energy spectrum for a NaI detector showing the ground and first excited states of ^{12}C as the two prominent peaks on the right end of the spectrum.*

Using the computer program KINMAT, the energy of a 160 MeV proton as it scatters through an angle of 19º can be determined. The subsequent energy loss in the Si detector, Kapton shield and Havar entrance window in front of the NaI detectors is then calculated with the program ELOSS. The final energy of the protons as observed in the NaI detector is given in **Table 3-2**.

Projectile energy [MeV]	*Energy loss in Kapton and Havar [MeV]*	*Energy loss in Si [MeV]*	*Final energy in NaI [MeV]*
158.353	0.025	0.495	157.83
153.973	0.025	0.505	153.44

Table 3-2: *Calculated energy of protons from the elastic and first excited states of ^{12}C used in the calibration of the NaI detectors at an incident energy of 160 MeV and detector angle of 19º.*

The calibration was based on the ground and first excited states of ^{12}C. A linear fit was drawn through these two points as well as the origin of the energy versus channel graph. The choice of the origin is to ensure that channel zero corresponds to zero energy. An example of such a calibration curve is shown in **Figure 3-3**.

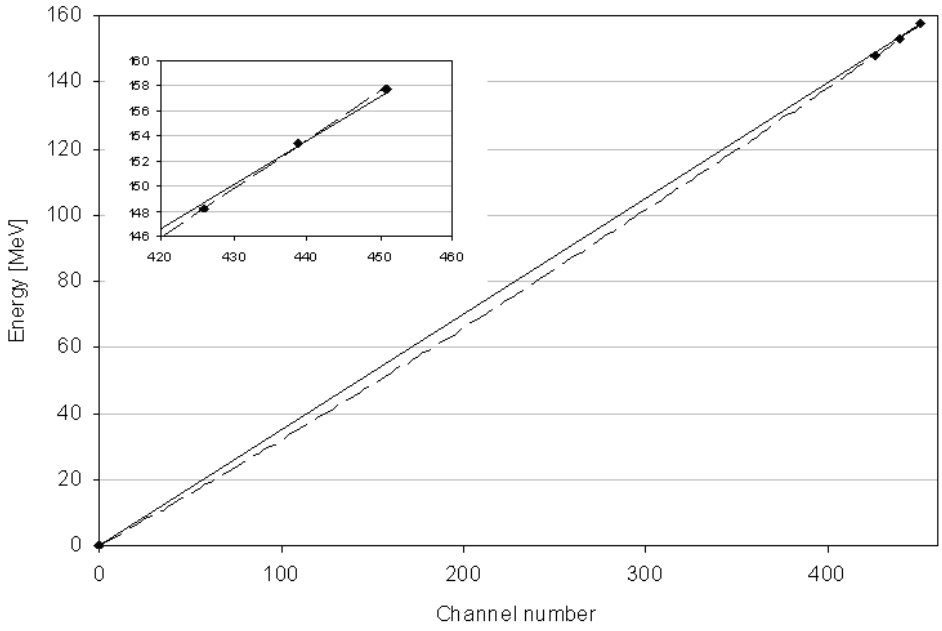

Figure 3-3: *A calibration curve for one of the NaI(Tl) detectors showing the linear (---) and second order polynomial (- - -) fit to the data. The insert is an enlargement of the upper right hand corner of the graph.*

The figure shows the linear fit with an average difference between the fit and the data of about 0.2%. This is slightly less than the ~0.3% uncertainty in the centroid channel number. Also shown in the figure is a second order polynomial fit which represents the data points even better with an average difference of less than 0.1%. The maximum difference between these two fits is less than 4 MeV.

The response of the NaI detectors to α-particles is, however, different from that of protons. Based on the maximum energy of the α-particles detected at the smallest emission angle, the calibration done with protons is considered to be adequate, differing with less than 4% from the theoretically calculated value.

3.1.3 Gain drifts

The gain of the photomultiplier tube on a NaI(Tl) detector tends to change (drift) during the course of an experiment due to factors such as a change in count rate [Kno89]. To correct for this, a pulser signal is sent to the LED, embedded in the NaI crystal, at regular intervals. The position of the pulser peak in the energy spectrum at the beginning of the weekend was used as a reference point for calibration. A separate gate was set around this initial pulser position. Any drifting of the pulser position is then automatically corrected for in the EVAL code and stored in a drift-corrected data area.

3.2 Setting of gates

During the off-line replay of the data, certain gates need to be set around regions in spectra as part of the sorting of the events in the software. One-dimensional gates are set around the initial pulser position in all the raw NaI detector spectra (data areas 71 – 75) to track any gain drifts, as discussed in the previous section. For polarisation measurements, one-dimensional gates are set around the elastic peak in the drift-corrected spectra for the left and right NaI detector (data area 30 and 31). Lastly, two-dimensional gates are drawn around particle loci in the mass-function spectra for the left and right telescope. This is discussed further in the next section.

3.3 Particle identification

Particle identification (PID) is done using the standard ΔE-E technique. A spectrum is generated of the energy loss of a particle in the ΔE detector as a function of its energy loss in the E detector. According to the Bethe formula, [Kno89]

$$-\frac{dE}{dx} = \frac{4\pi e^2 q^2}{m_e v^2} NZ \left[\ln \frac{2m_e v^2}{I} - \ln\left(1 - \frac{v^2}{c^2}\right) - \frac{v^2}{c^2} \right], \tag{3.3.1}$$

the energy loss of a charged particle in a medium is, to first order in v, its initial velocity, proportional to its mass and charge squared, and inversely proportional to its initial energy, i.e.

$$-\frac{dE}{dx} \propto \frac{mq^2}{E}.$$

In equation (3.3.1) m_e and e represent the mass and the charge of an electron respectively, q represents the charge of the primary particle, and N and Z represent the number density and atomic number of the absorber. The quantity I is a parameter for the average excitation potential for the atoms of the absorbing material.

Particles with different mass and charge will therefore lose different amounts of energy in the ΔE and E detectors. The different types of particles will form different loci on the two-dimensional ΔE versus E spectrum (see **Figure 3-4**). As can be seen in the ΔE versus E spectrum, it can be difficult to set a clear gate around the different particle loci. It is therefore more convenient to generate a mass function, M. The mass function transforms the hyperbolic shape of the particle loci into a more linear form. The mass function is calculated from the expression [Bez06],

$$M = \left(E_{total}^{Y} - E_{NaI}^{Y}\right) X + Z \tag{3.3.2}$$

where the constants X, Y and Z are adjusted to enhance the separation of the different particle loci. From the mass function spectrum the two-dimensional gates are set around each particle locus, as can be seen in **Figure 3-5**. The upper gate is set around the α-particle region, while the bottom gate is around the helions. With the PID gates in place, the event data is replayed.

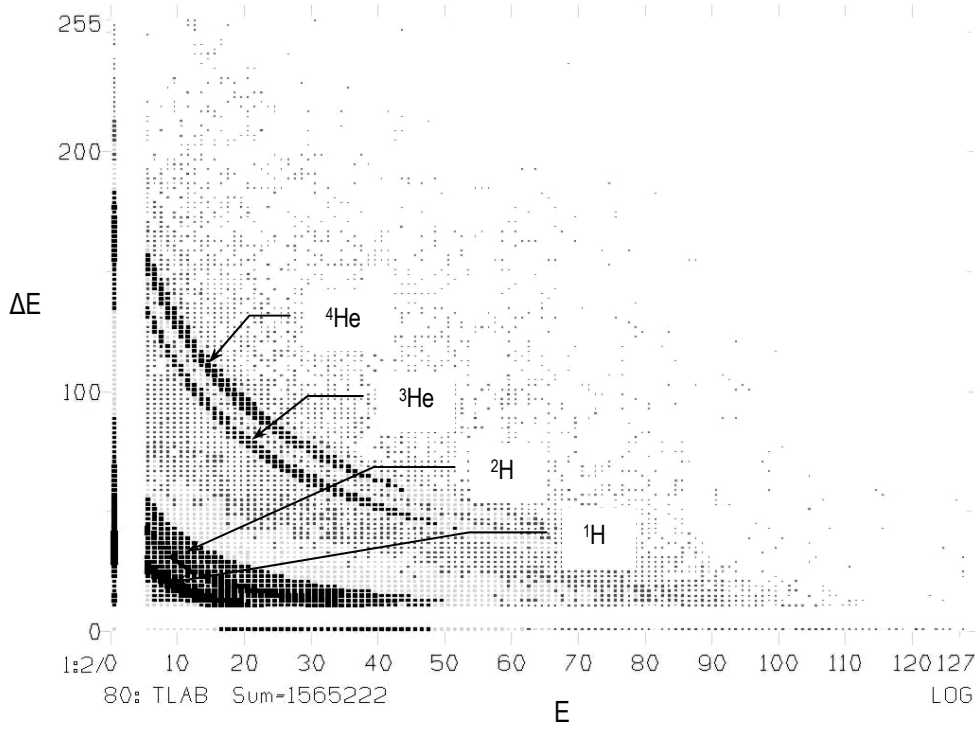

Figure 3-4: *Particle identification (PID) spectrum showing the loci for α-particles and helions at the top, data area 80.*

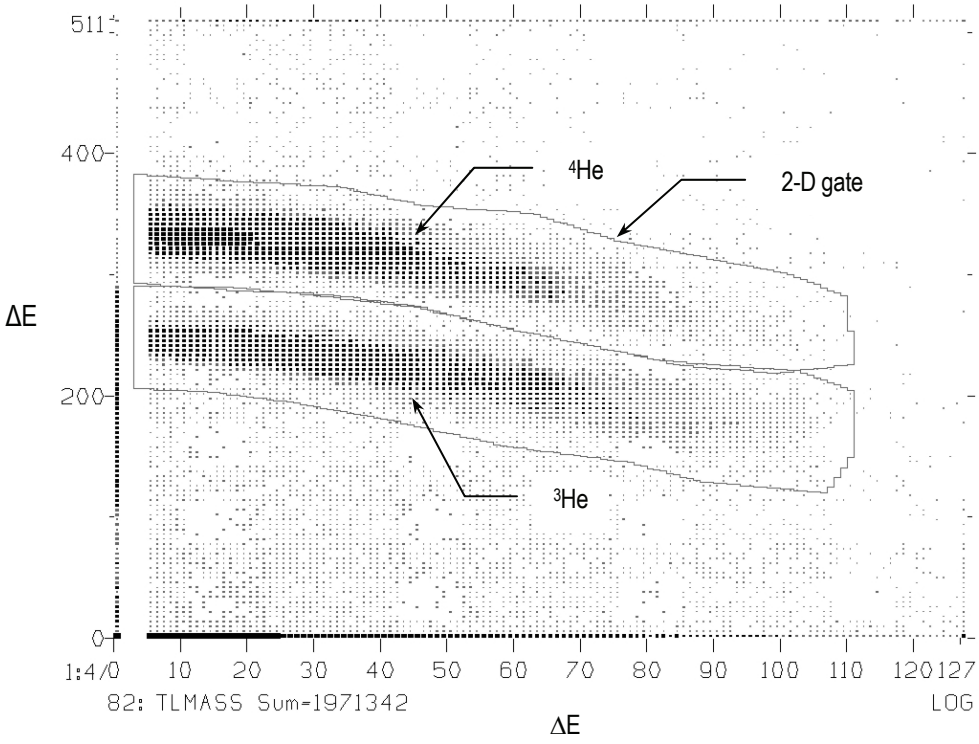

Figure 3-5: *Mass function spectrum with two-dimensional gates set around α- (top) and helion (bottom) loci, data area 82.*

3.4 Double differential cross section calculations

The double differential cross section, at different scattering angles, is calculated from the number of counts in the energy spectra. It is simply defined as the ratio of the number of particles that reacted per second per unit solid angle and energy, to the incident particle flux, i.e. the number of incident particles per unit area per second.

The double differential cross section (in mb sr^{-1} MeV^{-1}), for a specific detector telescope, left or right, is therefore given by

$$d^2\sigma \equiv \frac{d^2\sigma}{d\Omega dE} = \left(\frac{10^{27}}{n}\right)\frac{N_c}{N_0 \Delta\Omega\, \Delta E} \tag{3.4.1}$$

where

N_c is the corrected number of counts in the energy bin ΔE, which takes into account the detector-specific properties like efficiency,

$\Delta\Omega$ is the solid angle (in srad) subtending the ΔE-E telescopes,

ΔE is the width of the energy bins (in MeV), usually taken as 4 MeV,

N_0 is the total number of protons incident on the target, given by

$$N_0 = \frac{N_{CI} \cdot R \cdot 10^{-12}}{q_p} \tag{3.4.2}$$

where

N_{CI} is the scaler reading on the current integrator (CI) unit. Dead time is automatically taken into account by inhibiting the CI by a data-acquisition busy signal,

R is the selected range of the CI unit. A range of R represents a current of $R \times 10^{-3}$ nA, i.e. the total charge collected on the beam stop (in nC), is $N_{CI} \times R \times 10^{-3}$,

q_p is the charge of a proton ($1{,}6 \times 10^{-19}$ C),

n is the number of nuclei per unit area of the target (in cm^{-2}) and is calculated from

$$n = \frac{N_A t_\rho}{A \cos\theta_T} \tag{3.4.3}$$

where

t_ρ is the target density thickness (in g/cm^2),

N_A is Avogadro's number,

A is the atomic mass of the target (in g/mol),

θ_T is the angle between the normal to the target and the beam line.

During the experiment the direction of the beam polarisation was switched every 10 seconds. As derived in equation (7.2.2) in the Appendix, the absolute double differential cross section, $d^2\sigma_0$, is then written in terms of the left, spin up ($d^2\sigma_L^{\uparrow}$) and spin down ($d^2\sigma_L^{\downarrow}$), and right, spin up ($d^2\sigma_R^{\uparrow}$) and spin down ($d^2\sigma_R^{\downarrow}$) double differential cross sections as

$$d^2\sigma_0 = \tfrac{1}{4}\left(d^2\sigma_L^{\uparrow} + d^2\sigma_L^{\downarrow} + d^2\sigma_R^{\uparrow} + d^2\sigma_R^{\downarrow}\right). \tag{3.4.4}$$

Since the differential cross section is just proportional to the number of counts in an energy bin, N, the absolute double differential cross section can be calculated from

$$d^2\sigma_0 = F\left(N_L^{\uparrow} + N_L^{\downarrow} + N_R^{\uparrow} + N_R^{\downarrow}\right) \tag{3.4.5}$$

with the factor

$$F = \frac{10^{27}}{4N_0\, n\, \Delta\Omega\, \Delta E}.$$

The symbol $N_{L/R}^{\uparrow/\downarrow}$ represents the number of counts detected in the telescope on the left (L) or right (R) when the polarisation of the incident beam is in the up ($\uparrow$) or down ($\downarrow$) directions. For identical telescope arm setups, the factor F is common to both detector telescopes.

3.5 Analysing power calculations

The analysing power for a specific angle, $A_y(\theta)$, is calculated from equation (7.2.3) in the Appendix:

$$A_y(\theta) = \frac{2}{\left(p_\uparrow + p_\downarrow\right)} \frac{d^2\sigma_L^\uparrow + d^2\sigma_R^\downarrow - d^2\sigma_L^\downarrow - d^2\sigma_R^\uparrow}{d^2\sigma_L^\uparrow + d^2\sigma_R^\downarrow + d^2\sigma_L^\downarrow + d^2\sigma_R^\uparrow} \tag{3.5.1}$$

where $d^2\sigma_{L/R}^{\uparrow/\downarrow}$ represents the double differential cross section for either the left or right telescope when the incident beam polarisation is up or down.

As shown in the derivation of the absolute double differential cross section in equation (3.4.5), in terms of the number of counts per energy bin, the analysing power can be written as

$$A_y = \frac{2}{\left(p_\uparrow + p_\downarrow\right)} \left(\frac{N_L^\uparrow + N_R^\downarrow - N_L^\downarrow - N_R^\uparrow}{N_L^\uparrow + N_R^\downarrow + N_L^\downarrow + N_R^\uparrow} \right) \tag{3.5.2}$$

where, since the analysing power is expressed as a ratio of counts, the common factor in the cross sections cancels out.

As a check, similar analysing power values were found using the expression given by Lewandowski *et al.* [Lew82]

$$A_y = \frac{(r+1)\left(p^\uparrow + p^\downarrow\right) - \sqrt{\Delta}}{2p^\uparrow p^\downarrow (r-1)} \tag{3.5.3}$$

where

$$r = \frac{N_L^\uparrow N_R^\downarrow}{N_L^\downarrow N_R^\uparrow}$$

and

$$\Delta = \left(r^2+1\right)\left(p^\uparrow - p^\downarrow\right)^2 + 2N\left[\left(p^\uparrow - p^\downarrow\right)^2 + 8p^\uparrow p^\downarrow\right].$$

In the special case where $p^\uparrow \approx p^\downarrow = p$, this reduces to the form given by Haeberli [Hae74]:

$$A_y = \frac{1}{p}\frac{\sqrt{r}-1}{\sqrt{r}+1}.$$

3.6 Error analysis

3.6.1 Statistical uncertainties

The error associated with the calculated cross section and analysing power values as shown in the data are due to the normal statistical fluctuations in the count rate in each energy bin. The number of counts in each energy bin, N, is considered to be one single measurement with a standard deviation, σ, given by $\pm\sqrt{N}$ [Kno82]. The average number of counts per energy bin for a typical two hour run was about 6 000. The associated error is therefore about 77 counts, i.e. ~1.3% per 4 MeV energy bin.

In the derivation of the absolute double differential cross section, standard statistical error propagation techniques were employed. Here the propagated error in a derived quantity $u = u(x, y, z, ...)$ is determined from [Kno89]

$$\sigma_u^2 = \left(\frac{\partial u}{\partial x}\right)^2 \sigma_x^2 + \left(\frac{\partial u}{\partial y}\right)^2 \sigma_y^2 + \left(\frac{\partial u}{\partial z}\right)^2 \sigma_z^2 + ...$$

with $\sigma_x = \sqrt{x}$ being the standard deviation of the dependant quantity x, etc. The cross section, for example, is therefore quoted as $d^2\sigma_0 \pm \sigma_{d^2\sigma_0}$.

For the double differential cross section, the associated statistical uncertainty is given by

$$\sigma_{d^2\sigma_0} = F\sqrt{N_L^{\uparrow} + N_L^{\downarrow} + N_R^{\uparrow} + N_R^{\downarrow}}\ ,$$

which is generally < 1%.

The statistical uncertainty associated with the derived analysing power is determined in a similar manner as the cross section, and is given by the expression

$$\sigma_{A_y} = \frac{4}{\left(p^{\uparrow} + p^{\downarrow}\right)}\sqrt{\frac{\left(N_L^{\uparrow} + N_R^{\downarrow}\right)\left(N_L^{\downarrow} + N_R^{\uparrow}\right)\left(N_L^{\downarrow} + N_R^{\uparrow} - N_L^{\uparrow} - N_R^{\downarrow}\right)}{\left(N_L^{\downarrow} + N_R^{\uparrow} - N_L^{\uparrow} - N_R^{\downarrow}\right)^4}}\ .$$

It is of interest to again note that the analysing power is a ratio of counts and therefore any asymmetries in the left and right detector telescopes will cancel out. By alternating the incident polarisation direction, such systematic errors are effectively eliminated.

3.6.2 Systematic errors

The dominant contributors to the overall systematic error in the calculation of the cross section are the target thickness, the measured solid angle, detector calibrations and particle identification gates. Probably the largest source of any uncertainty in the cross section calculation is the target thickness. The thicknesses of the targets, which were also used in the experiment by Bezuidenhout [Bez06], are only known to ~7%.

Errors in the solid angle subtending the collimators arise from the measurements of the detector distances and the diameter of the collimator opening. These measurements had an accuracy of < 1%, largely from the diameter of the central opening in the tantalum collimator which is 14.1 ± 0.1 mm.

The uncertainty in the energy calibration of the detectors comes primarily from the response of the NaI detectors which is less than 4%, as mentioned in section 3.1.2, and the position of the centroid of the elastic peak in the ^{12}C energy spectrum. Based on the resolution of the NaI detector, one can assign an error of roughly 1 channel, which corresponds to an error of ~0.3%.

Another contributor to the systematic error in the measurement of the cross section is the uncertainty in the angle of the detector telescopes. By far the largest part comes from the measured beam offsets which were typically less than 0.3º on either side of the incident beam direction. The overall systematic error in the detector angles is therefore estimated to be ~1%. The sensitivity of the cross section values to the width of the PID gates was evaluated and found to be negligible, provided the gates are set comfortably in the background where the count rate drops to about 0.2% of its maximum value.

The overall systematic error, of which the largest contribution is that of the target thicknesses, is estimated at ~ 8.2% determined by adding the different systematic errors in quadrature.

CHAPTER 4 THEORETICAL DESCRIPTION AND CALCULATIONS

4.1 Overview

This chapter is dedicated to the theoretical description that underlies the study of the inclusive (*p, α*) reaction. The basic mechanism is that of a direct α-cluster knock-out by the incident proton. The interaction between the incident proton and bound α-cluster is, in its simplest form, considered to be a quasi-free collision described by the impulse approximation. In the inclusive formalism all processes that can lead to the emission of an α-cluster are taken into account and contribute to the differential cross section.

In the first section of this chapter an overview of the Distorted Wave Impulse Approximation (DWIA) is given. A discussion on polarisation and the definition of the analysing power follows. The section after that deals with the computer code THREEDEE and its use for the calculation of the differential cross section and analysing power. A summary of the optical potential parameter sets used in the code is given as well as the specific target dependent input parameters. Finally a discussion is presented for the calculation of the integrated differential cross section and analysing power for the inclusive reaction.

4.2 Distorted wave impulse approximation

In the impulse approximation, the reaction is considered to be a quasi-free interaction between the incoming proton and a single, bound α-cluster, which is then knocked out of the nucleus. The remainder of the nucleons in the target only act as spectators. In this model, multiple scattering effects and excitations of the bound α-particle are not taken into account. A comparison with the experimental data can therefore point out discrepancies and limitations in the application of such a model. For a proper treatment of nuclear reactions one must take into account distortion effects of the residual nucleus on the incident and emitted particle wave functions. In this way nuclear-medium effects are therefore taken into account by using distorted waves for the incoming, bound and outgoing particles which are modified by the presence of the target and residual nuclei. The distorted waves are determined from appropriate optical potentials.

For this theoretical description, the nuclear reaction is denoted by A (*a*, *cd*) B where A and B are the target and residual nuclei respectively, *a* is the incident beam particle, and *c* and *d* are the primary and secondary particles in the exit channel. **Figure 4-1** shows a diagram for this reaction. In the impulse approximation it is assumed that particles *c* and *d* result from a two-body interaction, *b* (*a, c*) *d* between the projectile *a* and bound cluster *b*, where A = *b* + B. This is shown in **Figure 4-2**. We thus consider only the special case where *d* = *a*, and *c* = *b*.

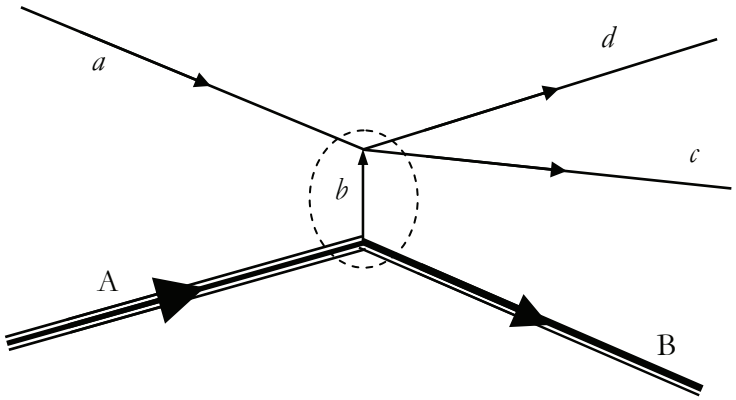

Figure 4-1: *Diagram of the direct knock-out reaction A(a, cd)B.*

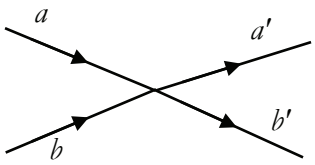

Figure 4-2: *Diagram of the quasi-free reaction between the projectile and bound cluster. The primes on the particles in the exit channel serve only to distinguish them from those in the entrance channel*

The differential cross section in the DWIA employed in the computer program THREEDEE by Chant [Cha3D], is derived from Fermi's golden rule:

$$\sigma_{fi} = \frac{2\pi}{\hbar \upsilon} \left| T_{fi} \right|^2 \omega_f \tag{4.2.1}$$

where υ is the relative velocity of *a* and A in the entrance channel and the matrix element

$$T_{fi} = \left\langle f \left| t_{fi} \right| i \right\rangle, \tag{4.2.2}$$

is the probability amplitude for scattering from initial state $\left| i \right\rangle$ to final state $\left| f \right\rangle$ and the transition operator t_{fi} is the difference between the exact Hamiltonian and the Hamiltonian

used to generate the final state. The factor ω_f is the energy density of the final states, i.e. the number of states to which transitions are possible.

The energy density, as derived by Mabiala [Mab07], is given as

$$\omega_f = \frac{\upsilon \hbar c E_a E_{a'} p_{a'} p_b}{(2\hbar c)^7 (2\pi)^5 p_a} \underbrace{\left[1 + \frac{E_b}{E_B}\left(1 - \frac{p_a}{p_b}\cos\theta_{ab} + \ldots\right)\right]}_{K_F} d\Omega_{a'} d\Omega_b dE_{a'}, \tag{4.2.3}$$

where the factor in square brackets, K_F, is a kinematic factor.

If we neglect the interacting potential in the total Hamiltonian, a *t*-operator can be defined as:

$$T_{fi} = \left\langle \Phi^{(-)}\left(\widetilde{B, a', b}\right) \middle| t_{fi} \middle| \Phi^{(+)}\left(\widetilde{A, a}\right) \right\rangle \tag{4.2.4}$$

where the ~ symbol indicates that the initial and final states are anti-symmetric with respect to the interchange of any two nucleons. The wave functions are rewritten in terms of products of separately anti-symmetrised wave functions which ignore the exchange of nucleons of the projectile *a* and the residual nucleus B.

In the impulse approximation, the *t*-operator is replaced by the two-body operator for the free *a* + *b* scattering process, t_{free}. If one assumes that the two-body *t*-matrix varies slowly with momentum, this approximation implies replacing the matrix elements with their asymptotic values.

Consequently the transition amplitude can be expressed in the factorised form as [Cha83]

$$\begin{aligned} \left|T_{fi}\right|^2 = & \sum_{\substack{\rho_a \rho'_c \rho''_d \\ JM}} \frac{1}{(2J_A + 1)(2S_a + 1)} \\ & \times \left| \sum_{\substack{\sigma_a \sigma'_c \sigma''_d \\ \Lambda \sigma_b}} (2L+1)^{\frac{1}{2}} \left(L \Lambda S_b \sigma_b \middle| JM\right) \times T^{L\Lambda}_{\substack{\rho_a \rho'_c \rho''_d \\ \sigma_a \sigma'_c \sigma''_d}} \left\langle \sigma'_c \sigma''_d \middle| t_{\text{free}} \middle| \sigma_a \sigma_b \right\rangle \right|^2 \end{aligned} \tag{4.2.5}$$

where L is the relative angular momentum of b and B (projection Λ), J_A is the angular momentum of the target, J is the angular momentum (projection M) of particle b, S_i are the spin quantum numbers with projections ρ_i and σ_i for particles i = *a, b, c, d* (as defined by Chant *et al.* [Cha83]), t_{free} is the two-body operator for the free N-N scattering process as obtained from the impulse approximation. The primes denote the relative directions of propagation of particles *a*, *c* and *d* which are defined as follows: the un-primed z-axis is along the beam direction while particles *c* and *d* propagate parallel to the z′- and z″-axes respectively [För92], [Cha83]. In this notation, the scattering plane is defined by $\hat{z}\times\hat{z}'$ as seen in **Figure 4-3**.

The amplitude $T^{L\Lambda}$ is written as

$$T^{L\Lambda}_{\substack{\sigma_a\sigma'_c\sigma''_d \\ \rho_a\rho_c\rho_d}} = (2L+1)^{-1/2}\int \chi^{(-)*}_{\sigma'_c\rho'_c}(\vec{r}')\chi^{(-)*}_{\sigma''_d\rho''_d}(\vec{r}'')\times\chi^{(+)}_{\sigma_a\rho_a}(\gamma\vec{r})\phi_{L\Lambda}(\vec{r})\,d\vec{r}\,, \tag{4.2.6}$$

and is generally known as the distorted momentum distribution, since in the plane wave limit of no distortions, it reduces to the Fourier transform of the bound state α-cluster wave function. The functions, $\chi^{(\pm)}_{ij}$, represent the distorted waves for the incoming and outgoing particles, and $\phi_{L\Lambda}$ is the bound-state wave function for particle *b*, the α-cluster in the target nucleus. The factor $\gamma = B/A$ is the ratio of the mass numbers of the residual and target nuclei. Details of the evaluation of the distorted momentum distribution can be found in references [Mab07] or [Cha77].

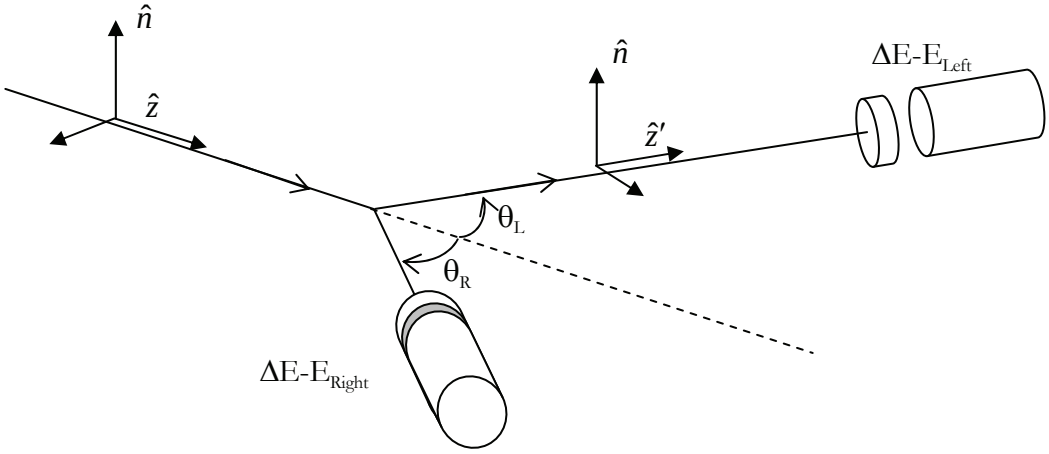

Figure 4-3: *Schematic representation of the scattering setup. The incident beam direction is in the positive z-direction.*

In the case where the two-body *t*-matrix elements are not dependent on spin, the triple differential cross section for specific values of L and J is eventually expressed by Chant *et al.* [Cha77] in the so-called factorised form as

$$\frac{d^3\sigma}{d\Omega_p d\Omega_\alpha dE_\alpha} = C^2 F_k S_{LJ}^{\alpha} \left.\frac{d\sigma}{d\Omega}\right|_{p-\alpha} \sum_{\Lambda} \left| T_{BA}^{\alpha L\Lambda} \right|^2 \tag{4.2.7}$$

where C is an isospin coupling constant, F_k is a kinematic factor and S_{LJ} is a spectroscopic factor for the final α-particle state LJ, where

$$S_{LJ} = \left| \sum_{\alpha} S_{\alpha LJ}^{1/2} \right|^2 . \tag{4.2.8}$$

In all the THREEDEE calculations, the factor $C^2 S_{LJ}$ was set equal to unity, and the cross sections normalised to the experimental data. $\left.\frac{d\sigma}{d\Omega}\right|_{p-\alpha}$ denotes the two-body p-α cross section.

From equation (4.2.7) it can be seen that the differential cross section is just proportional to the cross section for the projectile-cluster interaction and the momentum distribution of the cluster relative to the core [Wan85], and as such, contains information about the momentum distribution of the α-particle in the nucleus.

As a result of the inclusion of spin-orbit terms in the distorting optical potentials, the p-α cross section no longer appears as a multiplicative factor. In this case the individual *t*-matrix elements must be calculated in a spin representation. The triple differential cross section is then given by

$$\begin{aligned} \frac{d^3\sigma}{d\Omega_d d\Omega_c dE_c} = C^2 F_k S_{LJ}^{\alpha} \sum_{\substack{\rho_a \rho'_c \rho''_d \\ JM}} \frac{1}{(2J_A+1)(2S_a+1)} \times \Bigg| \sum_{\substack{\sigma_a \sigma'_c \sigma''_d \\ \Lambda \sigma_b}} (2L+1)^{\frac{1}{2}} \left(L\Lambda S_b \sigma_b \middle| JM\right) \\ \times D^{1/2*}_{\sigma_c \sigma'_c}(R_{ac})\, D^{1/2*}_{\sigma_d \sigma''_d}(R_{ad}) \times T^{L\Lambda}_{\substack{\rho_a \rho'_c \rho''_d \\ \sigma_a \sigma'_c \sigma''_d}} \left\langle \sigma_c \sigma_d \middle| t_{\text{free}} \middle| \sigma_a \sigma_b \right\rangle \Bigg|^2 \end{aligned} \tag{4.2.9}$$

where the $D^{1/2}_{mn}$ are rotation matrices which describe the transformation of spin projections from n to m through a rotation R_{ai} of the respective set of axes for particle i, into the reference set of axes of the beam direction.

4.3 Polarisation and analysing power

The spin-dependency of nuclear reaction mechanisms has been successfully investigated using measurements of the analysing power [Cow02], [Bon89]. Following closely the derivations of Hillhouse [Hil90], the relationship between polarisation and analysing power is briefly discussed in this section.

The polarisation of an incident beam of spin-½ particles, which is a normalised ensemble average, is defined as

$$\vec{P}^{\text{inc}} = \frac{Tr\left(\rho^{\text{inc}}\vec{\sigma}\right)}{Tr\ \rho^{\text{inc}}} \tag{4.3.1}$$

where $\vec{\sigma}$ are Pauli spin operators and ρ represents the statistical density matrix. The density matrix for the scattered beam can be written in terms of the scattering matrix M and the density matrix for the incident beam as

$$\rho^{\text{scatt}} = M\rho^{\text{inc}}M^{\dagger}.$$

One can write an expression for the differential cross section for the scattering of a beam of polarised particles into an angle θ, in terms of the density matrices as follows:

$$\sigma(\theta) = \frac{Tr\ \rho^{\text{scatt}}}{Tr\ \rho^{\text{inc}}} = \frac{Tr\left(M\rho^{\text{inc}}M^{\dagger}\right)}{Tr\ \rho^{\text{inc}}}. \tag{4.3.2}$$

For an unpolarised incident beam, the differential cross section reduces to

$$\sigma(\theta) \to \sigma_0(\theta) = \frac{1}{4}Tr\left(MM^{\dagger}\right) \tag{4.3.3}$$

The density matrix for the incident beam can be expressed in terms of the polarisation and Pauli spin matrices as

$$\rho^{\text{inc}} = \frac{1}{4}Tr(\rho^{\text{inc}})\left[1+\vec{P}^{\text{inc}}\cdot\vec{\sigma}\right]. \tag{4.3.4}$$

Substituting equation (4.3.4) for the density matrix into equation (4.3.2), the differential cross section for the scattering of polarised nucleons from an unpolarised target, is

$$\begin{aligned}\sigma(\theta) &= \frac{1}{4}Tr(MM^{\dagger}) + \frac{1}{4}\vec{P}^{\text{inc}} \cdot Tr(M\vec{\sigma}M^{\dagger}) \\ &= \sigma_0(\theta)\left[1 + \vec{P}^{\text{inc}} \cdot \vec{a}\right]\end{aligned} \tag{4.3.5}$$

where $\vec{a}$, the *asymmetry parameter*, is

$$\vec{a} = \frac{Tr\left(M\vec{\sigma}_1 M^{\dagger}\right)}{Tr\left(MM^{\dagger}\right)}. \tag{4.3.6}$$

In the case where the incident beam is polarised in the direction perpendicular to the scattering plane, i.e. the direction defined by the unit vector $\hat{n} = \hat{z} \times \hat{z}'$ as in **Figure 4-3**, equation (4.3.5) reduces to

$$\sigma(\theta) = \sigma_0(\theta)\left(1 + \vec{P}^{\text{inc}} \cdot A_y \hat{n}\right) \tag{4.3.7}$$

where A_y is referred to as the analysing power.

The meaning of the analysing power becomes clearer when one considers the scattering of the beam particles through an angle θ to the left and right with respect to the incident beam direction, see **Figure 4-3**. In the case of scattering to the left (L), the vector $\hat{n}$ points upwards, while in the case of scattering to the right (R), according to the right-hand screw rule, the vector $\hat{n}$ points downwards. One can therefore write equation (4.3.7) as

$$\begin{aligned}\sigma_L(\theta) &= \sigma_0(\theta)\left(1 + \vec{P}^{\text{inc}} \cdot A_y \hat{n}\right) \\ \sigma_R(\theta) &= \sigma_0(\theta)\left(1 - \vec{P}^{\text{inc}} \cdot A_y \hat{n}\right)\end{aligned}. \tag{4.3.8}$$

Combining these two equations for scattering to the left and right, yields

$$A_y p^{\text{inc}} \equiv \frac{\sigma_L(\theta) - \sigma_R(\theta)}{\sigma_L(\theta) + \sigma_R(\theta)} \tag{4.3.9}$$

where $p^{\text{inc}} \equiv \vec{P}^{\text{inc}} \cdot \hat{n}$ is generally referred to as the polarisation of the incident beam, and can be determined if the analysing power is known, as discussed in section 2.6.2. The term

$A_y p^{inc}$ is again just the asymmetry parameter of equation (4.3.5) and from equation (4.3.9) one can understand why it is called such.

The analysing power is one of many polarisation (spin) transfer observables, $D_{i'j}$ given by

$$D_{i'j} = \frac{Tr\left(M\sigma_j M^{\dagger}\sigma_i\right)}{Tr\left(MM^{\dagger}\right)},$$

which relates the ith component of the scattered beam polarisation to the jth component of the initial beam polarisation in terms of the scattering matrix, and specifically

$$D_{0n} = A_y = \frac{Tr\left(M\sigma_n M^{\dagger}\right)}{Tr\left(MM^{\dagger}\right)}.$$

4.4 Computer code THREEDEE

The computer program THREEDEE by Chant [Cha3D] was installed on the VAX computer network at iThemba LABS. It was decided to compile the code libraries in a Microsoft Windows environment using a free GNU FORTRAN77 compiler.

The code was used to calculate the triple differential cross sections and analysing powers for the A (*p, αp*) B reaction. The code employs the DWIA formalism of Chant *et al.* [Cha77] to calculate differential cross sections and analyzing powers for reactions of the type A (*a, cd*) B, where A = *b* + B is considered a bound state and it is assumed that particles *c* and *d* result from a two body reaction *b (a, c) d* as already discussed in section 4.2.

In the factorised form of the DWIA, the triple differential cross section for the scattering of an α-particle with orbital angular momentum *L* and total angular momentum J, is given by equation (4.2.7) [Car84], [Cha77] and [Cha83]. The radial wave functions in equation (4.2.6) are generated in the THREEDEE code by solving the Schrödinger equation with a complex optical potential and matching them to Coulomb functions at a radius where the effect of the nuclear potentials should have a negligible influence on the solution of the respective Schrödinger equations. For the bound-state wave function the solution of the overlap

integral of the many-body wave functions of the target A and residual nucleus B are negligible at this radius. This radius is expressed simply as the product of the number of steps and the integration step size used to generate the wave functions. The program performs a three-dimensional integration of equation (4.2.6) by evaluating the integrand at each Gaussian mesh point in r, θ and ϕ.

In order to calculate the double differential cross section and analysing power for the inclusive (p, α) reaction, an integration is carried out over the solid angle of the undetected particle, in this case the exiting proton. To take into account any loss of flux due to reactions where the incoming proton is absorbed or interacts with the recoil nucleus, the imaginary part of the optical potential between the ejected proton and residual nucleus is set to zero. [Cow02].

4.4.1 Standard optical potentials

The THREEDEE code uses standard optical model potentials which serve to account for inelastic scattering effects where some of the incident flux is removed from the elastic channel, very much like the absorption of light when it passes through an opaque sphere.

Optical potentials are generally obtained by analysing the appropriate elastic scattering data. In many cases similar fitting parameters are obtained for the elastic scattering by many target nuclei over a wide range of incident energies. These "global" optical potentials are very useful to calculate distorted waves for energies and targets nuclei for which no elastic scattering measurements are available.

The optical potential for the scattering-wave functions is generally written in the form

$$U(r) = U_{coul}(r_C) + (V + iW)\, f(r) + \left(\frac{V_S}{r} \vec{L} \cdot \vec{S} + iW_S \right) g(r) \qquad (4.4.1)$$

where U_{coul} is the Coulomb term, V and W are central potential strengths, V_S and W_S are spin-orbit strengths.

The form factor for the central part of the optical potential, *f(r)*, has a Woods-Saxon radial dependence given as

$$f(r, r_i, a_i) = \frac{1}{1 + \exp\left(\frac{r - r_i A^{1/3}}{a_i}\right)}.$$

The form factor, *g(r)*, is taken as the radial derivative of *f(r)* since it has been found that the spin-orbit force vanishes in the interior region of the nucleus [Mar70]. In all these Woods-Saxon potential forms, a_i is a diffuseness parameter, i.e. the radial distance over which the central potential decreases to zero, and $r_i A^{1/3}$ represents the radius at which the potential strength drops to half its central value, generally referred to as the mean radius.

The Coulomb term is determined from the potential due to a uniformly charged sphere of radius $R_C A^{1/3}$, and is calculated from

$$U_{coul}(r) = \begin{cases} \dfrac{Z_p Z_t e^2}{2R_C A^{1/3}}\left(3 - \dfrac{r^2}{(R_C A^{1/3})^2}\right), & \ldots\ldots r < R_C A^{1/3} \\ \dfrac{Z_p Z_t e^2}{r}, & \ldots\ldots r \geq R_C A^{1/3} \end{cases}$$

where $Z_p e$ and $Z_t e$ represent the charge of the projectile and target.

In the program THREEDEE the central part of the optical potential for the scattering-wave functions is expressed in the form

$$U_{central}(r) = U_{coul}(r_C) - \left[\frac{V}{1+e^x} + \frac{iW}{1+e^{x'}} + \frac{4iW_D e^{x'}}{(1+e^{x'})^2}\right] \qquad (4.4.2)$$

where $x = \dfrac{r - R_0 A^{1/3}}{a_0}$ and $x' = \dfrac{r - R_0' A^{1/3}}{a_0'}$.

In addition to the central term above, spin-orbit and exchange terms may be added, specifically

$$U(r) = U_{central}(r) - \left[g\vec{l} \cdot \vec{\sigma} \frac{\left(V_s + iW_S e^{x_s}\right)}{r a_s \left(1 + e^{x_s}\right)^2} + (-1)^l \frac{V_{ex}}{1 + e^{x_{ex}}} \right] \tag{4.4.3}$$

with $x_s = \dfrac{r - R_s A^{1/3}}{a_s}$ and $x_{es} = \dfrac{r - R_{es} A^{1/3}}{a_{es}}$.

The potential for the bound state of the α-particle is given by

$$U(r) = U_{coul}(R_C) - \frac{V}{1 + e^x} - g\vec{l} \cdot \vec{\sigma} \left[\frac{V_s e^{x_s}}{r a_s \left(1 + e^{x_s}\right)^2} \right] \tag{4.4.4}$$

where $x_s = \dfrac{r - R_s A_B^{1/3}}{a_s}$.

4.4.2 Potential parameter sets

A list of global mass- and/or energy-dependent potentials are available in the subroutine POTSET. These parameters options can be selected in the input file.

The distorted waves for the interaction of the proton in the entrance channel with the target nucleus A, and the interaction of the proton in the exit channel with the residual nucleus B, were generated using the energy-dependant optical potential set of Nadasen *et al.* [Nad81]. **Table 4-1** gives the parameters as they appear in the THREEDEE code. The symbol A is the mass number of the target nucleus, Z its atomic number, and E_p the effective projectile energy. These Nadasen potentials have been developed from differential cross section measurements of elastic proton-nucleus interactions on targets such as ^{40}Ca, ^{90}Zr and ^{208}Pb, and for a proton energy range of between 80 and 180 MeV.

The choice of potential parameters for the bound state of the α-cluster is not straight forward. Following the arguments of Carey *et al.* [Car84], the wave function of the α-cluster is a complicated overlap integral between the target ground state and the internal wave function of the residual nucleus. Contained in this overlap is not only the ground state of the α-particle, but also possible excited states with different centre-of-mass motions. It is generally assumed that the ground state configuration of ^{4}He is the dominant term in the

reaction. According to Carey *et al.* this approximation is valid especially in the case of the highly surface-localised (*p, αp*) reaction.

Common practice is to use an eigenfunction of a Woods-Saxon potential with an eigenvalue corresponding to the separation energy of the α-cluster. The potential parameters for the bound α-particle are then often determined by folding an α-nucleon interaction into charge distributions obtained from electron scattering [Roo77], [Car84]. This has the physical significance of relating the potential well geometry to different target nuclei. For the purpose of this thesis, we have selected the potential parameters for the heavier ^{66}Zr target, given by Carey *et al.* [Car84], for the bound cluster state as well as the interaction between the outgoing α-particle and residual nucleus. (see **Table 4-1**)

	p + A / p + B (Nadasen *et al.*)	α + B / bound state (Carey *et al.*)	p + ^{4}He (Van Oers *et al.*)
V	ξ[117.5 - 14.34 ln(Ep) - 50(Z/A)]	161.77	27.35 - 5.046 ln(Ep)
W	7.4 ξ	14.80	6.55 + 0.06977 Ep - 6.25e-05 $(Ep)^2$ + 2.3215e-08 $(Ep)^3$
R_0	1.21	1.26	1.577
R'_0	1.37 + 3.5/A	1.61	1.493
a_0	0.77	0.752	0.200
a'_0	0.36 + 0.036 $A^{1/3}$	0.580	0.315
W_D	0.0	0.0	0.0
R_C	1.25	1.30	1.36
V_S	ξ[15.0 – 2.4 ln(Ep)]	0.0	25.37 - 3.243 ln(Ep)
W_S	-1.2 ξ	0.0	5.69 - 1.355 ln(Ep)
R_S	0.985 + 0.0002 A + 0.00064 Ep	1.0	0.879
a_S	0.52 + 0.00086 A	1.0	0.303

Table 4-1: *Optical potential parameters used in THREEDEE given by the authors in brackets. The ξ-factor in the Nadasen set is a conversion factor used to convert potential strengths from the IUCF conventions to the definitions used in the present THREEDEE code. All potential strengths are in MeV and length parameters in fm.*

The interaction of the proton with the bound α-cluster is determined from energy dependent p + ^{4}He potentials given by Van Oers *et al.* [Van82], also listed in **Table 4-1**. These potential

parameters were obtained from experimental elastic ^{4}He(p, p)^{4}He cross sections and analysing powers for different incident energies.

The choice of optical potentials used in this study is based on the generally accepted potentials used in many knock-out reaction studies giving quite satisfactory agreement with experimental data [Cow96], [Nad89], [Wan85], [Yos98]. As noted by Neveling *et al.* [Nev07] in (p, $2p$) reaction studies, the theoretical cross section and analysing power calculations are rather insensitive to the details of the distorting potentials. Even without these distortions, as in the case of plane wave calculations, very similar results were found. This observation is confirmed by Arendse [Are97] who tested the sensitivity of the (p, $2p$) knock-out calculations to different optical potentials. Carey *et al.* [Car84] noted that the primary effect of the different potential parameters is on the magnitude of the cross section. As this study is mostly concerned with the qualitative description of the data, it was not deemed necessary to investigate the results based on different potential choices.

The principle quantum number N, and orbital angular momentum quantum number L for the bound α-particle required by THREEDEE are determined from the conservation of single particle shell model quanta with a harmonic oscillator potential as follows [Car84]:

$$\Lambda_{\text{cluster}} = \sum_{i=1}^{4} \lambda_i \ .$$

Thus,

$$2(N-1) + L = \sum_{i=1}^{4} \lambda_i = 2(n_i - 1) + l_i \tag{4.4.5}$$

where n_i = 1, 2, 3,... and l_i = 0, 1, 2,... are the principle and orbital angular momentum quantum numbers for the last four nucleons forming the α-cluster. The harmonic oscillator shell model energy levels are given by

$$E_{HO} = \hbar\omega\left(\lambda + \frac{3}{2}\right) - c'\begin{cases} l & \text{for } j = l - \frac{1}{2} \\ -(l+1) & \text{for } j = l + \frac{1}{2} \end{cases} \qquad \text{for } \lambda = 0,1,2,3,... \tag{4.4.6}$$

The possible orbital angular momentum quantum numbers, L , of the α-cluster are those satisfying the relation,

$$\Lambda = 2(N-1) + L \tag{4.4.7}$$

for N = 1, 2, 3,... and L = 0, 1, 2,....

The different possible quantum numbers of the bound α-particle in ^{93}Nb and ^{59}Co are listed in **Table 4-2**. All of the inclusive calculations in this study on ^{59}Co and ^{93}Nb were concerned with only the ground state transition.

Target	*Proton states*	*Neutron states*	Λ	N	L
^{93}Nb	$2p\,1/2$	$1g\,7/2$	15	7	3 (F)
	$1g\,9/2$			8	1 (P)
^{59}Co	$1f\,7/2$	$2p\,3/2$	12	7	0 (S)
				6	2 (D)

Table 4-2: *Principle and orbital angular momentum quantum numbers of the bound state of the α-cluster in the two target nuclei.*

4.5 Inclusive calculations

4.5.1 Double differential cross section

As only inclusive (p, α) reactions were investigated, integration over the solid angle of the undetected, secondary proton is carried out. The double differential cross section is therefore obtained from the following integral:

$$\frac{d^2\sigma}{d\Omega_\alpha dE_\alpha} = \int_{\Omega_{p'}} \frac{d^3\sigma}{d\Omega_{p'} d\Omega_\alpha dE_\alpha}\, d\Omega_{p'}\,. \tag{4.5.1}$$

Although the THREEDEE code is supposed to do the integration, it was not clear at the time where the code gives this integral value. So instead, a separate FORTRAN code called INTEGRATE was written which uses the triple differential cross sections and analysing powers for the coincidence (p, αp) reaction, calculated with THREEDEE, to do a numerical Gauss-Legendre integration. As described in the THREEDEE code, the integration is based on an N-point Gauss-Legendre quadrature method. The zeros of the Legendre polynomial of order N and their associated weights needed in the INTEGRATE code were calculated with THREEDEE in the subroutine LGAUSS. The numerical integration is discussed in more detail in the appendix. The integration range used in this study was generally chosen as

$5° \leq \theta_{p'} \leq 355°$ and similarly for the out-of-plane angle $5° \leq \beta_{p'} \leq 355°$ using 5 Gauss points in both cases.

4.5.2 Analysing power

The analysing power for the inclusive (*p*, α) reaction, when detecting the α-particle at an angle θ_α to the left (or right) of the incident beam direction, is calculated from equation (7.3.3) derived in the appendix:

$$A_\alpha(\theta_\alpha) = \frac{\int A_{(p,\alpha p)}(\theta_\alpha, \theta_p) \frac{d^3\sigma(\theta_\alpha, \theta_p)}{d\Omega_p d\Omega_\alpha dE_\alpha} d\Omega_p}{\int \frac{d^3\sigma(\theta_\alpha, \theta_p)}{d\Omega_p d\Omega_\alpha dE_\alpha} d\Omega_p}, \tag{4.5.2}$$

where $\frac{d^3\sigma(\theta_\alpha, \theta_p)}{d\Omega_p d\Omega_\alpha dE_\alpha}$ is the absolute triple differential cross section and $A_{(p,\alpha p)}(\theta_\alpha, \theta_p)$, the analysing power for the coincidence (*p*, αp) reaction. The integration is again performed over the solid angle of the undetected proton, which is done with the code INTEGRATE.

CHAPTER 5 RESULTS AND DISCUSSIONS

This chapter presents the results of the measurements on ^{93}Nb (p,α) at 160 MeV incident energy. The complete set of measured double differential cross section and analysing power values are listed in appendix a and b. Theoretical DWIA calculations done with the code THREEDEE by Chant [Cha3D], as discussed in the previous chapter, are compared with the present experimental data as well as data from Cowley *et al.* [Cow02] for the ^{59}Co (p,α) and ^{93}Nb (p,α) reactions at 100 MeV incident energy, and data analysed by Bezuidenhout [Bez06] for the reaction ^{59}Co (p,α) at 160 MeV.

The first part of this chapter, section 5.1, briefly discusses several initial test calculations which were performed with the THREEDEE code for the coincidence ($p, p\alpha$) reaction on targets like ^{9}Be, ^{12}C and ^{40}Ca at incident energies of 100 and 150 MeV. These calculations were done as a check to determine if similar calculations of other authors could be reproduced.

Section 5.2 gives graphical representations of the data together with the theoretical predictions for both the double differential cross sections and analysing powers as a function of scattering angle. Some comparisons are made between the two targets, ^{93}Nb (p, α) from the present study, and ^{59}Co (p, α) from the references, [Cow02] and [Bez06].

5.1 Initial (p, pα) and (p, α p) coincidence calculations with THREEDEE

Preliminary calculations done with the THREEDEE code indicated that the DWIA model could not represent the experimental data. To make sure that the code was functioning correctly a few calculations were performed as a consistency check. The results of three different cases are presented in sections 5.1.1 to 5.1.3 and in each the optical potential parameters used in the calculations are those given in the respective references.

Besides some quantitative differences between the current THREEDEE calculations and those done by the referenced authors, the overall agreement suggests that the current

THREEDEE code, at least in terms of the three-body coincidence reactions, performs satisfactorily.

5.1.1 ^{9}Be (p, pα) ^{5}He at 150 MeV

Following the study by Wang et al. [Wan85], the triple differential cross section and analysing power for cluster knock-out reaction on ^{9}Be at an incident energy of 150 MeV were calculated. The set of plots in **Figure 5-1** depicts the cross section and analysing power as a function of the relative centre-of-mass angle for a range of different quasi-free angle pairs, i.e. where the recoil momentum is zero. The calculated cross section values were normalised to fit the data given in the reference [Wan85].

In **Figure 5-2**, the results for the cross section and analysing power calculations are presented as a function of the energy of the outgoing proton for both the 3S and 2D cluster states at the quasi-free angle pair of $\theta_p / \theta_\alpha = 70° / -46.9°$. The spectroscopic factors for the two cluster states were set equal to unity for convenience. As can be seen in the graphs, the present calculations give generally similar results, at least with respect to the overall shape of the distributions.

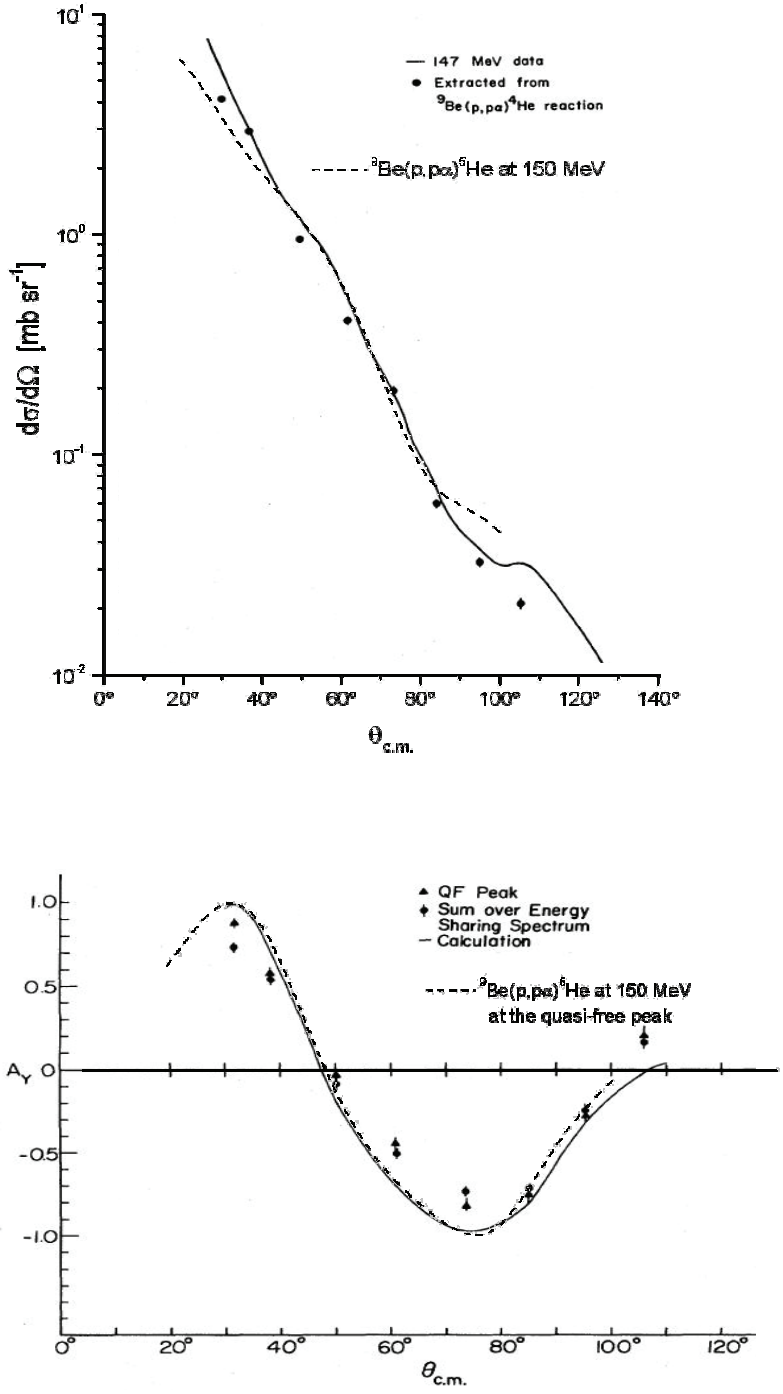

Figure 5-1: *Cross section (top) and analysing power calculations (bottom) for the ^{9}Be(p, pα) reaction at the quasi-free peak as a function of the two-body centre-of-mass angle. The dashed curves are those of the current calculations for the 3S state and the solid curves those reported by Wang et al. [Wan85] for the same reaction. The dots on the graphs are experimental data as discussed in the reference.*

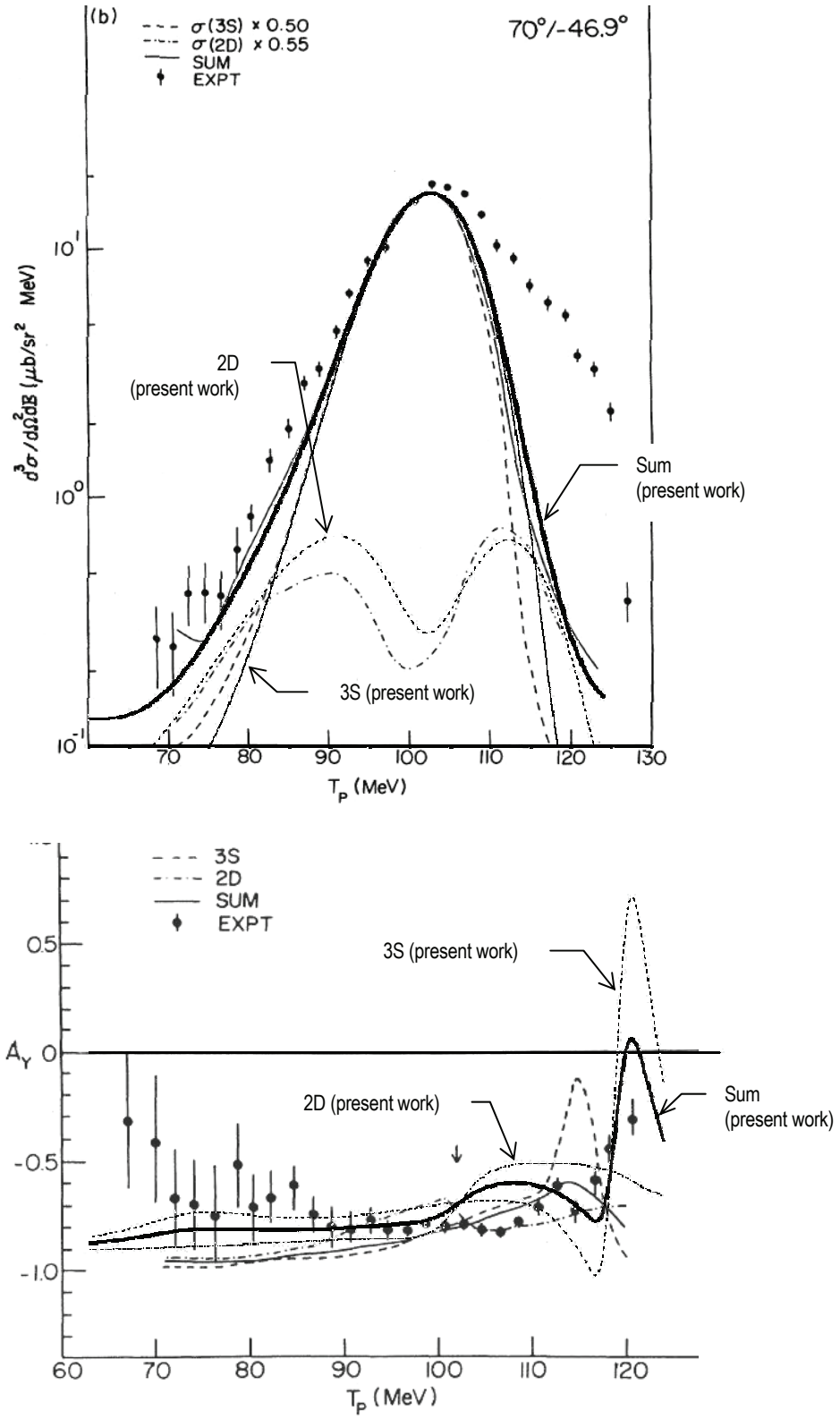

Figure 5-2: *Cross section (top) and analysing power calculations (bottom) for the ^{9}Be(p, pα) reaction at the angle pair θ_p/θ_α = 70°/-46.9° . The curves for the 2D, 3S and summed states of the present study are overlaid on those by Wang et al. [Wan85] for the same reaction as indicated. The dots in the plots are experimental data as given in the reference. The different states in the publication are indicated on the graphs.*

5.1.2 ^{12}C (p, pα) ^{8}Be at 100 MeV

As in the previous section, differential cross section distributions were calculated in order to reproduce the work done by Roos *et al.* [Roo77]. The triple differential cross sections for the 3S state of the (*p, pα*) reaction on ^{12}C at an incident energy of 100 MeV was calculated in the distorted wave and plane wave impulse approximation models. The results for the cross section at the quasi-free angle pair $\theta_p / \theta_\alpha = 90° / -35.7°$ using the DWIA (solid curves) and PWIA (dashed curves) are given below. See the caption for details.

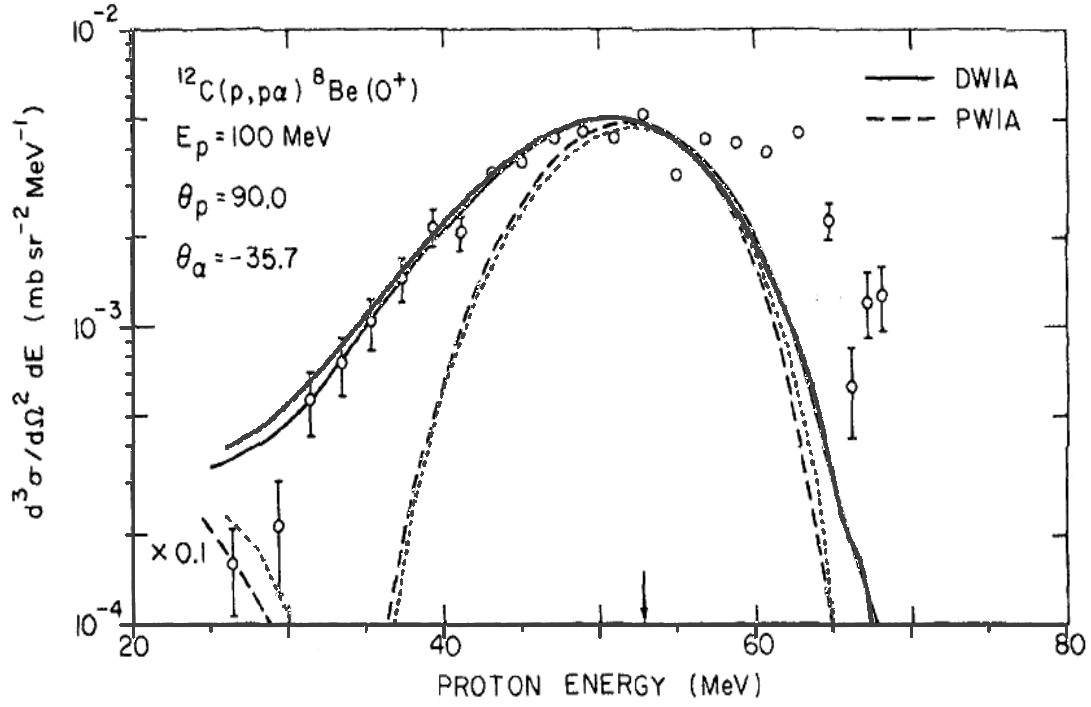

Figure 5-3: *Cross section calculations with THREEDEE compared to the results taken from Roos et al. [Roo77] for the same reaction. The uppermost solid and short dashed curves are those of the current calculations for the 3S state in the DWIA and PWIA respectively. The open circles in the plot are experimental data.*

5.1.3 $^{40}Ca\ (p, p\alpha)\ ^{36}Ar$ at 100 MeV

Lastly, the energy distributions of the differential cross section studied by Carey *et al.* [Car84] were reproduced for the 3S state of the $^{40}Ca(p, p\alpha)^{36}Ar$ reaction at an incident energy of 100 MeV, and for the quasi-free angle pair of $\theta_p / \theta_\alpha = 70° / -45.7°$. The spectroscopic amplitude was set to unity.

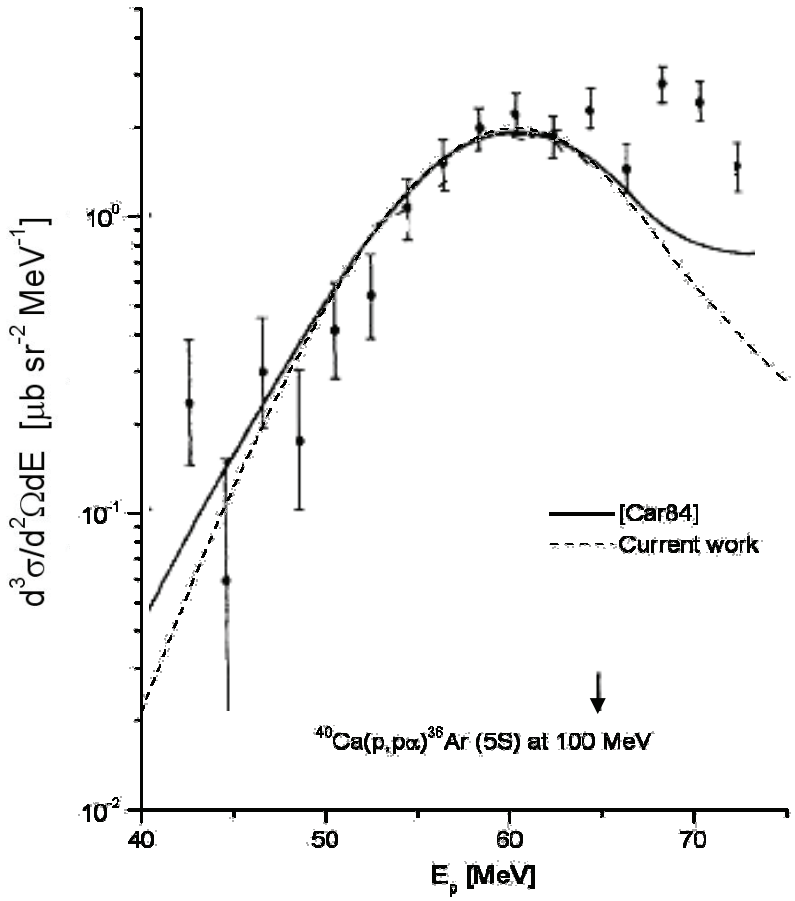

Figure 5-4: *Cross section calculations for the 3S state (dashed line) compared to calculations done by Carey et al.[Car84] for the same reaction. The dots in the plot are experimental data as given in the reference. The arrow indicates the corresponding quasi-free point (E_p = 64.3 MeV).*

5.1.4 Reaction kinematics

Initial THREEDEE calculations for the triple differential cross section of the coincidence ^{93}Nb (*p, αp*) reaction at 160 MeV were made around the quasi-free kinematic point, i.e. the kinematic conditions where the momentum of the recoil nucleus approaches a minimum and the reaction behaves like the knock-out of an α-particle at rest in the target. The kinematics of the two-body interaction was determined from calculations done with the code KINMAT in which the Q-value for the reaction was set equal to the binding energy of the α-cluster in that particular nucleus. These quasi-free angle pairs and kinetic energy values are listed in **Table 5-1**.

$\theta_{\alpha'}$[deg]	$\theta_{p'}$[deg]	$E_{\alpha'}$[MeV]	$E_{p'}$[MeV]
15	139.4	97.9	60.2
20	126.7	92.5	65.6
25	115.0	85.9	72.1
30	103.8	78.3	79.8
35	93.2	69.9	88.2
40	83.1	61.0	97.1
50	64.4	42.6	115.5
60	46.9	25.4	132.7

Table 5-1: *Kinematics for the (p, pα) reaction for zero recoil momentum. The Q-value for the reaction was set equal to -1.931 MeV, i.e. the binding energy for the α-cluster in ^{93}Nb.*

It should be expected that the impulse approximation calculations will yield cross section distributions which reflect a direct knock-out process favouring high emission energies. As seen from statistical multi-step studies done by Cowley *et al.* [Cow96], the single-step reaction dominates at forward scattering angles ($\theta_{\alpha'} < 50^{\circ}$) and large emission energies (excitation energy ~20-30 MeV).

To understand the behaviour of the DWIA results, a few calculations were performed for the ^{93}Nb (*p, αp*) reaction at 160 MeV around the quasi-free angle pair $\theta_\alpha / \theta_p = 15^{\circ} / -139.4^{\circ}$ as shown in **Figure 5-5**. A second set of ^{93}Nb (*p, αp*) cross section calculations was made for a fixed α-particle angle of 30º while integrating over a proton angle window of 40º. A schematic representation of the scattering geometry is presented in **Figure 5-6**. The results of the calculation are plotted in **Figure 5-7** for the indicated proton angles. It is instructive to

note how the cross section peaks near the quasi-free point, where $\theta_p \sim 104^o$ and $E_p \sim 78$ MeV. In all these calculations the out-of-plane angle above the scattering plane β_p was set to zero to simplify the calculations.

From these three-body calculations one can get an indication of the contribution of the different proton angles to the integrated cross section. It can be seen from **Figure 5-7** that the integrated differential cross section is dominated at small α-emission angles and large emission energies by very forward proton angles. Calculations done with the three-body kinematics code QUASTA-92 indicates that this kinematic range corresponds to the maximum recoil energy of the residual nucleus and the minimum relative energy of the outgoing α and proton.

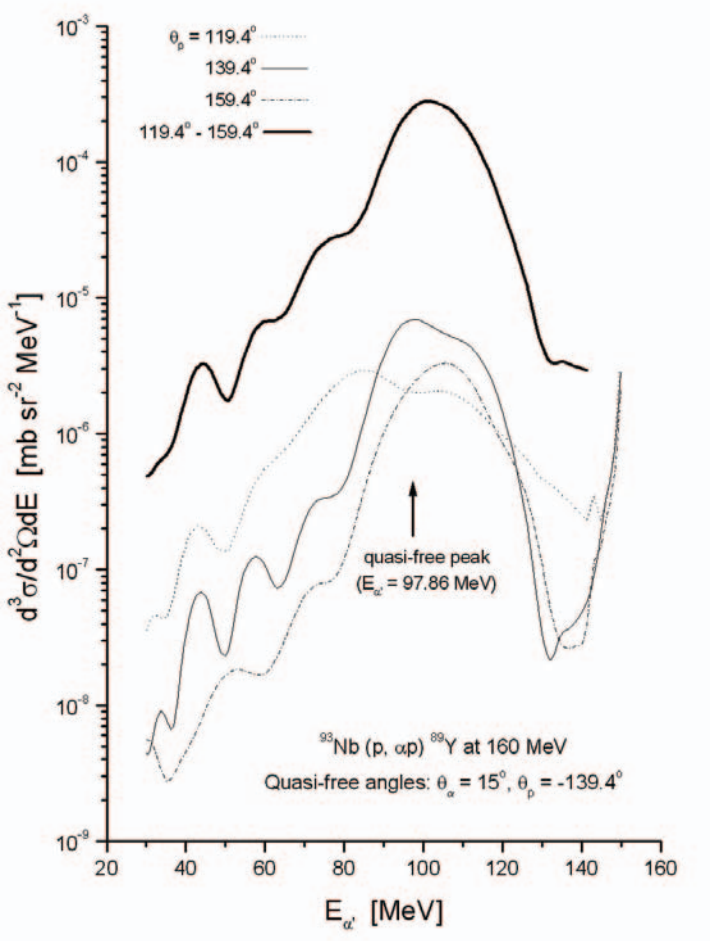

Figure 5-5: *THREEDEE calculations for ^{93}Nb (p, αp) at 160 MeV at and around the quasi-free angle pair indicated on the graph. The thick solid line represents the integral cross section for a window of 20° on either side of the quasi-free proton angle.*

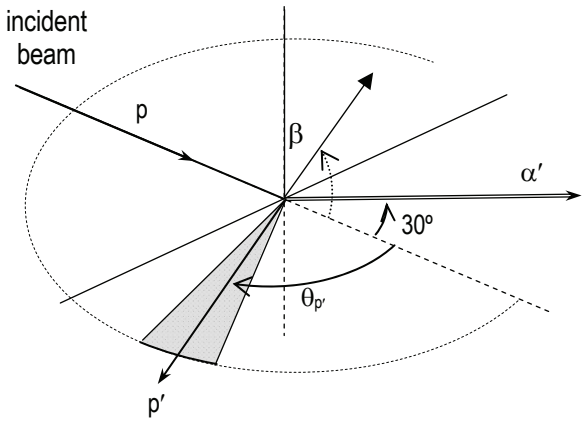

Figure 5-6: *Schematic representation of the cross section calculation. The cross section is integrated over a 40° window at different proton angles and a fixed α-angle.*

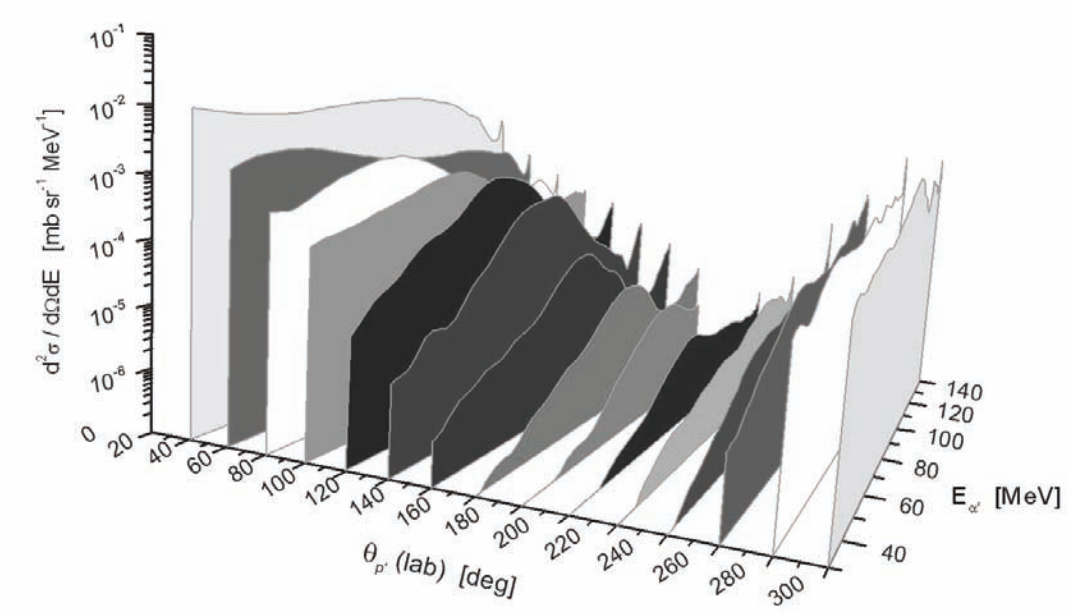

Figure 5-7: *Cross section vs. energy distributions for the ^{93}Nb (p, αp) reaction at 160 MeV and fixed α-angle of 30°. For each of the plots the proton angle is integrated over a 40° window.*

5.2 Inclusive (p, α) measurements

5.2.1 Experimental data

The double differential cross sections for ^{93}Nb (*p, α*) at 160 MeV as a function of the emission angle of the α-particle are presented in **Figure 5-8** (on the right) for several emission energies. The data are compared to that of ^{93}Nb (*p, α*) at 100 MeV incident energy (on the left). The general trend in the 160 MeV data is similar to that observed in similar studies on different targets and incident energies [Bez06], [Cow96], [Cow02]. The cross sections, for a given excitation energy, tend to be more forwardly peaked at the lower incident energy and become less forwardly peaked as the excitation energy increases. Bezuidenhout [Bez06] showed the same results for his (*p*, ^{3}He) studies and indicated that the contribution of the multi-step reaction was dominant at the larger excitation energies.

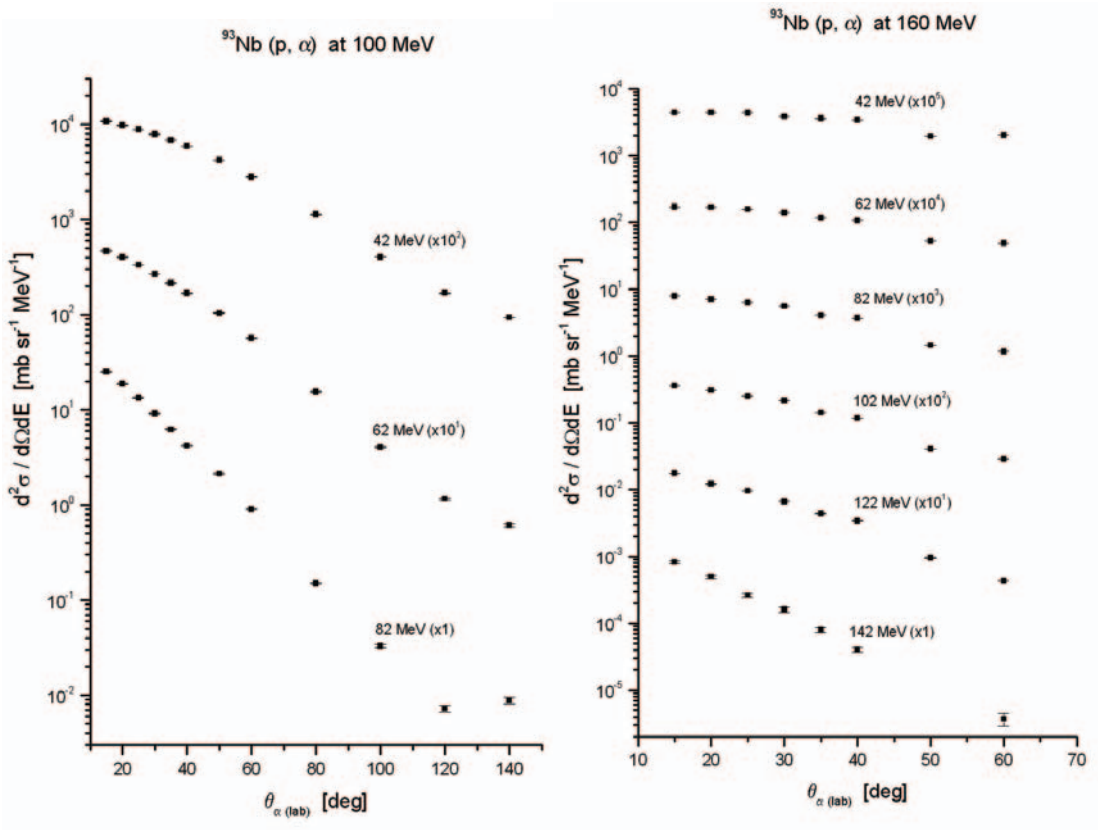

Figure 5-8: *Double differential cross section angular distributions for the reaction ^{93}Nb (p, α) at 100 MeV incident proton energy on the left and 160 MeV on the right for different outgoing α-energies as shown. The data are scaled with the factors shown in brackets to make it more distinguishable.*

The double differential cross sections for the reaction ^{59}Co (p, α) and ^{93}Nb (p, α) at 100 MeV incident energy are compared in **Figure 5-9** to show the dependency of cross section on different target nuclei. The magnitude of the cross section for the heavier target, ^{93}Nb, is slightly larger than that of ^{59}Co. This is the general trend also observed in other studies [Lew82], [Bez06] and [Cow96], and can be expected in terms of the basic idea of a reaction cross section.

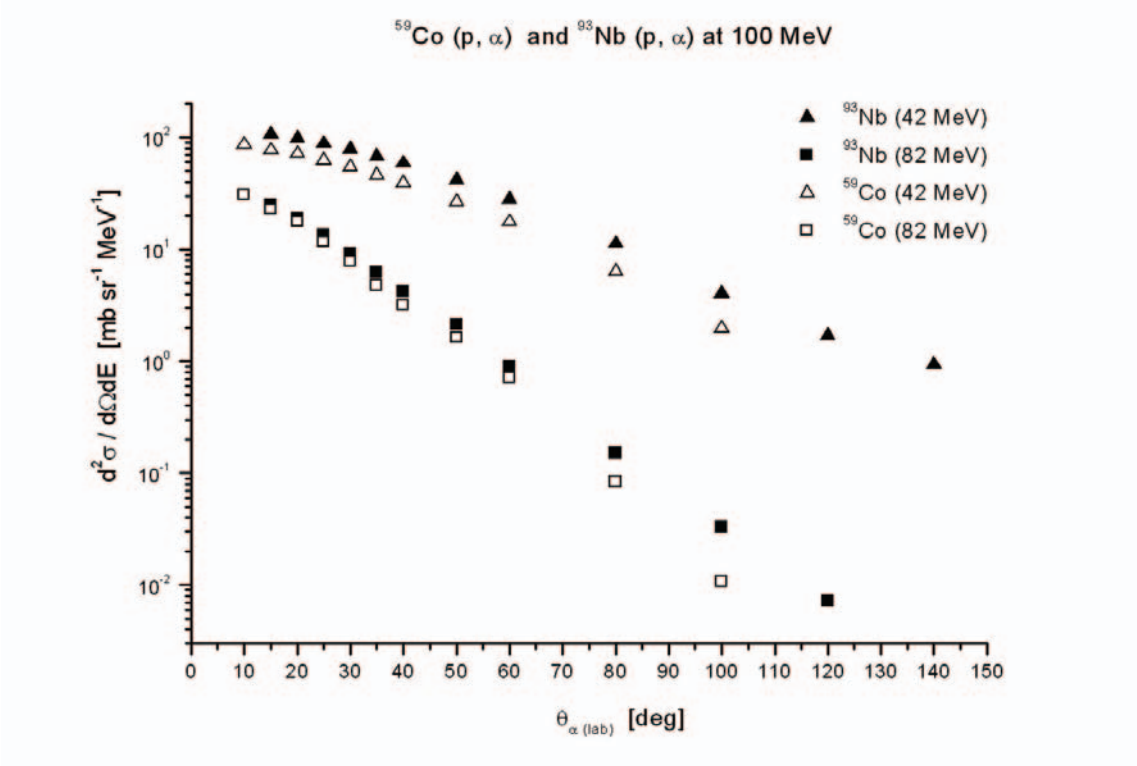

Figure 5-9: *Double differential cross section angular distributions for ^{59}Co(p, α) and ^{93}Nb (p, α) at 100 MeV incident energy and emission energies as indicated.*

The analysing power angular distributions for ^{93}Nb (p, α) at 160 MeV are given in **Figure 5-10**. The analysing power distributions seem to follow the general trend also seen in the data of ^{59}Co, [Bez06]. It was found that the analysing power is a strong indicator of the relative contributions from the various steps, and can be used to shed light on the still unclear reaction mechanism responsible for multi-nucleon cluster emissions. As expected from a single-step direct reaction mechanism, the analysing power drops off to zero at larger scattering angles. Previous multi-step studies on ^{93}Nb (p, ^{3}He), [Cow00], show a lesser contribution of the first step to the analysing power as the emission energy decreases. This

has also been observed in all the angular distributions where the DWIA predictions seem to improve with increasing emission energy (see **Figure 5-17**).

The analysing power as a function of emission energy for the measured data on ^{93}Nb at 160 MeV is shown in **Figure 5-11** for the different scattering angles. It would appear that the absolute magnitude of the analysing power decreases with increasing angle. This is understood to be associated with the direct reaction mechanism. It is suggested by the multi-step theory that the spin characteristics of the ejected particles would be averaged out after successive collisions.

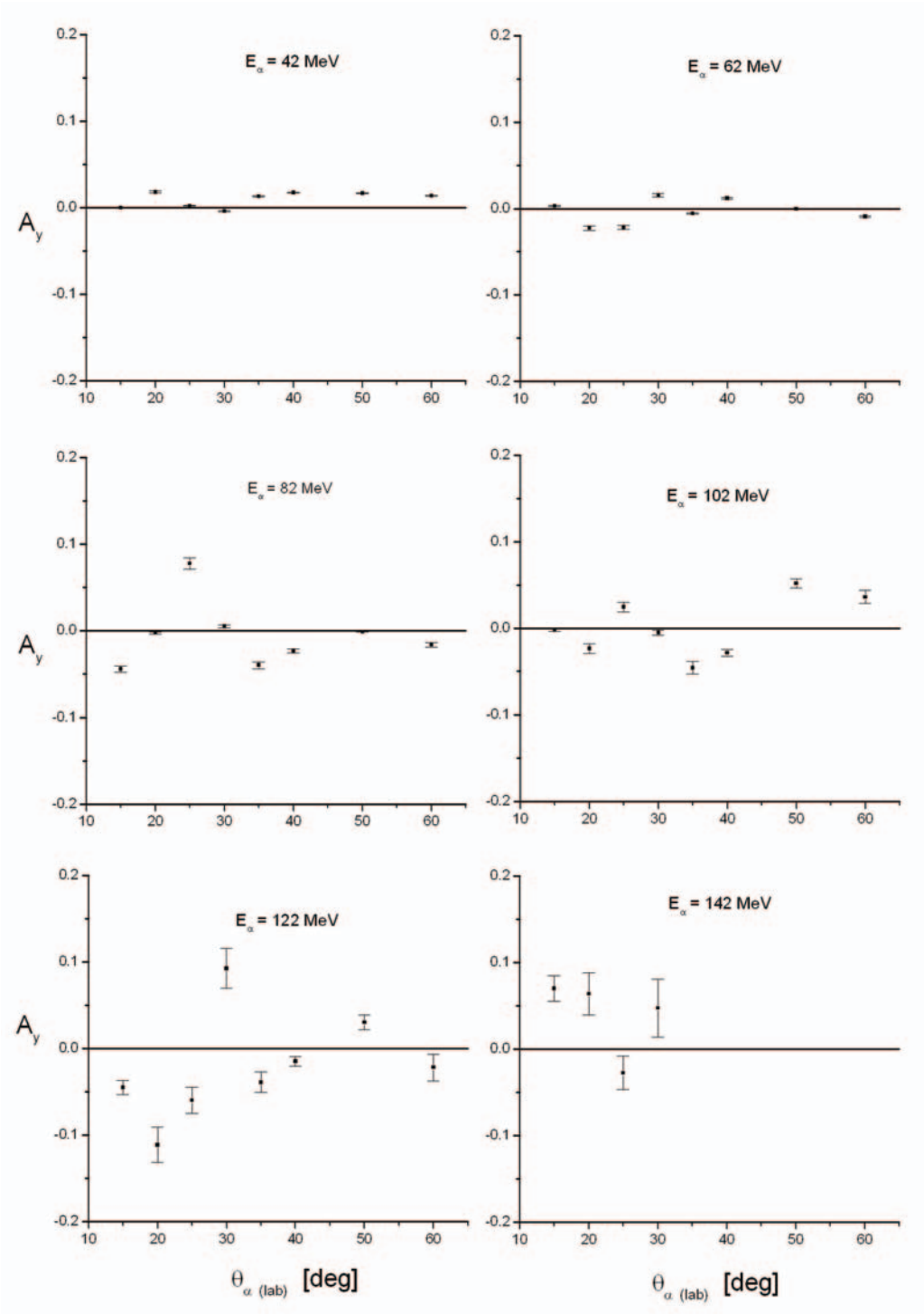

Figure 5-10: *Measured analysing power as a function of scattering angle for the reaction ^{93}Nb (p, α) at 160 MeV. The different outgoing α-energies are indicated.*

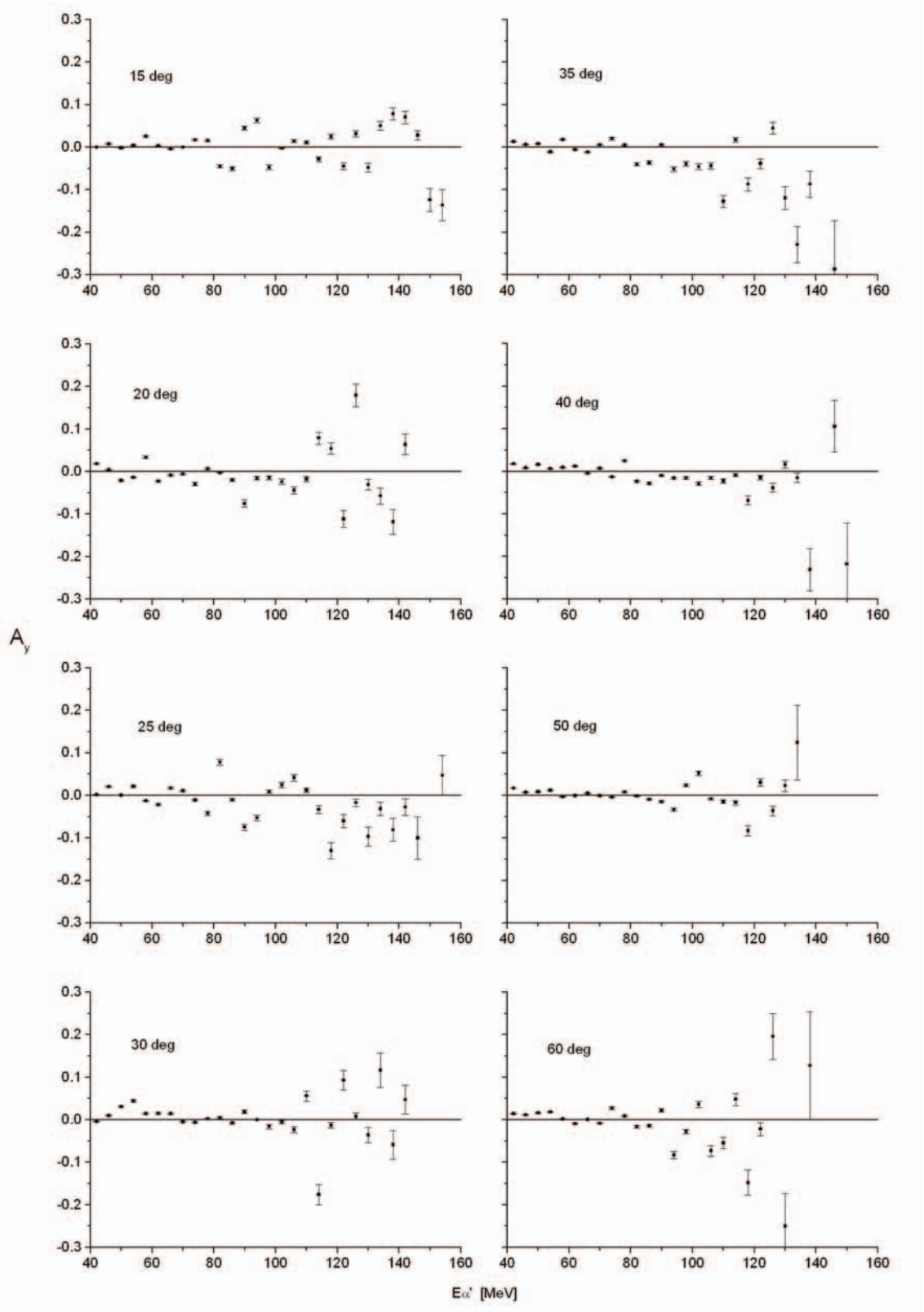

Figure 5-11: *Analysing power for the reaction ^{93}Nb (p, α) at 160 MeV incident proton energy as function of outgoing α-energy for the different α-emission angles shown. The theoretical predictions are left out in order to see the experimental data more clearly.*

5.2.2 Comparison with theory

Several theoretical calculations for the angular distributions of the double differential cross section and analysing power have been made and these are presented in **Figure 5-12** and **Figure 5-13** for ^{59}Co at 100 and 160 MeV respectively, and in **Figure 5-14** and **Figure 5-15** for ^{93}Nb at 100 and 160 MeV respectively, for a selection of α-particle emission energies as indicated.

It has been found in pre-equilibrium multi-step reaction studies done by Cowley *et al.* [Cow96], [Cow02], that the first-step α-particle knock-out process dominates the angular distributions at the higher α-emission energies, corresponding to an energy transfer of ~30 MeV or less, and very forward angles, less than ~50º. It would then be reasonable to assume that the DWIA would be more likely to represent the experimental data in this region. With this in mind, the theoretical cross sections were normalised to the experimental data at the lower α-particle angle and higher emission energy region as best as possible. This is also necessary since the absolute magnitude of the cross section depends on an unknown pre-formation factor, which represents the probability of finding a pre-formed α-cluster in the target nucleus.

Although the theoretical calculations do not reproduce the experimental trends well at all, the cross section calculations do however show the feature of a rapid decrease at the very forward angles. This is in agreement with the assumption that a direct knock-out mechanism would be forwardly peaked. As discussed by Bezuidenhout [Bez06], the forward peaked cross section agrees with the suggestion of a dominance in the contribution of the single-step direct mechanism especially at low excitation energies.

For most of the analysing power angular distributions there seem to be very little, if any correlation between the theoretical calculations and the data. The most promising predictions are at the lower incident energies of ^{59}Co and ^{93}Nb at around 82 MeV emission energy. As noted by Cowley *et al.* [Cow02] and also observed in the present calculations, direct mechanisms are generally associated with large analysing power values which have been observed experimentally at lower incident energies. A few analysing power calculations

were made around the emission energy of 82 MeV to get an indication of the sensitivity of the calculation for smaller energy increments. This is briefly discussed in appendix c.

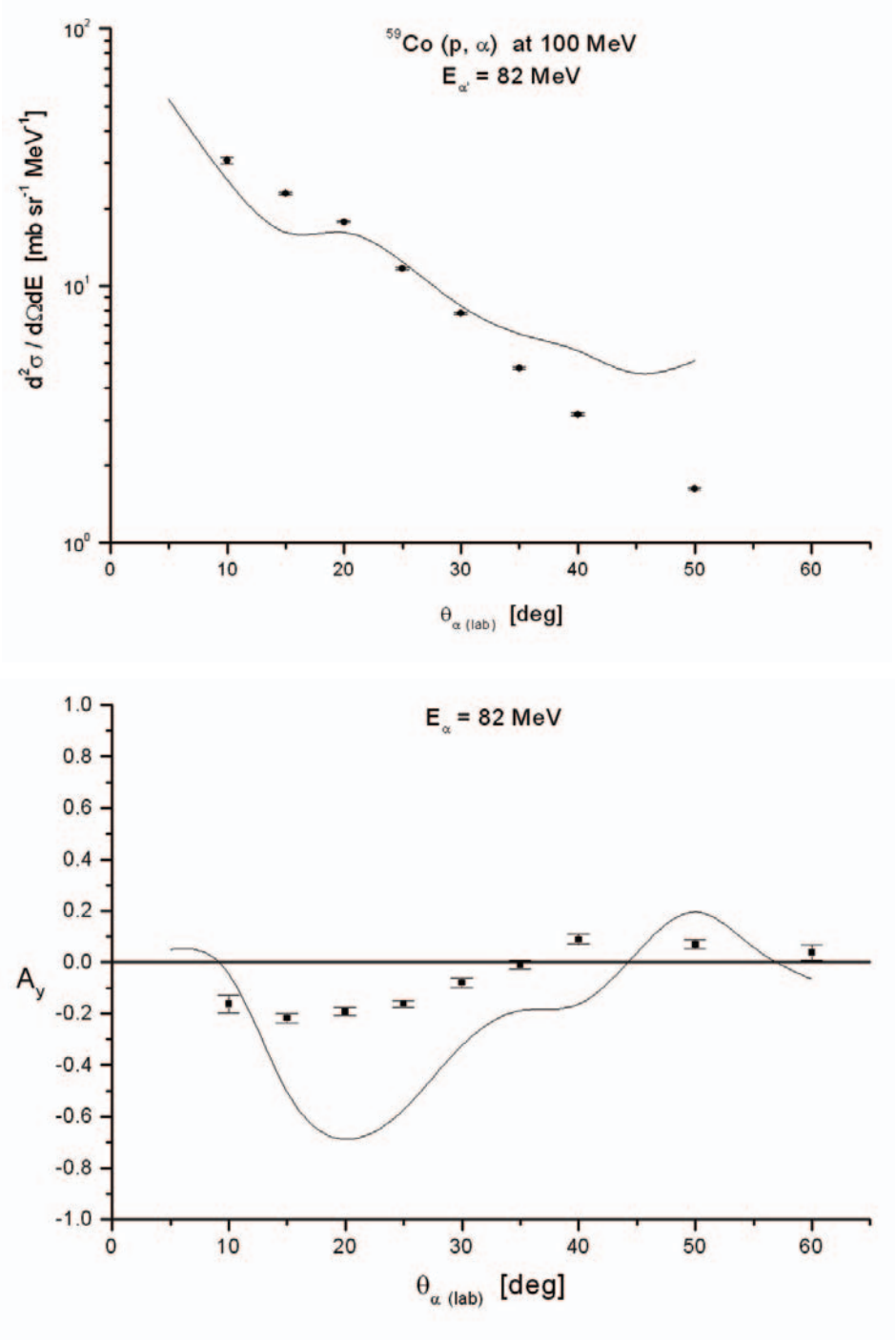

Figure 5-12: *Double differential cross section (top) and analysing power angular distributions (bottom) for the reaction ^{59}Co (p, α) at 100 MeV incident proton energy for an outgoing α-energy of 82 MeV.*

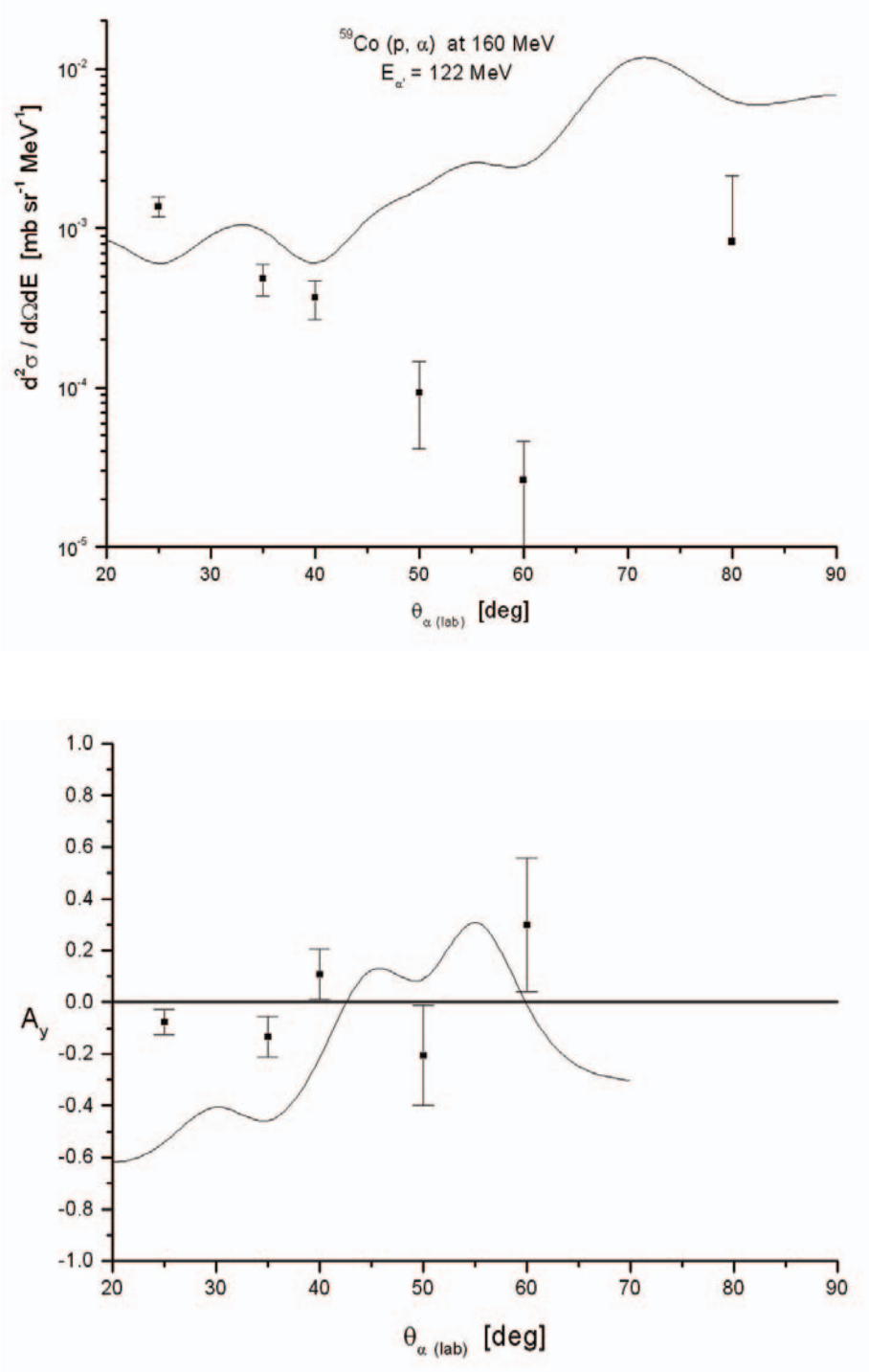

Figure 5-13: *Double differential cross section (top) and analysing power angular distributions (bottom) for the reaction ^{59}Co (p, α) at 160 MeV incident proton energy for an outgoing α-energy of 122 MeV.*

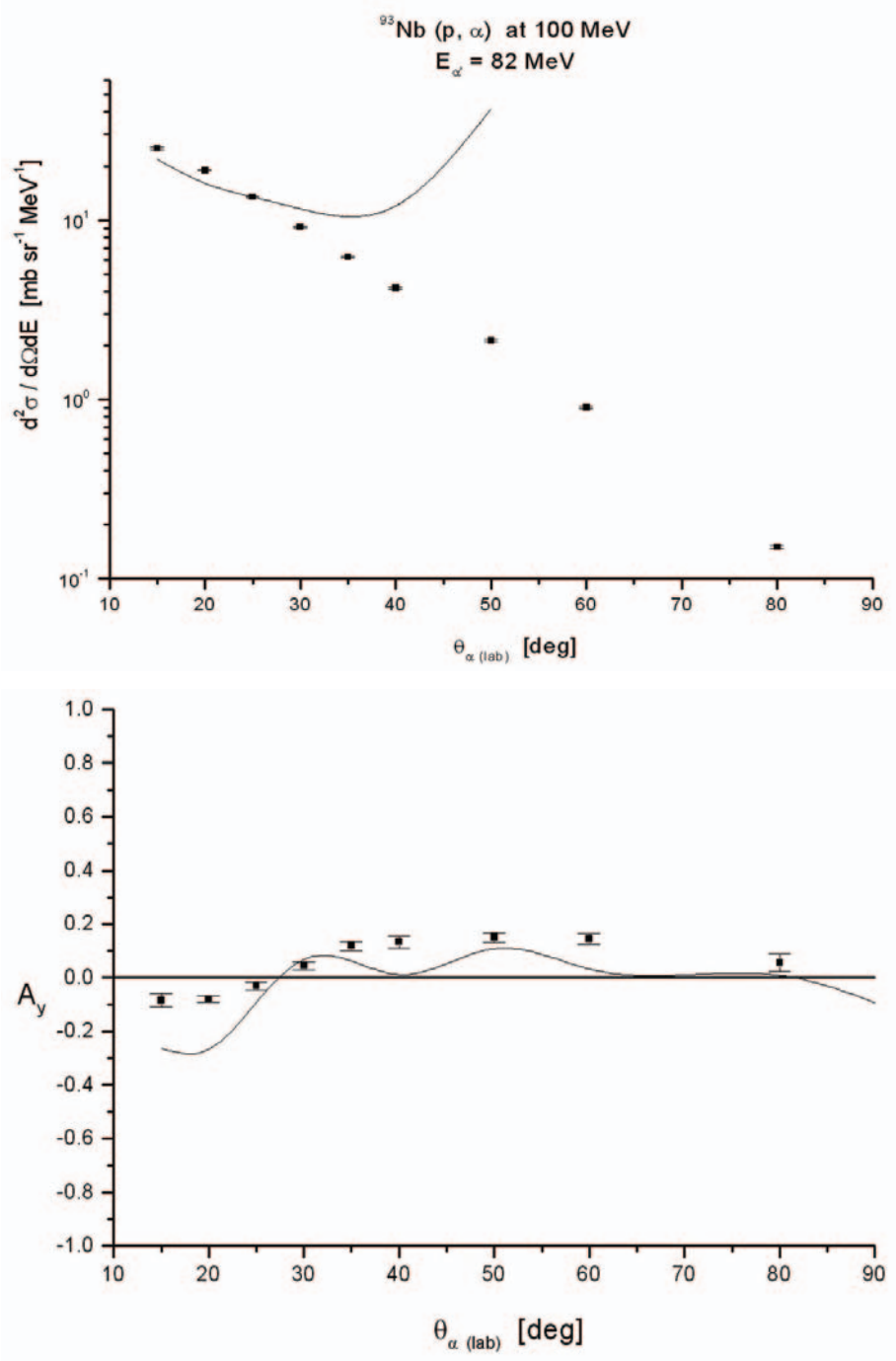

Figure 5-14: *Double differential cross section (top) and analysing power angular distributions (bottom) for the reaction ^{93}Nb (p, α) at 100 MeV incident proton energy for an outgoing α-energy of 82 MeV.*

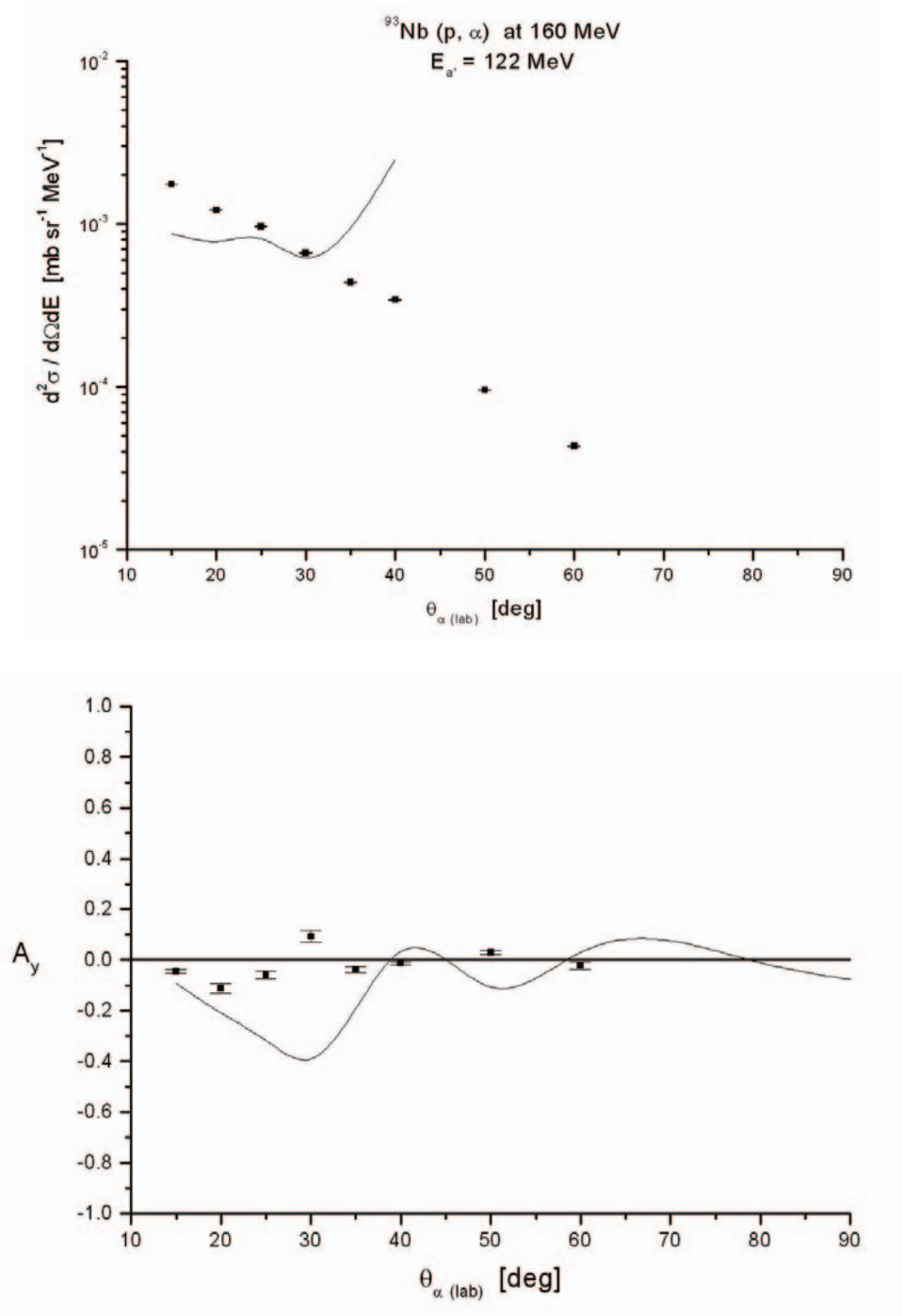

Figure 5-15: *Double differential cross section (top) and analysing power angular distributions (bottom) for the reaction ^{93}Nb (p, α) at 160 MeV incident proton energy for an outgoing α-energy of 122 MeV.*

A comparison between the analysing power angular distributions of the two different target nuclei, ^{59}Co and ^{93}Nb at an emission energy of 82 MeV is presented in **Figure 5-16**. The figure shows that there is some subtle dependence on the type of nucleus in the experimental data. This would not be unexpected as the multi-step reaction mechanism is directly related to the number of possible nucleon-nucleon collisions available.

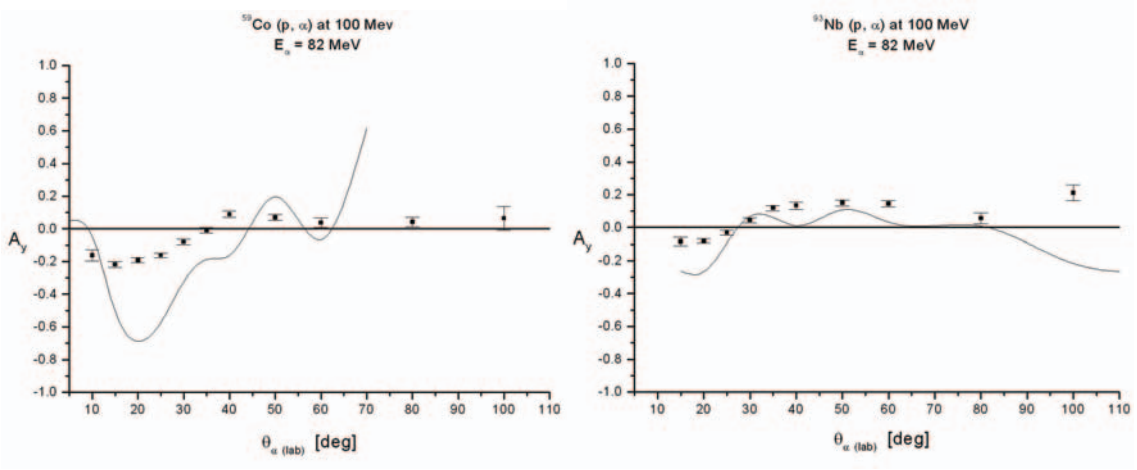

Figure 5-16: *Analysing power as a function of scattering angle for ^{59}Co (p, α) and ^{93}Nb (p, α) at 100 MeV incident energy and 82 MeV emission energy.*

In **Figure 5-17** and **Figure 5-18** the double differential cross section and analysing power angular distributions are presented for ^{59}Co and ^{93}Nb at 100 MeV showing how the DWIA calculations fail to represent the experimental data at the lower emission energies and larger scattering angles.

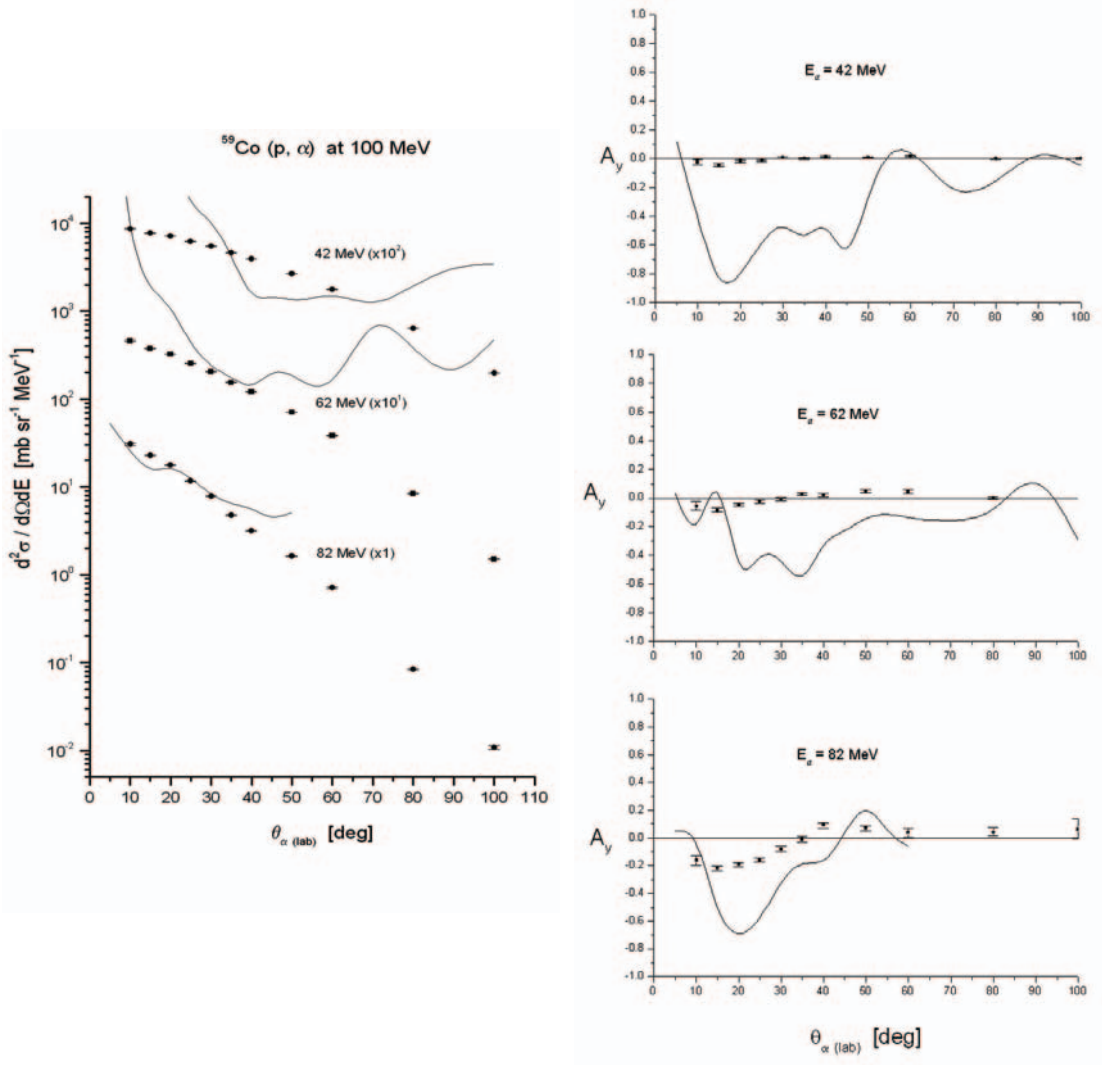

Figure 5-17: *Double differential cross section (left) and analysing power angular distributions (right) for the reaction ^{59}Co (p, α) at 100 MeV incident proton energy for different outgoing α-energies as shown. The cross section data are scaled with the factors shown in brackets to make it more distinguishable.*

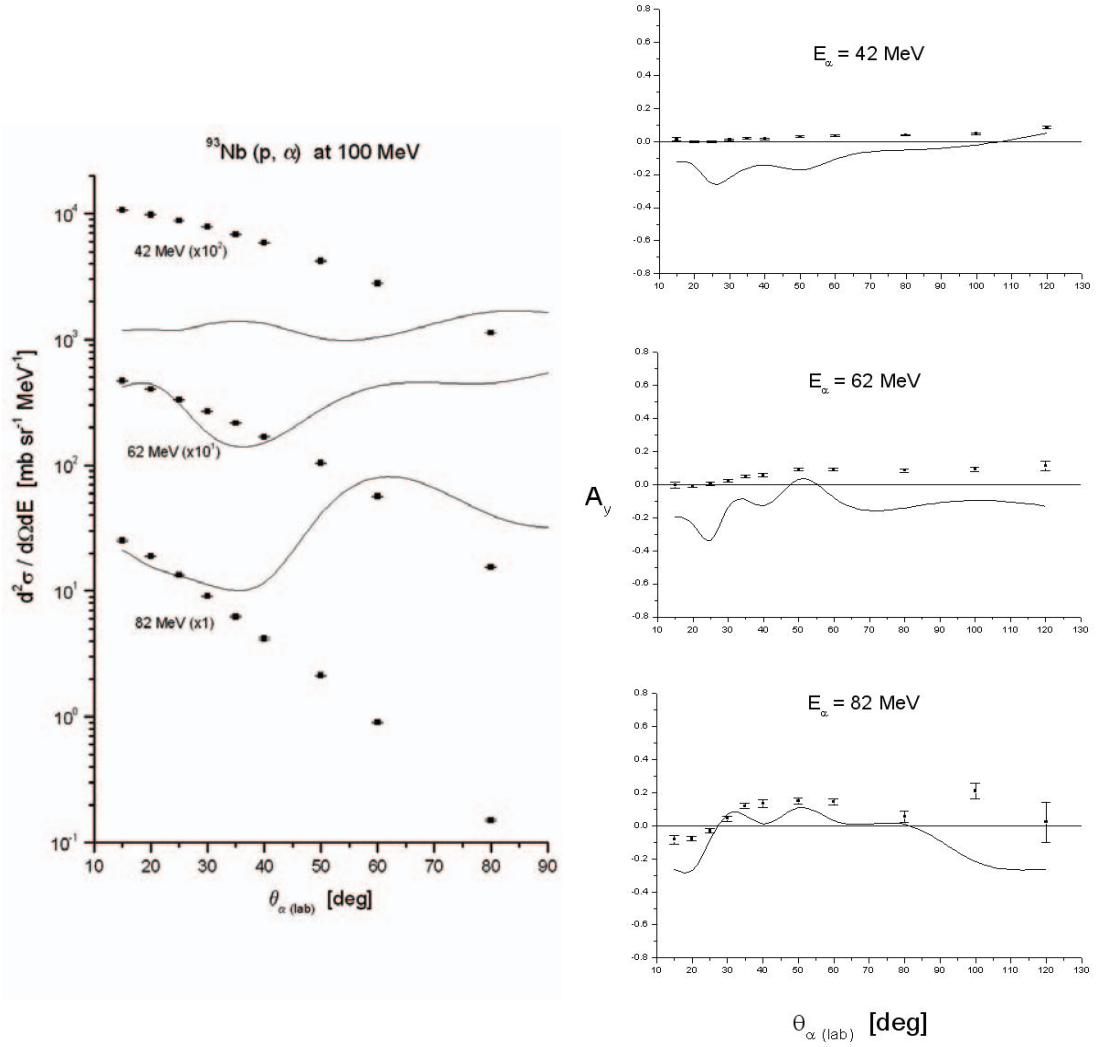

Figure 5-18: *Double differential cross section (left) and analysing power angular distributions (right) for the reaction ^{93}Nb (p, α) at 100 MeV incident proton energy for different outgoing α-energies as shown. The cross section data are scaled with the factors shown in brackets to make it more distinguishable.*

CHAPTER 6 SUMMARY AND CONCLUSION

This study has been devoted to the investigation of the inclusive (p, α) reaction and its description in terms of a simple direct cluster knock-out reaction model.

One of the two larger parts of this study was the analysis of the experimental (p, α) data obtained during an experiment done in the scattering chamber at iThemba LABS. Measurements were made on a ^{93}Nb target at an incident energy of 160 MeV and for scattering angles from 15º to 60º. This is a continuation of many experimental investigations on cluster emission reactions such as (p, α) and (p, ^{3}He), as both the emitted α-particle and helion are detected in the same experiment. The emission of the latter particle has been extensively studied using the statistical multi-step formalism and with great success.

Double differential cross section and analysing power distributions as a function of emission energy and angle were extracted and compared with theoretical predictions. Calculations were performed using the computer code THREEDEE which employs the DWIA formalism. In this model the reaction is assumed to proceed through the direct knock-out of an α-cluster in a single-step quasi-free interaction. Inclusive calculations were performed by integrating the triple differential cross sections over the solid angle of the undetected proton. Initial test calculations were made for available (p, $p\alpha$) investigations to make sure the code produces similar results. These calculations were successfully reproduced, thus inspiring confidence in our correct implementation of the code.

The analysed experimental data on ^{93}Nb were found to be consistent with other measurements of a similar kind. Guided by the results of existing multi-step reaction studies done on (p, α) and (p, ^{3}He), the aim was to see to what extent such a simple direct knock-out model is able to describe the reaction, at least qualitatively, in the region where the first-step is expected to dominate the reaction. The DWIA calculations were found to reproduce only the general trend in the double differential cross sections especially for the lower 100 MeV incident energy, and then only in the region of small emission angles less that ~30º and small excitation energies less than ~20 MeV where one would expect the direct reaction mechanism to dominate. Large discrepancies were also observed in the calculated analysing

power distributions. Some features, however, suggest that the direct knock-out process does in fact contribute to the reaction mechanism as the emission energy increases. The results of the theoretical calculations seem to be compatible with the prescription of a single-step reaction model which has been observed in pre-equilibrium multi-step reaction studies on (p, α) and (p, ^{3}He). The theoretical results of this study confirm that the first-step reaction process is mostly confined to the region of small emission angles and excitation energies, and that other effects such as the contribution of excitations in the α-cluster, which are not included in the DWIA, play a much more important role.

APPENDIX

a. Experimental data for $^{93}Nb(p,\alpha)$ at an incident energy of 160 MeV.

Angle [deg]	Energy [MeV]	$d^2\sigma/d\Omega dE$ [mb sr^{-1} MeV^{-1}]	Error in σ	A_y	Error in A_y
15	30	4.08E-03	6.56E-05	-3.48E-02	4.74E-03
	34	7.82E-02	2.87E-04	5.58E-03	4.33E-04
	38	5.69E-02	2.45E-04	8.97E-03	6.44E-04
	42	4.41E-02	2.16E-04	5.97E-05	5.97E-05
	46	3.51E-02	1.92E-04	7.79E-03	7.64E-04
	50	2.89E-02	1.75E-04	-1.82E-03	4.06E-04
	54	2.44E-02	1.60E-04	4.31E-03	6.82E-04
	58	2.03E-02	1.46E-04	2.59E-02	1.83E-03
	62	1.71E-02	1.35E-04	2.91E-03	6.69E-04
	66	1.45E-02	1.24E-04	-4.34E-03	8.87E-04
	70	1.22E-02	1.14E-04	-	-
	74	1.04E-02	1.05E-04	1.71E-02	2.08E-03
	78	8.99E-03	9.74E-05	1.49E-02	2.09E-03
	82	7.98E-03	9.18E-05	-4.48E-02	3.84E-03
	86	6.81E-03	8.48E-05	-5.06E-02	4.42E-03
	90	5.63E-03	7.71E-05	4.48E-02	4.57E-03
	94	5.06E-03	7.31E-05	6.29E-02	5.71E-03
	98	4.06E-03	6.55E-05	-4.73E-02	5.53E-03
	102	3.61E-03	6.17E-05	-2.18E-03	1.26E-03
	106	3.28E-03	5.89E-05	1.44E-02	3.40E-03
	110	2.81E-03	5.44E-05	1.12E-02	3.25E-03
	114	2.50E-03	5.14E-05	-2.84E-02	5.46E-03
	118	2.04E-03	4.64E-05	2.45E-02	5.63E-03
	122	1.76E-03	4.31E-05	-4.49E-02	8.20E-03
	126	1.49E-03	3.96E-05	3.19E-02	7.51E-03
	130	1.31E-03	3.72E-05	-4.82E-02	9.84E-03
	134	1.15E-03	3.49E-05	5.02E-02	1.07E-02
	138	9.69E-04	3.20E-05	7.87E-02	1.46E-02
	142	8.23E-04	2.95E-05	7.03E-02	1.50E-02
	146	6.61E-04	2.64E-05	2.79E-02	1.05E-02
	150	4.45E-04	2.17E-05	-1.24E-01	2.69E-02
	154	2.70E-04	1.69E-05	-1.36E-01	3.62E-02
	158	8.87E-05	9.67E-06	-6.53E-01	1.19E-01
20	30	4.48E-03	8.42E-05	1.01E-02	3.21E-03
	34	6.39E-02	3.18E-04	5.09E-02	1.90E-03
	38	5.90E-02	3.05E-04	3.56E-02	1.66E-03
	42	4.42E-02	2.64E-04	1.84E-02	1.37E-03
	46	3.58E-02	2.38E-04	4.18E-03	7.28E-04
	50	2.88E-02	2.14E-04	-2.08E-02	1.81E-03
	54	2.35E-02	1.93E-04	-1.37E-02	1.63E-03
	58	2.00E-02	1.78E-04	3.36E-02	2.76E-03
	62	1.70E-02	1.64E-04	-2.27E-02	2.46E-03
	66	1.43E-02	1.50E-04	-8.28E-03	1.62E-03
	70	1.16E-02	1.35E-04	-5.87E-03	1.52E-03

	74	9.90E-03	1.25E-04	-2.94E-02	3.67E-03
	78	8.23E-03	1.14E-04	6.62E-03	1.91E-03
	82	7.08E-03	1.06E-04	-2.57E-03	1.28E-03
	86	6.04E-03	9.78E-05	-1.95E-02	3.83E-03
	90	4.77E-03	8.68E-05	-7.53E-02	8.46E-03
	94	4.21E-03	8.16E-05	-1.51E-02	4.03E-03
	98	3.38E-03	7.31E-05	-1.48E-02	4.46E-03
	102	3.07E-03	6.97E-05	-2.36E-02	5.91E-03
	106	2.49E-03	6.27E-05	-4.38E-02	8.94E-03
	110	2.31E-03	6.05E-05	-1.77E-02	5.89E-03
	114	1.78E-03	5.31E-05	7.91E-02	1.42E-02
	118	1.43E-03	4.75E-05	5.41E-02	1.31E-02
	122	1.22E-03	4.39E-05	-1.12E-01	2.03E-02
	126	1.11E-03	4.20E-05	1.79E-01	2.68E-02
	130	8.86E-04	3.74E-05	-3.08E-02	1.26E-02
	134	7.12E-04	3.36E-05	-5.74E-02	1.91E-02
	138	6.14E-04	3.12E-05	-1.18E-01	2.95E-02
	142	4.97E-04	2.80E-05	6.40E-02	2.42E-02
	146	3.73E-04	2.43E-05	-	-
	150	3.80E-04	2.45E-05	-4.31E-01	6.85E-02
	154	2.09E-04	1.82E-05	-3.92E-01	8.88E-02
	158	1.08E-04	1.30E-05	-5.91E-01	1.44E-01
25	30	7.93E-03	9.92E-05	-1.28E-02	2.42E-03
	34	5.87E-02	2.70E-04	3.13E-02	1.39E-03
	38	5.69E-02	2.66E-04	5.53E-03	5.93E-04
	42	4.39E-02	2.34E-04	2.06E-03	4.12E-04
	46	3.39E-02	2.05E-04	2.05E-02	1.48E-03
	50	2.81E-02	1.87E-04	3.87E-04	2.23E-04
	54	2.28E-02	1.68E-04	2.15E-02	1.85E-03
	58	1.85E-02	1.52E-04	-1.27E-02	1.57E-03
	62	1.58E-02	1.40E-04	-2.17E-02	2.23E-03
	66	1.30E-02	1.27E-04	1.72E-02	2.19E-03
	70	1.06E-02	1.15E-04	1.09E-02	1.93E-03
	74	8.83E-03	1.05E-04	-1.11E-02	2.13E-03
	78	7.51E-03	9.66E-05	-4.24E-02	4.52E-03
	82	6.35E-03	8.88E-05	7.76E-02	6.64E-03
	86	5.25E-03	8.08E-05	-1.03E-02	2.67E-03
	90	4.54E-03	7.51E-05	-7.49E-02	7.72E-03
	94	3.88E-03	6.95E-05	-5.31E-02	7.03E-03
	98	3.19E-03	6.29E-05	9.09E-03	3.21E-03
	102	2.52E-03	5.59E-05	2.44E-02	5.93E-03
	106	2.10E-03	5.10E-05	4.14E-02	8.45E-03
	110	1.80E-03	4.73E-05	1.20E-02	4.91E-03
	114	1.42E-03	4.20E-05	-3.32E-02	9.20E-03
	118	1.25E-03	3.94E-05	-1.30E-01	1.93E-02
	122	9.64E-04	3.46E-05	-6.01E-02	1.50E-02
	126	8.20E-04	3.19E-05	-1.77E-02	8.83E-03
	130	6.71E-04	2.89E-05	-9.71E-02	2.28E-02
	134	4.57E-04	2.38E-05	-3.17E-02	1.58E-02
	138	4.00E-04	2.23E-05	-8.14E-02	2.71E-02
	142	2.63E-04	1.81E-05	-2.75E-02	1.94E-02
	146	1.44E-04	1.34E-05	-1.00E-01	5.01E-02
	150	1.27E-04	1.25E-05	-3.14E-01	9.25E-02
	154	7.70E-05	9.78E-06	4.70E-02	4.70E-02
	158	2.24E-05	5.27E-06	-8.09E-01	3.01E-01

30	30	6.86E-03	9.62E-05	1.57E-02	2.96E-03
	34	6.70E-02	3.01E-04	1.28E-02	8.58E-04
	38	5.07E-02	2.62E-04	7.57E-05	7.57E-05
	42	3.87E-02	2.29E-04	-3.87E-03	6.19E-04
	46	3.12E-02	2.05E-04	1.01E-02	1.12E-03
	50	2.51E-02	1.84E-04	3.13E-02	2.19E-03
	54	2.03E-02	1.65E-04	4.40E-02	2.88E-03
	58	1.70E-02	1.51E-04	1.47E-02	1.82E-03
	62	1.40E-02	1.37E-04	1.54E-02	2.05E-03
	66	1.17E-02	1.26E-04	1.44E-02	2.17E-03
	70	9.85E-03	1.15E-04	-4.68E-03	1.35E-03
	74	7.98E-03	1.04E-04	-6.26E-03	1.74E-03
	78	6.62E-03	9.45E-05	2.32E-03	1.16E-03
	82	5.56E-03	8.66E-05	4.83E-03	1.83E-03
	86	4.51E-03	7.80E-05	-7.67E-03	2.56E-03
	90	3.88E-03	7.23E-05	1.88E-02	4.32E-03
	94	3.08E-03	6.44E-05	-	-
	98	2.60E-03	5.93E-05	-1.62E-02	4.89E-03
	102	2.18E-03	5.42E-05	-5.29E-03	3.06E-03
	106	1.66E-03	4.73E-05	-2.31E-02	7.31E-03
	110	1.44E-03	4.40E-05	5.61E-02	1.22E-02
	114	1.13E-03	3.91E-05	-1.76E-01	2.43E-02
	118	9.09E-04	3.50E-05	-1.27E-02	7.32E-03
	122	6.64E-04	2.99E-05	9.26E-02	2.31E-02
	126	4.94E-04	2.58E-05	7.78E-03	7.78E-03
	130	4.26E-04	2.40E-05	-3.60E-02	1.80E-02
	134	2.64E-04	1.89E-05	1.16E-01	4.09E-02
	138	1.97E-04	1.63E-05	-5.85E-02	3.37E-02
	142	1.62E-04	1.48E-05	4.75E-02	3.35E-02
	146	1.13E-04	1.24E-05	-4.07E-01	1.13E-01
	150	5.93E-05	8.95E-06	-5.18E-01	1.70E-01
	154	2.43E-05	5.72E-06	-4.75E-01	2.58E-01
	158	1.08E-05	3.81E-06	-	-
35	30	9.76E-03	7.80E-05	-9.22E-03	1.21E-03
	34	6.95E-02	2.08E-04	1.10E-02	4.96E-04
	38	4.82E-02	1.73E-04	2.33E-02	8.65E-04
	42	3.61E-02	1.50E-04	1.31E-02	7.52E-04
	46	2.79E-02	1.32E-04	5.95E-03	5.76E-04
	50	2.24E-02	1.18E-04	8.22E-03	7.54E-04
	54	1.77E-02	1.05E-04	-1.08E-02	9.73E-04
	58	1.44E-02	9.48E-05	1.81E-02	1.40E-03
	62	1.17E-02	8.55E-05	-5.56E-03	8.57E-04
	66	9.23E-03	7.59E-05	-1.13E-02	1.38E-03
	70	7.78E-03	6.97E-05	5.58E-03	1.06E-03
	74	6.23E-03	6.23E-05	1.99E-02	2.23E-03
	78	5.01E-03	5.59E-05	4.95E-03	1.24E-03
	82	4.09E-03	5.05E-05	-4.02E-02	3.90E-03
	86	3.26E-03	4.51E-05	-3.67E-02	4.18E-03
	90	2.67E-03	4.08E-05	5.80E-03	1.84E-03
	94	2.23E-03	3.73E-05	-5.16E-02	5.99E-03
	98	1.82E-03	3.37E-05	-3.93E-02	5.79E-03
	102	1.42E-03	2.98E-05	-4.58E-02	7.06E-03
	106	1.15E-03	2.68E-05	-4.43E-02	7.71E-03
	110	9.23E-04	2.40E-05	-1.28E-01	1.46E-02

	114	7.19E-04	2.12E-05	1.73E-02	6.10E-03
	118	5.69E-04	1.88E-05	-8.72E-02	1.54E-02
	122	4.38E-04	1.65E-05	-3.90E-02	1.17E-02
	126	3.49E-04	1.48E-05	4.44E-02	1.40E-02
	130	2.60E-04	1.27E-05	-1.20E-01	2.66E-02
	134	1.90E-04	1.09E-05	-2.29E-01	4.25E-02
	138	1.42E-04	9.42E-06	-8.72E-02	3.08E-02
	142	7.99E-05	7.06E-06	-3.88E-01	8.25E-02
	146	3.24E-05	4.50E-06	-2.87E-01	1.14E-01
	150	2.50E-06	1.25E-06	-	-
40	30	5.80E-03	3.80E-05	3.65E-02	2.13E-03
	34	5.00E-02	1.12E-04	1.34E-02	4.38E-04
	38	4.60E-02	1.07E-04	1.32E-02	4.54E-04
	42	3.46E-02	9.29E-05	1.76E-02	6.05E-04
	46	2.66E-02	8.15E-05	8.24E-03	4.72E-04
	50	2.10E-02	7.23E-05	1.59E-02	7.39E-04
	54	1.65E-02	6.42E-05	6.17E-03	5.18E-04
	58	1.34E-02	5.78E-05	9.40E-03	7.11E-04
	62	1.07E-02	5.17E-05	1.20E-02	8.97E-04
	66	8.80E-03	4.69E-05	-4.41E-03	6.00E-04
	70	7.04E-03	4.19E-05	6.74E-03	8.29E-04
	74	5.58E-03	3.73E-05	-1.31E-02	1.30E-03
	78	4.51E-03	3.36E-05	2.47E-02	1.98E-03
	82	3.71E-03	3.04E-05	-2.36E-02	2.14E-03
	86	2.94E-03	2.71E-05	-2.86E-02	2.64E-03
	90	2.33E-03	2.41E-05	-9.87E-03	1.75E-03
	94	1.92E-03	2.19E-05	-1.64E-02	2.48E-03
	98	1.53E-03	1.96E-05	-1.64E-02	2.77E-03
	102	1.18E-03	1.72E-05	-2.85E-02	4.16E-03
	106	9.24E-04	1.52E-05	-1.56E-02	3.48E-03
	110	7.48E-04	1.37E-05	-2.31E-02	4.70E-03
	114	5.78E-04	1.20E-05	-8.71E-03	3.29E-03
	118	4.75E-04	1.09E-05	-6.81E-02	1.01E-02
	122	3.42E-04	9.24E-06	-1.47E-02	5.56E-03
	126	2.80E-04	8.36E-06	-3.85E-02	9.93E-03
	130	1.81E-04	6.72E-06	1.59E-02	7.95E-03
	134	9.48E-05	4.87E-06	-1.51E-02	1.07E-02
	138	6.54E-05	4.04E-06	-2.31E-01	4.97E-02
	142	3.99E-05	3.16E-06	-	-
	146	2.05E-05	2.26E-06	1.05E-01	6.06E-02
	150	1.65E-05	2.03E-06	-2.18E-01	9.64E-02
	154	4.99E-06	1.12E-06	-	-
	158	2.00E-06	7.06E-07	-7.19E-01	4.41E-01
50	30	6.75E-03	2.45E-05	2.72E-02	9.45E-04
	34	3.93E-02	5.92E-05	2.25E-02	3.56E-04
	38	2.66E-02	4.87E-05	2.01E-02	4.09E-04
	42	1.94E-02	4.16E-05	1.68E-02	4.39E-04
	46	1.48E-02	3.63E-05	7.40E-03	3.33E-04
	50	1.13E-02	3.17E-05	8.60E-03	4.11E-04
	54	8.75E-03	2.79E-05	1.16E-02	5.42E-04
	58	6.78E-03	2.46E-05	-3.04E-03	3.15E-04
	62	5.28E-03	2.17E-05	-2.94E-04	1.11E-04
	66	4.09E-03	1.91E-05	5.09E-03	5.25E-04
	70	3.14E-03	1.67E-05	-8.48E-04	2.45E-04

	74	2.48E-03	1.49E-05	-3.85E-03	5.87E-04
	78	1.91E-03	1.31E-05	8.00E-03	9.63E-04
	82	1.45E-03	1.14E-05	-1.38E-03	4.60E-04
	86	1.15E-03	1.01E-05	-9.68E-03	1.37E-03
	90	9.12E-04	9.02E-06	-1.53E-02	1.93E-03
	94	6.97E-04	7.88E-06	-3.31E-02	3.25E-03
	98	5.34E-04	6.90E-06	2.33E-02	3.11E-03
	102	4.07E-04	6.02E-06	5.18E-02	5.31E-03
	106	3.09E-04	5.25E-06	-7.90E-03	2.38E-03
	110	2.31E-04	4.54E-06	-1.44E-02	3.72E-03
	114	1.63E-04	3.82E-06	-1.77E-02	4.90E-03
	118	1.33E-04	3.45E-06	-8.33E-02	1.18E-02
	122	9.55E-05	2.92E-06	3.02E-02	8.37E-03
	126	6.66E-05	2.44E-06	-3.67E-02	1.10E-02
	130	2.91E-05	1.61E-06	2.29E-02	1.32E-02
	134	3.57E-06	5.64E-07	1.24E-01	8.75E-02
60	30	2.53E-03	2.07E-05	2.61E-03	6.98E-04
	34	3.12E-02	7.26E-05	7.58E-03	3.39E-04
	38	2.87E-02	6.96E-05	9.23E-03	3.90E-04
	42	2.03E-02	5.85E-05	1.41E-02	5.73E-04
	46	1.50E-02	5.03E-05	1.16E-02	6.06E-04
	50	1.11E-02	4.33E-05	1.62E-02	8.29E-04
	54	8.50E-03	3.79E-05	1.83E-02	1.01E-03
	58	6.39E-03	3.28E-05	1.78E-03	3.63E-04
	62	4.88E-03	2.87E-05	-9.21E-03	9.45E-04
	66	3.61E-03	2.47E-05	3.93E-04	2.27E-04
	70	2.72E-03	2.14E-05	-8.16E-03	1.19E-03
	74	2.09E-03	1.88E-05	2.72E-02	2.48E-03
	78	1.57E-03	1.63E-05	8.42E-03	1.59E-03
	82	1.17E-03	1.41E-05	-1.65E-02	2.58E-03
	86	9.23E-04	1.25E-05	-1.38E-02	2.66E-03
	90	6.62E-04	1.06E-05	2.21E-02	3.98E-03
	94	5.04E-04	9.22E-06	-8.26E-02	8.79E-03
	98	3.89E-04	8.10E-06	-2.80E-02	5.83E-03
	102	2.88E-04	6.97E-06	3.61E-02	7.70E-03
	106	2.08E-04	5.92E-06	-7.29E-02	1.29E-02
	110	1.40E-04	4.86E-06	-5.39E-02	1.35E-02
	114	1.08E-04	4.27E-06	4.81E-02	1.45E-02
	118	7.99E-05	3.67E-06	-1.48E-01	2.94E-02
	122	4.32E-05	2.70E-06	-2.19E-02	1.55E-02
	126	3.14E-05	2.30E-06	1.96E-01	5.38E-02
	130	1.89E-05	1.78E-06	-2.50E-01	7.79E-02
	134	6.75E-06	1.07E-06	-4.21E-01	1.64E-01
	138	3.71E-06	7.91E-07	1.28E-01	1.27E-01
	142	3.71E-06	7.91E-07	-3.83E-01	2.12E-01
	146	2.02E-06	5.84E-07	-	-
	150	3.37E-07	2.38E-07	-	-

b. Experimental data for ^{93}Nb(p,^{3}He) at an incident energy of 160 MeV

Angle [deg]	Energy [MeV]	$d^2\sigma/d\Omega dE$ [mb sr^{-1} MeV^{-1}]	Error in σ	A_y	Error in A_y
15	30	1.96E-02	1.44E-04	-1.13E-02	1.23E-03
	34	2.36E-02	1.58E-04	5.12E-03	7.55E-04
	38	2.16E-02	1.51E-04	-3.17E-02	1.97E-03
	42	1.96E-02	1.44E-04	1.40E-02	1.37E-03
	46	1.85E-02	1.40E-04	3.41E-03	6.97E-04
	50	1.69E-02	1.34E-04	4.21E-03	8.09E-04
	54	1.54E-02	1.28E-04	1.88E-03	5.66E-04
	58	1.49E-02	1.25E-04	-1.93E-02	1.85E-03
	62	1.40E-02	1.22E-04	1.37E-02	1.60E-03
	66	1.29E-02	1.17E-04	2.45E-03	7.08E-04
	70	1.23E-02	1.14E-04	-1.54E-02	1.81E-03
	74	1.15E-02	1.10E-04	2.28E-04	2.28E-04
	78	1.10E-02	1.08E-04	-1.96E-02	2.17E-03
	82	1.04E-02	1.05E-04	-2.14E-02	2.32E-03
	86	9.60E-03	1.01E-04	-4.11E-03	1.06E-03
	90	9.19E-03	9.85E-05	-3.15E-02	3.00E-03
	94	8.85E-03	9.67E-05	-2.97E-02	2.97E-03
	98	8.24E-03	9.33E-05	-4.53E-02	3.80E-03
	102	7.98E-03	9.18E-05	-2.87E-02	3.07E-03
	106	7.36E-03	8.81E-05	-2.04E-02	2.70E-03
	110	6.95E-03	8.56E-05	1.10E-02	2.04E-03
	114	6.46E-03	8.25E-05	-3.06E-02	3.53E-03
	118	5.87E-03	7.87E-05	2.91E-02	3.61E-03
	122	5.62E-03	7.70E-05	5.62E-02	5.12E-03
	126	5.39E-03	7.54E-05	5.37E-02	5.12E-03
	130	5.17E-03	7.39E-05	5.85E-02	5.45E-03
	134	4.66E-03	7.02E-05	8.35E-02	6.84E-03
	138	4.27E-03	6.71E-05	9.98E-02	7.82E-03
	142	3.60E-03	6.16E-05	-2.92E-03	1.46E-03
	146	2.32E-03	4.95E-05	-2.04E-02	4.81E-03
	150	7.75E-04	2.86E-05	-1.60E-01	2.31E-02
	154	4.22E-04	2.11E-05	-2.87E-01	4.11E-02
	158	2.58E-04	1.65E-05	-3.27E-01	5.58E-02
20	30	1.44E-02	1.51E-04	-1.48E-02	2.16E-03
	34	2.16E-02	1.85E-04	3.15E-03	8.14E-04
	38	1.99E-02	1.77E-04	1.37E-03	5.60E-04
	42	1.80E-02	1.69E-04	1.85E-02	2.16E-03
	46	1.68E-02	1.63E-04	-3.28E-02	2.98E-03
	50	1.53E-02	1.56E-04	-1.24E-02	1.92E-03
	54	1.44E-02	1.51E-04	5.66E-03	1.33E-03
	58	1.36E-02	1.47E-04	-1.66E-03	7.44E-04
	62	1.24E-02	1.40E-04	-2.16E-02	2.82E-03
	66	1.15E-02	1.35E-04	8.67E-03	1.85E-03
	70	1.11E-02	1.32E-04	1.31E-02	2.32E-03
	74	1.04E-02	1.28E-04	-3.37E-02	3.84E-03
	78	9.57E-03	1.23E-04	-6.46E-02	5.53E-03
	82	8.86E-03	1.18E-04	-5.13E-03	1.62E-03
	86	8.35E-03	1.15E-04	-2.01E-02	3.31E-03
	90	7.74E-03	1.11E-04	-5.51E-02	5.68E-03

	94	7.25E-03	1.07E-04	-6.20E-02	6.22E-03
	98	6.73E-03	1.03E-04	-2.23E-02	3.87E-03
	102	6.24E-03	9.94E-05	-6.04E-02	6.62E-03
	106	5.49E-03	9.32E-05	2.15E-02	4.22E-03
	110	5.08E-03	8.97E-05	-4.91E-02	6.62E-03
	114	4.56E-03	8.49E-05	-6.18E-02	7.84E-03
	118	4.14E-03	8.09E-05	-4.39E-02	6.94E-03
	122	3.62E-03	7.57E-05	-7.53E-02	9.71E-03
	126	3.11E-03	7.01E-05	-5.85E-02	9.24E-03
	130	2.63E-03	6.44E-05	-7.27E-02	1.12E-02
	134	2.35E-03	6.10E-05	-1.02E-01	1.40E-02
	138	2.26E-03	5.98E-05	-8.04E-02	1.27E-02
	142	1.87E-03	5.43E-05	-4.38E-02	1.03E-02
	146	1.57E-03	4.99E-05	-6.64E-02	1.38E-02
	150	7.02E-04	3.33E-05	-1.55E-01	3.15E-02
	154	2.88E-04	2.13E-05	-3.94E-01	7.59E-02
	158	2.59E-04	2.03E-05	-7.00E-01	9.67E-02
25	30	1.40E-02	1.32E-04	-1.79E-02	2.15E-03
	34	2.09E-02	1.61E-04	1.75E-02	1.74E-03
	38	1.91E-02	1.54E-04	-2.45E-02	2.16E-03
	42	1.76E-02	1.48E-04	-1.51E-02	1.76E-03
	46	1.60E-02	1.41E-04	3.84E-03	9.31E-04
	50	1.50E-02	1.36E-04	-1.81E-02	2.09E-03
	54	1.36E-02	1.30E-04	-3.45E-02	3.03E-03
	58	1.28E-02	1.26E-04	-8.48E-03	1.55E-03
	62	1.16E-02	1.20E-04	-2.41E-02	2.74E-03
	66	1.07E-02	1.15E-04	1.05E-02	1.88E-03
	70	1.01E-02	1.12E-04	-3.59E-04	3.59E-04
	74	9.47E-03	1.08E-04	-1.34E-02	2.26E-03
	78	8.72E-03	1.04E-04	-4.48E-02	4.31E-03
	82	7.53E-03	9.67E-05	-2.79E-02	3.66E-03
	86	7.07E-03	9.38E-05	-4.76E-02	4.93E-03
	90	6.62E-03	9.07E-05	-2.30E-02	3.54E-03
	94	5.85E-03	8.52E-05	6.19E-04	6.19E-04
	98	5.11E-03	7.97E-05	-8.50E-03	2.45E-03
	102	4.75E-03	7.68E-05	-8.23E-02	7.90E-03
	106	4.26E-03	7.27E-05	-1.62E-02	3.71E-03
	110	3.86E-03	6.93E-05	-9.56E-02	9.45E-03
	114	3.29E-03	6.39E-05	-8.81E-03	3.12E-03
	118	2.79E-03	5.89E-05	-7.26E-02	9.69E-03
	122	2.55E-03	5.63E-05	-9.37E-02	1.15E-02
	126	2.08E-03	5.08E-05	-6.97E-02	1.10E-02
	130	1.74E-03	4.65E-05	-7.91E-02	1.28E-02
	134	1.50E-03	4.32E-05	-2.41E-02	7.63E-03
	138	1.12E-03	3.72E-05	-1.62E-02	7.25E-03
	142	9.54E-04	3.44E-05	-1.29E-01	2.20E-02
	146	6.56E-04	2.86E-05	-1.88E-01	3.19E-02
	150	3.38E-04	2.05E-05	-2.14E-01	4.74E-02
	154	7.70E-05	9.78E-06	3.29E-01	1.21E-01
	158	2.49E-05	5.56E-06	-5.83E-01	2.67E-01
30	30	1.67E-02	1.50E-04	3.02E-02	2.64E-03
	34	1.93E-02	1.61E-04	9.54E-03	1.38E-03
	38	1.72E-02	1.52E-04	-2.54E-02	2.38E-03
	42	1.62E-02	1.48E-04	4.51E-03	1.03E-03

	46	1.47E-02	1.41E-04	-1.46E-02	1.95E-03
	50	1.33E-02	1.34E-04	-6.91E-03	1.41E-03
	54	1.27E-02	1.31E-04	2.53E-02	2.76E-03
	58	1.18E-02	1.26E-04	-7.46E-03	1.55E-03
	62	1.05E-02	1.19E-04	-2.57E-02	3.07E-03
	66	9.63E-03	1.14E-04	-5.98E-03	1.54E-03
	70	8.86E-03	1.09E-04	-1.04E-02	2.12E-03
	74	7.94E-03	1.03E-04	1.64E-02	2.82E-03
	78	7.52E-03	1.01E-04	-8.17E-03	2.04E-03
	82	6.83E-03	9.60E-05	-3.88E-02	4.67E-03
	86	6.16E-03	9.11E-05	-4.30E-02	5.18E-03
	90	5.31E-03	8.47E-05	-2.60E-02	4.33E-03
	94	5.11E-03	8.30E-05	-1.13E-02	2.91E-03
	98	4.52E-03	7.81E-05	-2.63E-02	4.73E-03
	102	3.88E-03	7.24E-05	-1.38E-02	3.70E-03
	106	3.46E-03	6.83E-05	-2.77E-02	5.55E-03
	110	3.04E-03	6.40E-05	-5.31E-02	8.19E-03
	114	2.51E-03	5.82E-05	7.80E-02	1.09E-02
	118	2.08E-03	5.30E-05	-4.43E-02	9.03E-03
	122	1.65E-03	4.72E-05	-1.09E-01	1.59E-02
	126	1.53E-03	4.55E-05	3.51E-02	9.37E-03
	130	1.21E-03	4.04E-05	-5.72E-02	1.35E-02
	134	1.07E-03	3.79E-05	-8.29E-02	1.73E-02
	138	7.44E-04	3.17E-05	-2.06E-02	1.03E-02
	142	5.37E-04	2.69E-05	-9.30E-02	2.57E-02
	146	4.18E-04	2.37E-05	-3.21E-01	5.29E-02
	150	1.40E-04	1.38E-05	-	-
	154	6.74E-05	9.54E-06	-7.40E-01	1.75E-01
	158	1.35E-05	4.26E-06	2.85E-01	2.79E-01
35	30	2.02E-02	1.12E-04	3.54E-03	5.22E-04
	34	2.03E-02	1.13E-04	-	-
	38	1.80E-02	1.06E-04	-1.12E-03	3.11E-04
	42	1.64E-02	1.01E-04	1.03E-02	9.86E-04
	46	1.47E-02	9.56E-05	3.39E-03	5.99E-04
	50	1.34E-02	9.15E-05	6.47E-03	8.65E-04
	54	1.19E-02	8.61E-05	2.33E-02	1.74E-03
	58	1.10E-02	8.30E-05	1.65E-02	1.52E-03
	62	9.52E-03	7.71E-05	1.11E-02	1.34E-03
	66	8.83E-03	7.42E-05	-3.95E-02	2.63E-03
	70	8.03E-03	7.08E-05	1.55E-03	5.46E-04
	74	7.18E-03	6.69E-05	-1.47E-02	1.78E-03
	78	6.39E-03	6.31E-05	-4.15E-02	3.17E-03
	82	5.93E-03	6.08E-05	-2.22E-02	2.41E-03
	86	5.02E-03	5.60E-05	-1.48E-02	2.14E-03
	90	4.46E-03	5.28E-05	1.32E-02	2.14E-03
	94	3.83E-03	4.89E-05	-1.94E-02	2.80E-03
	98	3.41E-03	4.61E-05	-5.46E-03	1.58E-03
	102	2.89E-03	4.24E-05	-1.34E-02	2.69E-03
	106	2.41E-03	3.87E-05	-	-
	110	2.07E-03	3.60E-05	-1.27E-02	3.09E-03
	114	1.65E-03	3.21E-05	-9.42E-02	9.39E-03
	118	1.40E-03	2.95E-05	-3.66E-02	6.37E-03
	122	1.05E-03	2.56E-05	-7.41E-03	3.31E-03
	126	8.66E-04	2.32E-05	-8.96E-02	1.26E-02
	130	6.08E-04	1.95E-05	-1.51E-01	1.95E-02

	134	3.81E-04	1.54E-05	-1.26E-01	2.26E-02
	138	2.38E-04	1.22E-05	-1.63E-01	3.23E-02
	142	9.98E-05	7.89E-06	-1.24E-01	4.37E-02
	146	4.87E-05	5.51E-06	-4.78E-01	1.14E-01
	150	2.25E-05	3.74E-06	-4.14E-01	1.59E-01
	154	6.24E-06	1.97E-06	-7.46E-01	3.44E-01
40	30	1.22E-02	5.51E-05	3.90E-03	4.80E-04
	34	1.81E-02	6.72E-05	4.45E-03	4.21E-04
	38	1.59E-02	6.29E-05	4.62E-03	4.58E-04
	42	1.44E-02	5.99E-05	-1.45E-03	2.69E-04
	46	1.30E-02	5.69E-05	-4.82E-03	5.17E-04
	50	1.17E-02	5.40E-05	-1.42E-02	9.35E-04
	54	1.06E-02	5.14E-05	-2.13E-02	1.20E-03
	58	9.51E-03	4.87E-05	-2.24E-02	1.30E-03
	62	8.54E-03	4.62E-05	2.02E-03	4.12E-04
	66	7.65E-03	4.37E-05	-1.03E-02	9.84E-04
	70	6.91E-03	4.15E-05	-1.73E-02	1.34E-03
	74	6.10E-03	3.90E-05	6.24E-03	8.57E-04
	78	5.35E-03	3.65E-05	7.39E-03	9.96E-04
	82	4.75E-03	3.44E-05	-1.86E-02	1.68E-03
	86	4.11E-03	3.20E-05	2.97E-03	7.20E-04
	90	3.65E-03	3.02E-05	-1.24E-02	1.56E-03
	94	3.14E-03	2.80E-05	2.84E-02	2.55E-03
	98	2.72E-03	2.60E-05	-1.88E-02	2.23E-03
	102	2.32E-03	2.41E-05	2.23E-02	2.62E-03
	106	1.98E-03	2.22E-05	-2.43E-02	2.97E-03
	110	1.70E-03	2.06E-05	4.22E-04	4.22E-04
	114	1.42E-03	1.88E-05	2.53E-03	1.13E-03
	118	1.16E-03	1.70E-05	-5.71E-02	5.95E-03
	122	9.55E-04	1.54E-05	-7.60E-02	7.55E-03
	126	7.23E-04	1.34E-05	-1.79E-02	4.22E-03
	130	5.28E-04	1.15E-05	-1.36E-03	1.36E-03
	134	4.39E-04	1.05E-05	1.31E-01	1.46E-02
	138	3.42E-04	9.24E-06	-4.83E-02	1.01E-02
	142	1.97E-04	7.02E-06	-4.01E-02	1.21E-02
	146	1.17E-04	5.40E-06	1.23E-02	8.70E-03
	150	3.64E-05	3.02E-06	-4.14E-01	8.65E-02
	154	1.20E-05	1.73E-06	4.80E-01	1.60E-01
	158	1.20E-05	1.73E-06	-3.60E-01	1.42E-01
50	30	1.22E-02	3.29E-05	7.02E-03	3.58E-04
	34	1.17E-02	3.23E-05	-2.64E-03	2.24E-04
	38	1.01E-02	3.01E-05	7.76E-03	4.12E-04
	42	8.91E-03	2.82E-05	-7.07E-03	4.20E-04
	46	7.76E-03	2.63E-05	-5.66E-03	4.02E-04
	50	6.78E-03	2.46E-05	2.49E-03	2.85E-04
	54	5.96E-03	2.31E-05	4.06E-03	3.89E-04
	58	5.22E-03	2.16E-05	-1.90E-02	8.99E-04
	62	4.51E-03	2.01E-05	8.01E-03	6.27E-04
	66	3.92E-03	1.87E-05	-1.28E-02	8.53E-04
	70	3.40E-03	1.74E-05	-8.62E-03	7.50E-04
	74	2.88E-03	1.60E-05	-2.39E-03	4.29E-04
	78	2.45E-03	1.48E-05	4.99E-03	6.73E-04
	82	2.07E-03	1.36E-05	-2.76E-02	1.72E-03
	86	1.74E-03	1.25E-05	-8.14E-03	1.02E-03

	90	1.46E-03	1.14E-05	-5.92E-03	9.48E-04
	94	1.24E-03	1.05E-05	1.52E-02	1.65E-03
	98	9.90E-04	9.40E-06	-7.61E-03	1.31E-03
	102	8.22E-04	8.56E-06	2.43E-03	8.09E-04
	106	6.52E-04	7.63E-06	3.33E-02	3.37E-03
	110	5.10E-04	6.75E-06	-2.61E-03	1.06E-03
	114	3.86E-04	5.87E-06	2.18E-02	3.54E-03
	118	2.95E-04	5.13E-06	-4.96E-02	6.10E-03
	122	2.18E-04	4.41E-06	-6.41E-02	8.07E-03
	126	1.50E-04	3.66E-06	-1.47E-03	1.47E-03
	130	9.51E-05	2.91E-06	-6.76E-02	1.25E-02
	134	4.66E-05	2.04E-06	-5.24E-02	1.58E-02
	138	9.81E-06	9.36E-07	-1.13E-01	5.03E-02
	142	1.78E-07	1.26E-07	-	-
60	30	8.01E-03	3.68E-05	-2.30E-02	1.16E-03
	34	1.23E-02	4.55E-05	-7.76E-03	5.47E-04
	38	1.03E-02	4.18E-05	-9.70E-03	6.66E-04
	42	8.85E-03	3.86E-05	1.39E-03	2.73E-04
	46	7.55E-03	3.57E-05	-1.11E-02	8.35E-04
	50	6.40E-03	3.28E-05	-1.30E-02	9.81E-04
	54	5.60E-03	3.07E-05	6.75E-03	7.55E-04
	58	4.83E-03	2.85E-05	-1.08E-03	3.25E-04
	62	4.06E-03	2.62E-05	-2.06E-02	1.55E-03
	66	3.38E-03	2.39E-05	-1.05E-02	1.21E-03
	70	2.88E-03	2.20E-05	-1.64E-02	1.64E-03
	74	2.34E-03	1.98E-05	1.11E-02	1.50E-03
	78	1.96E-03	1.82E-05	1.40E-02	1.84E-03
	82	1.59E-03	1.64E-05	5.36E-03	1.26E-03
	86	1.31E-03	1.49E-05	1.19E-02	2.07E-03
	90	1.05E-03	1.33E-05	2.88E-02	3.60E-03
	94	8.50E-04	1.20E-05	4.12E-02	4.79E-03
	98	6.80E-04	1.07E-05	2.99E-02	4.56E-03
	102	5.26E-04	9.42E-06	3.68E-02	5.75E-03
	106	4.07E-04	8.28E-06	6.28E-02	8.54E-03
	110	3.11E-04	7.24E-06	7.77E-02	1.09E-02
	114	2.28E-04	6.20E-06	6.03E-02	1.12E-02
	118	1.65E-04	5.27E-06	-2.01E-02	7.59E-03
	122	1.31E-04	4.69E-06	-3.99E-02	1.20E-02
	126	9.38E-05	3.98E-06	1.21E-01	2.46E-02
	130	5.94E-05	3.16E-06	1.12E-01	2.97E-02
	134	2.46E-05	2.04E-06	-2.50E-01	6.82E-02
	138	1.52E-05	1.60E-06	-2.18E-01	8.15E-02
	142	6.07E-06	1.01E-06	-4.68E-01	1.80E-01
	146	2.70E-06	6.75E-07	-3.51E-01	2.40E-01
	150	2.36E-06	6.31E-07	2.00E-01	1.98E-01
	154	6.75E-07	3.37E-07	-	-
	158	3.37E-07	2.38E-07	-	-

c. Analysing power calculations for ^{59}Co around at 82 MeV emission energy.

Based on the reasonably good agreement between the theoretical calculations and the data for the analysing power angular distributions of ^{59}Co at 100 MeV incident and 82 MeV emission energy, **Figure 5-17**, it is instructive to see what the THREEDEE calculations give for a few energies around ~80 MeV. This is shown in **Figure 6-2** here in the appendix. At emission energies below ~84 MeV the THREEDEE calculations always tend to underestimate the analysing power at the smaller angles. At 84 MeV the general trend of the calculation, though still less, corresponds well with the data. At 85 MeV and, in particular 86 MeV, the calculations oscillate around an average that seems to follow the experimental data. This is indicated in **Figure 6-1** where a Gaussian mean has been drawn through the theoretical values. The agreement is very promising. It is as yet not clear whether this large oscillating behaviour is due to kinematics or a numerical problem in the computer code.

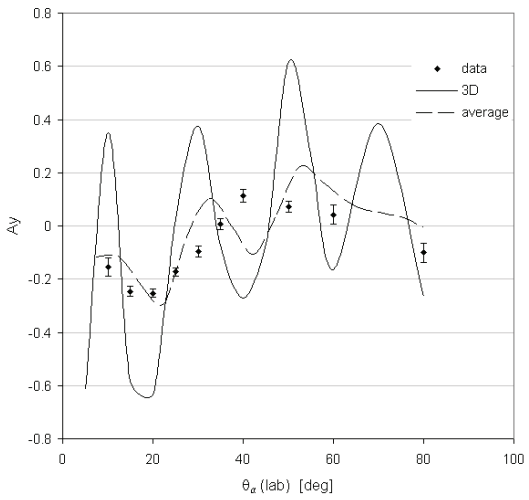

Figure 6-1: *Plot of the analysing power for ^{59}Co (p, α) at 100 MeV and 86 MeV emission energy. The dashed line represents a Gaussian average of the THREEDEE calculation.*

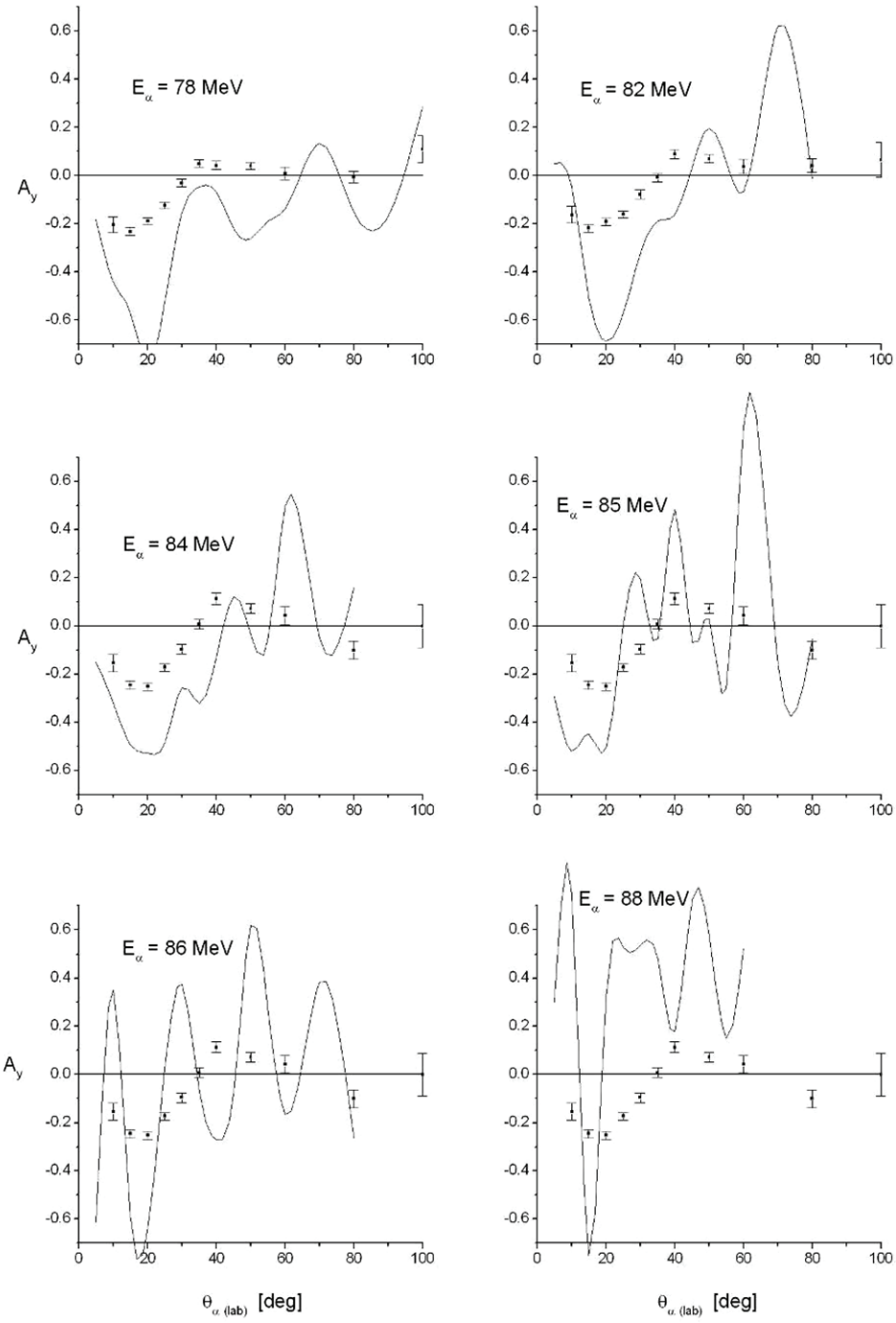

Figure 6-2: *Analysing power as a function of scattering angle for ^{59}Co (p, α) at 100 MeV and emission energies in smaller increments around ~83 MeV as indicated.*

d. Derivation of the absolute differential cross section and analysing power

During the experiment the direction of the beam polarisation was switched between up and down every 10 seconds. From the definition of the differential cross section for scattering at an angle θ to either the left or right of the incident beam direction, and with polarisation up or down, equation (4.3.7) is written as

$$\sigma^{\uparrow\downarrow}(\theta_L) = \sigma_0(\theta)\left(1 \pm p_{\uparrow\downarrow} A_y\right),$$

and

$$\sigma^{\uparrow\downarrow}(\theta_R) = \sigma_0(\theta)\left(1 \mp p_{\uparrow\downarrow} A_y\right)$$

with special emphasis on the different signs for scattering to the left and right. From the symmetry of the setup, the scattering of a beam of particles to the left and with spins pointing up is equivalent to the scattering of a beam of particles to the right with their spins pointing down, i.e.

$$\sigma^{\uparrow(\downarrow)}(\theta_L) = \sigma^{\downarrow(\uparrow)}(\theta_R) \tag{7.2.1}$$

and the unpolarised cross section, σ_0 , which is independent of spin, is common to both scattering to the left and right.

From these equations we can write

$$\left(\sigma_L^{\uparrow} - \sigma_L^{\downarrow}\right) - \left(\sigma_R^{\uparrow} - \sigma_R^{\downarrow}\right) = 2\sigma_0 A_y \left(p_{\uparrow} + p_{\downarrow}\right)$$

and

$$\sigma_L^{\uparrow} + \sigma_L^{\downarrow} + \sigma_R^{\uparrow} + \sigma_R^{\downarrow} = 4\sigma_0$$

so that the absolute differential cross section for zero polarisation, σ_0, is simply

$$\sigma_0 = \tfrac{1}{4}\left(\sigma_L^{\uparrow} + \sigma_L^{\downarrow} + \sigma_R^{\uparrow} + \sigma_R^{\downarrow}\right) \tag{7.2.2}$$

which is just the average of the differential cross sections for both detectors, left and right, and incident beam polarisation up and down.

The analysing power for a specific angle can then be calculated, as used by Moss *et al.* [Mos80], from

$$A_y(\theta) = \frac{2}{\left(p_\uparrow + p_\downarrow\right)} \frac{\sigma_L^\uparrow + \sigma_R^\downarrow - \sigma_L^\downarrow - \sigma_R^\uparrow}{\sigma_L^\uparrow + \sigma_R^\downarrow + \sigma_L^\downarrow + \sigma_R^\uparrow}. \tag{7.2.3}$$

In the case where the experiment is done with only one detector, positioned at a specific angle left (or right) of the incident beam direction, the analysing power can be calculated as

$$A_y(\theta) = \frac{\sigma_\uparrow - \sigma_\downarrow}{\sigma_0\left(p_\uparrow + p_\downarrow\right)},$$

which can further be written as

$$A_y(\theta) = \frac{\sigma_\uparrow - \sigma_\downarrow}{p_\downarrow\sigma_\uparrow + p_\uparrow\sigma_\downarrow}. \tag{7.2.4}$$

If the polarisations up and down are very similar, i.e. $p_\uparrow \approx p_\downarrow$, the analysing power is simply given by

$$A_y(\theta) \approx \frac{1}{p}\left(\frac{\sigma_\uparrow - \sigma_\downarrow}{\sigma_\uparrow + \sigma_\downarrow}\right) \tag{7.2.5}$$

where p is the average polarisation. This approximation holds to within ~1%.

We can express the absolute differential cross section for zero polarisation, σ_0, as

$$\sigma_0 = \frac{\sigma_\uparrow + \sigma_\downarrow}{2 + A_y\left(p_\uparrow - p_\downarrow\right)},$$

which simplifies to

$$\sigma_0 = \frac{p_\uparrow\sigma_\downarrow + p_\downarrow\sigma_\uparrow}{p_\uparrow + p_\downarrow}. \tag{7.2.6}$$

If the difference in polarisation up and down is very small, this equation reduces to

$$\sigma_0 \approx \frac{\sigma_\uparrow + \sigma_\downarrow}{2}. \tag{7.2.7}$$

e. Derivation of the analysing power for the inclusive (p, α) reaction

The analysing power for the inclusive (*p*, α) reaction when detecting the α-particle at an angle θ_α to the left (or right) of the incident beam direction, is given, from equation (7.2.4), by

$$A_{(p,\alpha)}(\theta_\alpha) = \frac{d^2\sigma^{\uparrow}(\theta_\alpha) - d^2\sigma^{\downarrow}(\theta_\alpha)}{p_{\downarrow} d^2\sigma^{\uparrow}(\theta_\alpha) + p_{\uparrow} d^2\sigma^{\downarrow}(\theta_\alpha)}. \tag{7.3.1}$$

where $d^2\sigma^{\uparrow(\downarrow)}(\theta_\alpha)$ represents the double differential cross section for the scattering of the α-particle to an angle θ_α when the incident beam polarisation was up (down).

The double differential cross section is just the integral of the triple differential cross section over the solid angle of the unobserved proton, i.e.

$$d^2\sigma \equiv \frac{d^2\sigma(\theta_\alpha)}{d\Omega_\alpha dE_\alpha} = \int_{\Omega_p} d\Omega_p \frac{d^3\sigma(\theta_\alpha, \theta_p)}{d\Omega_p d\Omega_\alpha dE_\alpha}. \tag{7.3.2}$$

The analysing power then becomes

$$A_{(p,\alpha)}(\theta_\alpha) = \frac{\int d\Omega_p \left[d^3\sigma^{\uparrow}(\theta_\alpha, \theta_p) - d^3\sigma^{\downarrow}(\theta_\alpha, \theta_p) \right]}{\int d\Omega_p \left[p_{\downarrow} d^3\sigma^{\uparrow}(\theta_\alpha, \theta_p) + p_{\uparrow} d^3\sigma^{\downarrow}(\theta_\alpha, \theta_p) \right]}.$$

Using equation (4.3.7) for the triple differential cross section, this can be written as

$$A_{(p,\alpha)}(\theta_\alpha) = \frac{\int d\Omega_p \left[A_{(p,p\alpha)}(\theta_\alpha, \theta_p) \times d^3\sigma_0(\theta_\alpha, \theta_p) \times \left(p_{\uparrow} + p_{\downarrow} \right) \right]}{\int d\Omega_p \left[d^3\sigma_0 \left(2 + A_{(p,p\alpha)}(\theta_\alpha, \theta_p) \times \left(p_{\uparrow} - p_{\downarrow} \right) \right) \right]}$$

where $A_{(p,p\alpha)}(\theta_\alpha, \theta_p)$ is the analysing power for the coincidence reaction (*p*, *pα*) when detecting the proton and α-particle at angles θ_p and θ_α, respectively.

As the difference in $p_\uparrow$ and $p_\downarrow$ is usually not very large, and $A_{(p,p\alpha)} \leq 1$, the analysing power for the inclusive (*p, α*) reaction reduces to

$$A_y(\theta_\alpha) \approx \frac{\int d\Omega_p A_{(p,p\alpha)}(\theta_\alpha,\theta_p)\frac{d^3\sigma_0(\theta_\alpha,\theta_p)}{d\Omega_p d\Omega_\alpha dE_\alpha}}{\int d\Omega_p \frac{d^3\sigma_0(\theta_\alpha,\theta_p)}{d\Omega_p d\Omega_\alpha dE_\alpha}}. \qquad (7.3.3)$$

For the inclusive calculations done by Cowley *et al.* [Cow02], the (*p, pα*) analysing power in equation (7.3.3) was approximated by the two-body analysing power, $A_{p-\alpha}(\theta_p)$, for the elastic scattering of the incident proton from the α-cluster.

f. THREEDEE program inputs and structure

Input parameters are read in by the main routine THREEDEE via an input file containing all the bound particle quantum numbers, the masses and charges of the interacting particles, integration parameters, the different optical potential parameters and the kinematic quantities for the reaction. The data output is managed by a few possible integer flags called jcon-parameters. Optical potentials can be selected from a list of available energy-dependent potential parameter sets.

The structure of the program is presented in the flowchart below. After the initial input cards are read, the program calculates the bound state wave function. Then, for each reaction, *a* + A, *c* + B, *d* + B and *p* + ^{4}He (in the case of bound *α*-cluster reactions), the distorted wave functions are determined in the subroutine DSTWF using the selected potential sets found in the subroutine POTSET. The program then calculates the reaction kinematics, i.e. the energies, momenta and angles for each set of kinematic conditions, using the subroutine PROLOG. For each set of angles and energies the subroutine EPILOG is called to calculate observables such as the cross section and analysing power.

The program finally prints all the selected values in a plot-file as well as a list-file containing the wave functions, S-matrix elements, potentials, kinematics etc.

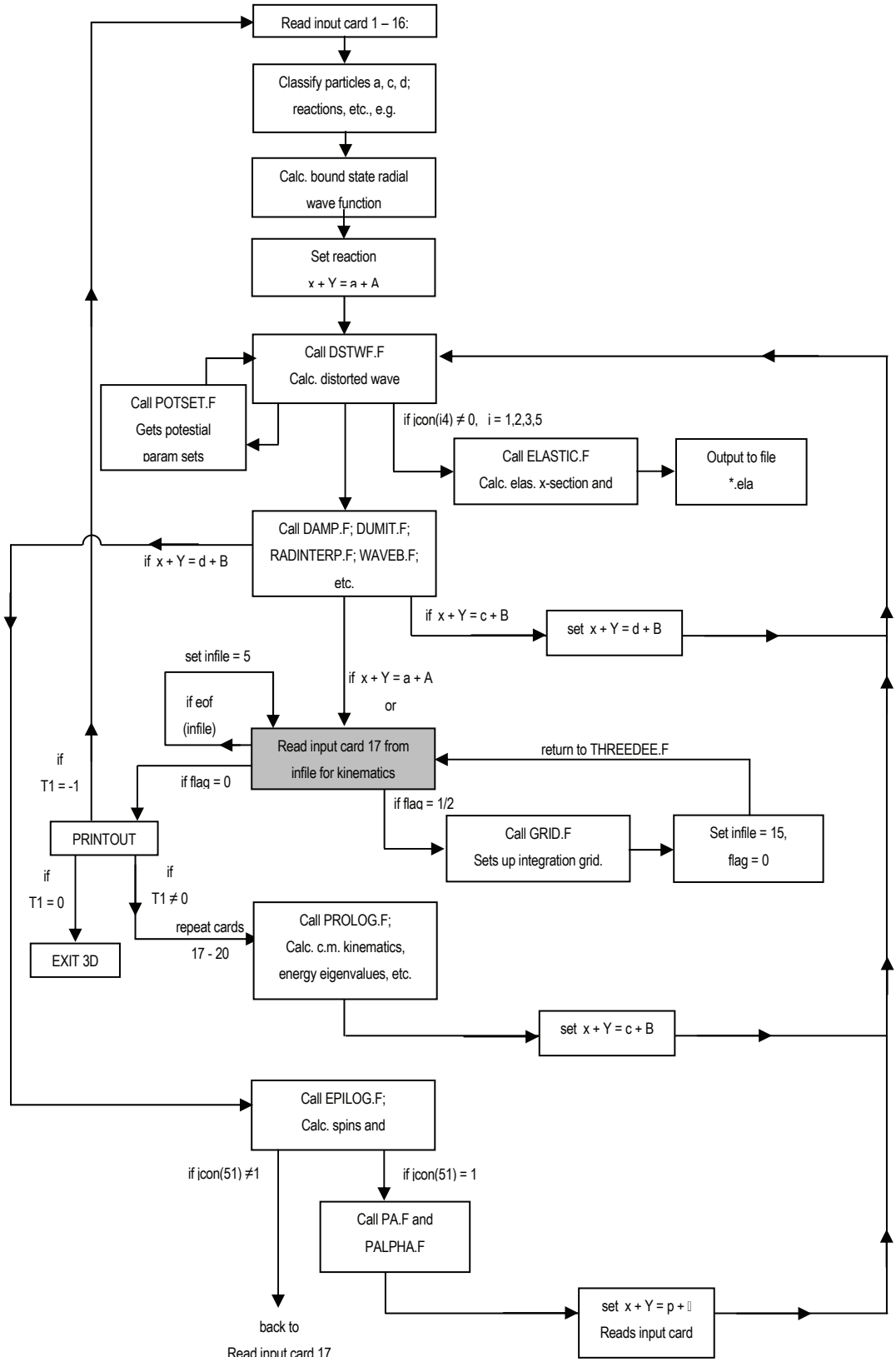

Figure 6-3: *Logic flow chart for the computer code THREEDEE.*

g. Detector solid angle measurements

The dimensions of the collimators and target ladder were measured before the experiments and recorded in the logbook. The measured values are given in the figure below. The subtended solid angle is calculated from the following defining equation:

$$\Omega = 2\pi\left[1-\cos\left(\tan^{-1}\left(\frac{d}{2D}\right)\right)\right],$$

where d is the diameter of the collimator opening and D, target-collimator distance measured as indicated in the diagram below.

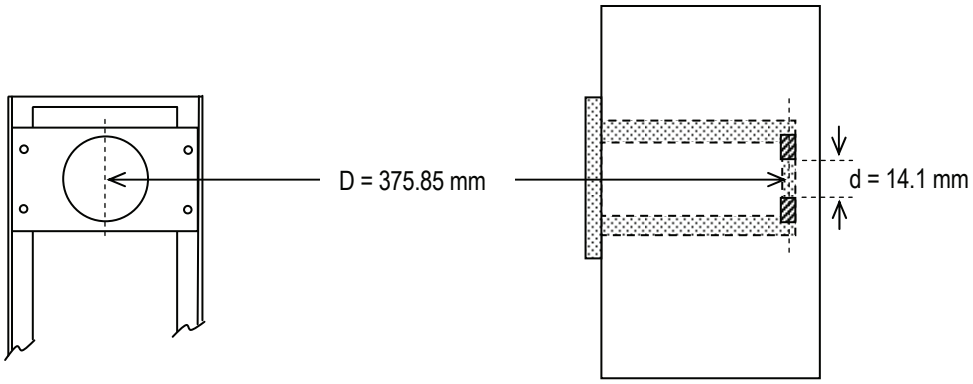

Figure 6-4: *Diagram showing the dimensions of the target ladder and collimator setup.*

h. Numerical integration

The method used in the numerical integration of the inclusive cross sections and analysing powers is based on an N-point Gauss-Legendre quadrature. The integration is based on the following approximation rule:

$$\int_{-1}^{1} f(x)dx \cong \sum_{i=1}^{N} \omega_i f(x_i)$$

where $\{\omega_i\}$ are the weights and $\{x_i\}$ the roots of the Legendre polynomial of order N. The weights and roots can usually be looked up in appropriate tables. The integration limits can be adjusted using the following equation:

$$\int_{a}^{b} f(x)dx = \frac{b-a}{4}\int_{-1}^{1} f\left((b-a)x+(b+a)\right)dx\,.$$

A section of the FORTRAN code INTEGRATE, which was written to do this integration, is given below.

```
      program INTEGRATE
...
...
      do k=1,nt1
          asig=0.0
          sig=0.0

          do j=1,nthd
            do i=1,nbetad
                read (55,100,end=901,err=990) t1, es, tc, td, betad
     .                , t0eff, theff, A3b00i0
                asig=asig + wthd(j)*wbetad(i)*A3b00i0*es
                sig=sig + wthd(j)*wbetad(i)*es
            end do
          end do
          ay=asig/sig
          asig=asig*ABS(thdf - thdi)*ABS(betdf - betdi)/4.0
          sig=sig*ABS(thdf - thdi)*ABS(betdf - betdi)/4.0
          write(66,103) t1,tc,sig,ay
      end do
      go to 888
...
...
      End program INTEGRATE
```

REFERENCES

Are94 - G.J. Arendse, *Pre-equilibrium Excitation of Nuclei in (p, α) and (p,^{3}He) Reactions Induced by 120, 160 and 200 MeV Protons*, MSc thesis, University of Stellenbosch (1994).

Are97 - G.J. Arendse, *Nuclear Distortions in the (p,2p) Knock-out Reaction on ^{208}Pb at a Incident Energy of 200 MeV*, PhD thesis, University of Stellenbosch (1997).

Bez06 - J. Bezuidenhout, *Pre-equilibrium Helion Emission Induced by Protons*, PhD thesis, University of Stellenbosch (2006).

Bon89 - R. Bonetti, F. Crespi, and K.-I. Kubo, *The ^{58}Ni (p,α) Reaction Mechanism through a Study of the Analyzing Power*, Nucl. Phys. A499, 381 (1989).

Bur95 - W.E. Burcham and M. Jones, *Nuclear and Particle Physics* (Longman Scientific & Technical, England, 1995).

Car84 - T.A. Carey, P.G. Roos, N.S. Chant, A. Nadasen, and H.L. Chen, *Alpha-particle Spectroscopic Strengths using the (p, pα) Reaction at 101.5 MeV*, Phys. Rev. C 29, 1273 (1984).

Cha3D - N.S. Chant, Program THREEDEE, University of Maryland, unpublished.

Cha77 - N.S. Chant and P.G. Roos, *Distorted-Wave Impulse-Approximation Calculations for Quasifree Cluster Knock-out Reactions*, Phys. Rev. C 15, 57 (1977).

Cha83 - N.S. Chant and P.G. Roos, *Spin Orbit Effects in Quasi-free Knock-out Reactions*, Phys. Rev. C 27, 1060 (1983).

Cow91 - A.A. Cowley, A. van Kent, J.J. Lawrie, S.V. Förtsh, D.M. Whittal, J.V. Pilcher, F.D. Smit, W.A. Richter, R. Lindsay, I.J. van Heerden, R. Bonetti, and P.E. Hodgson, *Pre-equilibrium Proton Emission Induced by 80 and 120 MeV Protons Incident on ^{90}Zr*, Phys. Rev. C 43, 678 (1991).

Cow96 - A.A. Cowley, G.J. Arendse, J.W. Koen, W.A. Richter, J.A. Stander, G.F. Steyn, S.S. Dimitrova, P.E. Hodgson, and Y. Watanabe, *Inclusive (p,α) Reactions on ^{27}Al, ^{59}Co and ^{197}Au at Incident Energies of 120, 160 and 200 MeV*, Phys. Rev. C 54, 778 (1996).

Cow97 - A.A. Cowley, G.J. Arendse, G.F. Steyn, J.A. Stander, W.A. Richter, S.S. Dimitrova, P. Demetriou, and P.E. Hodgson, *Inclusive (p, ^{3}He) Reactions on ^{59}Co and ^{197}Au at Incident Energies of 120, 160 and 200 MeV*, Phys. Rev. C 55, 1843 (1997).

Cow00 - A.A. Cowley, G.F. Steyn, S.S. Dimitrova, P.E. Hodgson, G.J. Arendse, S.V. Förtsch, G.C. Hillhouse, J.J. Lawrie, R. Neveling, W.A. Richter, J.A. Stander, and S.M. Wyngaardt, *Multi-step Direct Mechanism in the ($\vec{p}$,^{3}He) Inclusive Reaction on ^{59}Co and ^{93}Nb at an Incident Energy of 100 MeV*, Phys. Rev. C 62, 064605 (2000).

Cow02 - A.A. Cowley, S.V. Förtsch, G.F. Steyn, S. Dimitrova, and P.E. Hodgson, *Comparison between Analysing Powers from the Inclusive Reactions* $(\vec{p},\alpha)$ *and ($\vec{p}$,^{3}He) on ^{59}Co at an Incident Energy of 100 MeV*, J. Nucl. Science and Tech., Suppl. 2, 742 (2002).

Dem96 - P. Demetriou and P.E. Hodgson, *The Energy Dependence of the Proton-Alpha Reaction to Continuum States*, J. Phys. G: Nucl. Part. Phy. 22, 1813 (1996).

Fes92 - Herman Feshbach, *Theoretical Nuclear Physics, Nuclear Reaction* (John Wiley & Sons, 1992).

För92 - S.V. Förtsch, *Proton Emission in Pre-equilibrium Reactions Induced by Incident Protons of 100 to 200 MeV*, PhD thesis, University of Pretroria (1992).

Gad84 - E. Gadioli, E. Gadioli-Erba, P. Gauzzoni, P.E. Hodgson, and L. Zetta, *The Mechanism of the (p, α) Reaction: Pick-up or Knock-out?*, Zeitschrift für Physik A 318, 147 (1984).

Gle83 - Norman K. Glendenning, *Direct Nuclear Reactions* (Academic Press, Inc. New York, 1983).

Hae74 - W. Haeberli, *Nuclear Spectroscopy and Reactions (Part A); Polarisation Experiments; Polarised Beams*, edited by J. Cerny (California, 1974).

Hil90 - G.C. Hillhouse, *Nuclear Reactions with Polarised Spin-½ Beams*, MSc thesis, University of Stellenbosch (1990).

Hod97 - P.E. Hodgson, *The Nuclear Optical Model - Introductory Overview*, Nuclear Physics Laboratory, Dept. of Physics, University of Oxford, Oxford.

Hod00 - P.E. Hodgson, E. Gadioli, and E. Gadioli Erba, *Introductory Nuclear Physics* (Oxford University Press, New York, 1997).

Hod02 - P.E. Hodgson, *Alpha-Particle Clustering in Nuclear Reactions*, Contemporary Physics 43, 461 (2002).

Hod03 - P.E. Hodgson and E. Běták, *Cluster Emission, Transfer and Capture in Nuclear Reactions*, Physics Reports 374, 1 (2003).

Lew82 - Z. Lewandowski, E. Loeffler, R. Wagner, H.H. Mueller, W. Reichart, and P. Schober, *Analyzing Power in the Continuum of the ($\vec{p}$, αx) and ($\vec{p}$, τx) Reactions on ^{12}C, ^{27}Al, ^{58}Ni, ^{90}Zr, ^{209}Bi at E_p = 72 MeV*, Nucl. Phys. A389, 247 (1982).

Kno89 - G.L. Knoll, *Radiation Detection and Measurement Second Edition* (John Wiley & Sons, New York, 1989).

Mab07 - J. Mabiala, *Theoretical Description of Quasi-free A(a, a'b)B Reactions*, diploma project, Africa Institute for Mathematical Sciences (AIMS) (June 2007), unpublished.

Mar70 - Pierre Marmier and Eric Sheldon, *Physics of Nuclei and Particles* Vol. II (Academic Press, Inc. New York 1970).

Mey83 - H.O. Meyer, P. Schwandt, W.W. Jacobs, and J.R. Hall, *Proton Scattering from ^{12}C between 120 and 200 MeV and the Optical Potential*, Phys. Rev. C 27, 459 (1983).

Mos80 - G.A. Moss, L.G. Greeniaus, J.M. Cameron, D.A. Hutcheon, R.L. Liljestrand, C.A. Miller, G. Roy, B.K.S. Koene, W.T.H. van Oers, A.W. Stetz, A. Willis, and N. Willis, *Proton-^{4}He Elastic Scattering at Intermediate Energies*, Phys. Rev. C 21, 1932 (1980).

Nad81 - A. Nadasen, P. Schwandt, P.P. Singh, W.W. Jacobs, A.D. Bacher, P.T. Debevec, M.D. Kaitchuck, and J.T. Meek, *Elastic Scattering of 80-180 MeV Protons and the Proton-Nucleus Optical Potential*, Phys. Rev. C 23, 1023 (1981).

Nad81b - A. Nadasen, P. Schwandt, P.P. Singh, W.W. Jacobs, A.D. Bacher, P.T. Debevec, M.D. Kaitchuck, and J.T. Meek, *^{40}Ca (p, pα) ^{36}Ar Reaction in a Noncoplanar Geometry*, Phys. Rev. C 23, 2353 (1981).

Nad89 - A. Nadasen, P.G. Roos, N.S. Chant, C.C. Chang, G. Ciangaru, H.F. Breuer, J. Wesick, and E. Norbeck, *(p, pα) Cluster knock-out Reaction on ^{9}Be at 200 MeV*, Phys. Rev. C 40, 1130 (1989).

Nev07 - R. Neveling, A.A. Cowley, Z. Buthelezi, S.V. Förtsch, H. Fujita, G.C. Hillhouse, J.J. Lawrie, G.F. Steyn, S.M. Wyngaardt, N.T. Botha, L. Mudau, and S.S. Ntshangase, *Analysing Power of the ^{40}Ca(p,pα) Reaction at 100 MeV*, (2007), unpublished.

Pil89 - J.V. Pilcher, A.A. Cowley, D.M. Whittal, and J.J. Lawrie, *Protons of 200 MeV Incident on ^{12}C. I. Coincident Proton Emission from the Continuum*, Phys. Rev. C 40, 1937 (1989).

Ric94 - W.A. Richter, A.A. Cowley, G.C. Hillhouse, J.A. Stander, J.W. Koen, S.W. Steyn, R. Lindsay, R.E. Julies, J.J. Lawrie, J.V. Pilcher, and P.E. Hodgson *Pre-equilibrium (p,p') Measurements and Calculations for ^{90}Zr and Neighbouring Nuclei for Incident Energies up to 200 MeV*, Phys. Rev. C 49, 1001 (1994).

Roo77 - P.G. Roos, N.S. Chant, A.A. Cowley, D.A. Goldberg, H.D. Holmgren, and R. Woody, *Absolute Spectroscopic Factors from the (p, pα) Reaction at 100 MeV on 1p-shell Nuclei*, Phys. Rev. C 15, 69 (1977).

Ste97 - S.W. Steyn, *Multistep Direct Reactions in Nuclei*, PhD thesis, University of Stellenbosch (1997).

Van82 - W.T.H. van Oers, B.T. Murdoch, B.K.S. Koene, D.K. Hasell, R. Abegg, D.J. Margaziotis, M.B. Epstein, G.A. Moss, L.G. Greeniaus, J.M. Greben, J.M. Cameron, J.G. Rogers, and A.W. Stetz, *^{4}He (p, 2p) ^{3}H Reaction at Intermediate Energies*, Phys. Rev. C 25, 390 (1982).

Wan85 - C.W. Wang, P.G. Roos, N.S. Chant, G. Ciangaru, F. Khazaie, D.J. Mack, A. Nadasen, S.J. Mills, R.E. Warner, E. Norbeck, F.D. Becchetti, J.W. Janecke, and P.M. Lister, *^{9}Be (p, pα) ^{5}He Cluster Knock-out Reaction with 150 MeV Polarised Protons*, Phys. Rev. C 31, 1662 (1985).

Yos98 - T. Yoshimura, A. Okihana, R.E. Warner, N.S. Chant, P.G. Roos, C. Samanta, S. Kakigi, N. Koori, M. Fujiwara, N. Matsuoka, K. Tamura, E. Kubo, and K. Ushiro, *Alpha Spectroscopic Factors for ^{6}Li, ^{7}Li, ^{9}Be and ^{12}C from the* $(\vec{p}, p\alpha)$ *Reaction at 296 MeV*, Nucl. Phys. A 641, 3 (1998).